UNIVERSIDADE DE LISBOA
FACULDADE DE CIÊNCIAS
DEPARTAMENTO DE FíSICA

ON THE HOT INTERSTELLAR MEDIUM OF HIGH-REDSHIFT GALAXIES

Lara Sofia Gorgulho Alegre

MESTRADO EM FíSICA
Especialização em Astrofísica e Cosmologia

Dissertação orientada por:
Prof. Doutor David Ricardo Serrano Gonçalves Sobral

2017

Abstract

At high redshift, galaxies are very different from the ones in the local Universe. They present several high ionization ultraviolet emission lines such as CIV, OIII] and CIII], besides HeII which is associated with young and massive stars. The energy required for the production of emission lines like CIV was once only associated to Active Galactic Nuclei (AGNs). However, photoionization models have shown that these lines can be produced by star forming galaxies (SFGs) holding very hot and young stellar populations with a low metal content.

The properties of high-redshift galaxies are not fully understood and the discrimination between these galaxies and AGNs is essential for their understanding. Recently, diagnostic diagrams using ultraviolet emission lines started being developed, however they are based on single stellar populations, which cannot reproduce the spectral energy distribution of these galaxies.

In this work we produce and present three sets of models of nebular emission that allow to interpret and distinguish SFGs and AGNs, using the photoionization simulation code CLOUDY.

We created a set of CLOUDY models using black bodies with a broad range of temperatures (20000 - 150000 K), densities (10^2 - 10^5 cm^{-3}) and metallicities ($1 - 10^{-5}$ $Z_\odot$), which span from ionization parameters logU $\sim$ -1 to -4.5. This provides a set of models with well known input parameters. Models below $\sim$ 70000K can reproduce SFGs while the ones with higher temperature go into the classical AGN regime.

To simulate AGNs we create another set of models based on power laws with slopes from -1.2 to -2.0 within the same range of densities and metallicities.

Thirdly, for SFGs we used the state-of-the-art binary stellar evolutionary models BPASS.V2 (Binary Population And Spectral Synthesis code). It is thought that at least $\sim$ 70% of stars live in binary systems. Binary interactions which account for rotation effects are extremely important to understand the spectral energy distribution of these galaxies. In particular, for low metallicity systems, at which binary interactions promote dynamically mass transfer between the stars contrarily to high metallicity systems where the binary tends to become a wide structure.

We present emission-line ratios diagnosis diagrams based on CIII], OIII], CIV and HeII] using our photoionization models. These diagrams allow to discriminate between SFGs and AGNs and at the same time provide a tool for unveiling the physical properties of these sources.

We apply the modelling results to a population of 10 analogues of high redshift galaxies at z $\sim$ 2 - 3 selected by their UV continuum. We found that these galaxies are better described by our BPASS models holding young stellar populations with ages $\sim$ $10^{6.4}$ - $10^{6.8}$ yrs, ionization parameters $\sim$ logU = -2.21 , low stellar metallicities $\sim$ 0.2 - 0.1 $Z_\odot$ and very low gas metallicities $\sim$ 0.004 $Z_\odot$. We used the results obtained for these galaxies to calculate optical emission lines fluxes for [OIII],

[OII], Hα and Hβ. These emission line fluxes can probe metal poor SFGs at high redshift to be observed with upcoming telescopes such as the James Webb Space telescope, and further test the validity of BPASS models to explain these sources.

We then analyse 6 bright Lyα emitters at the same range of redshifts, and we found that 3 of these systems are also better described by our BPASS models. They are consistent with being analogues of high redshift galaxies, in particular 2 galaxies which present young ages ($\sim 10^{6.3}$ - $10^{6.5}$ yrs), higher ionization parameter (logU = -1.84 to -1.74) and lower stellar metallicity (< 0.1 $Z_{\odot}$) than the previous UV continuum selected galaxies.

We then use our models to understand the absence of metal lines in bright LAEs at redshifts up to z = 6 - 7, and we conclude that most of these sources require deeper observations.

Lastly, we analyse galaxies from the HiZELS survey, selected with narrow band filters by their bright Hα emission line. We analyse a total of 425 spectra obtained with follow-up VIMOS (VLT) spectroscopy and we calculated the spectroscopic redshifts of 87 galaxies and AGNs. We found bright ionization ultraviolet lines in 2 of these galaxies at z $\sim$ 1.5 and we estimate that these galaxies present extreme properties similar to the z $\sim$ 2 - 3 bright LAEs analysed before.

Our models provide a tool to discriminate between the nature of the galaxies, and estimate their physical properties. Our results are highly important to understand the properties of young galaxies now being found at the epoch of reionization.

We aim to make all our modelling results fully public so it can benefit a wider community.

Keywords: galaxies: evolution; high-redshift; Interstellar medium; emission lines; observations.

Part of this work has been submitted or is in preparation for submission to the Monthly Notices of the Royal Astronomical Society:

- "Spectroscopic properties of luminous Lyman-α emitters at $z \approx 6-7$ and comparison to the Lyman-break population." Matthee, Jorryt, David Sobral, Behnam Darvish, Sérgio Santos, Bahram Mobasher, Ana Paulino-Afonso, Huub Röttgering, and Lara Alegre. arXiv preprint arXiv:1706.06591 (2017).
- Sobral et al. in prep (including Lara Alegre), "The nature and diversity of luminous Lyα emitters at z = 2 - 3: an extremely ionising population"
- Alegre et al. in prep, with the bulk of the results presented in this thesis.

Resumo

Galáxias distantes, a elevado "redshift", apresentam características muito diferentes das galáxias do Universo local. São galáxias pequenas e compactas, por vezes com formas bastante irregulares e muitas vezes em processos de fusão com outras galáxias. Estas galáxias contêm maioritariamente populações estelares jovens, dominadas por estrelas massivas que produzem elevada quantidade de fotões ionizantes. Espera-se que alberguem também as primeiras gerações de estrelas (população III). O seu elevado número a alto redshift bem como a energia que produzem leva-as a serem consideradas as responsáveis pela reionização do Universo.

No espetro destas galáxias é possível observar riscas de emissão ultravioleta, características de estrelas massivas, como HeIIλ1640 Å, CIII]$\lambda\lambda$1907,1909 Å, CIV$\lambda\lambda$1948,1951 Å e OIII]$\lambda\lambda$1661,1666 Å. Estas riscas requerem elevadas energias de ionização, sendo mais comuns em galáxias a elevado redshift. No entanto, a redshift aproximadamente entre 2 e 3, várias observações indicam existir uma população de galáxias com características semelhantes. São galáxias compactas, com altas taxas de formação estelar, baixa metalicidade e riscas de emissão semelhantes. Nesta gama de redshifts as linhas de alta ionização ultravioleta destas galáxias estão deslocadas para comprimentos de onda no ótico, o que permite observá-las com telescópios localizados no solo.

Estudar estas galáxias ajuda-nos a compreender galáxias a elevado redshift e permite-nos desenvolver meios de diagnóstico para identificar as suas características e compreender a sua natureza. Estes meios de diagnósticos serão úteis para estudar galáxias a elevado redshift cujas linhas ultravioleta estão deslocadas para comprimentos de onda maiores, sendo melhor observadas a partir do espaço. Novos telescópios, como por exemplo o James Webb Space Telescope, terão a capacidade de observar espetros de milhares de galáxias até redshifts perto de 10. No entanto existe já a necessidade de compreender galáxias encontradas no final da época da reionização (redshifts aproximadamente entre 6 e 7) como é o caso da galáxia CR7, que apresenta apenas Lyα e HeII indicando uma população de estrelas com elevada grande capacidade de ionização e baixa metalicidade, por exemplo uma população III de estrelas. No entanto os meios de diagnóstico que existem não conseguem explicar as riscas de emissão observadas nestas galáxias.

Muitas vezes estas galáxias produzem energias de ionização associadas a AGNs ("Active Galactive Nuclei", buracos negros ativos que ejetam material até Mega parsecs de distância). Distinguir galáxias com tais características de AGNs não é fácil. Para galáxias a baixo redshift e com propriedades semelhantes às galáxias do Universo local, este tipo de diagnóstico já existe, usando por exemplo, razões entre linhas de emissão do espetro visível, como é o caso do diagrama BPT. Diagramas de diagnóstico recorrendo a linhas ultravioleta tendo em conta os fluxos de emissão detetados nestas galáxias só agora começaram a ser desenvolvidos.

Neste projeto utilizamos ao código de fotoionização CLOUDY para simular as condições físicas características deste tipo de galáxias, bem como em AGNs. O CLOUDY determina as condições físicas de um gás irradiado por uma fonte de ionização externa, resolvendo numericamente as equações de equilíbrio estatítisco, conservação de carga e de energia. O CLOUDY permite definir diversas condições, quer para a fonte de ionização, quer para as propriedades do gás que rodeia estas fontes. Como output, o CLOUDY determina por exemplo o nível de ionização, as condições químicas do gás, a temperatura e gera centenas a milhares de linhas de emissão.

Para criar os nossos models usamos diferentes geometrias (esférica para simular galáxias e plano paralela para simular AGNs) e várias condições de densidade e baixa metalicidade, tendo em conta que as abundâncias dos elementos carbono e azoto não variam linearmente com a metalicidade do gás.

Foram criados três tipos de modelos com fontes de ionização diferentes: um corpo negro com temperaturas entre 20000K a 150000K, que permite simular o comportamento tanto de uma galáxia com formação estelar como de um AGN (a temperaturas e condições de ionização mais elevadas); uma lei de potência com diferentes expoentes, que permite modelar AGNs; e distribuições espectrais de energia baseadas em formação estelar (modelos BPASS), que permitem simular de uma forma mais realista galáxias com formação estelar.

Enquanto a energia produzida por uma lei de potência ou por um corpo negro permite simular condições sem incertezas inerentes a modelos de AGNs ou modelos estelares, para interpretar o seu espetro de emissão de uma galáxia de forma precisa é necessário recorrer a modelos de evolução sintética (ES), também referidos muitas vezes como populações sintéticas estelares (SPS).

Existe um grande número de modelos de evolução sintética, que podem variar, de uma forma geral, de modelos teóricos que incluem processos de evolução estelar a modelos empíricos. Contudo, modelos de evolução sintética convencionais não conseguem explicar os fluxos característicos destas galáxias. Por essa razão, evolução estelar e evolução galática criaram de certa forma uma sinergia. Novos modelos de evolução sintética que incluem interações estelares binárias bem como rotação estelar, revelaram um grande impacto na distribuição espectral de energia das galáxias, principalmente a baixa metalicidade. Estes efeitos prolongam a vida das estrelas massivas, essenciais para a produção de fotões ionizantes. Estes novos modelos de evolução sintética são também essenciais para compreender a reionização do universo, uma vez que eles conseguem prever os fotões necessários para a reionização. Da mesma forma, estudar galáxias com tais características tem permitido grandes avanços na compreensão dos processos relativos a estrelas massivas.

No nosso projeto usámos a última versão dos modelos de evolução sintética BPASS V2.0 (Binary Population And Spectral Synthesis code) que inclui modelos estelares que têm em conta os efeitos descritos. Desta forma, é possível descrever e interpretar de forma mais precisa as condições reais destas galáxias. Com esse objetivo, usamos os nossos modelos para reproduzir diferentes diagramas de diagnóstico baseados em razões entre várias linhas de alta ionização, como CIV/HEII, CIII]/HEII, CIII]/CIV e OIII]/HEII. Os nossos modelos permitem fazer um diagnóstico das fontes, tanto a nível da sua natureza (AGNs vs SGFs) como estimar as suas propriedades. Os nosso modelos de fotoionização que utilizam os modelos de evolução sintética BPASS conseguem reproduzir condições em galáxias com baixa metalicidade que outros modelos de evolução sintética que não incluem sistemas binários não conseguem explicar.

Utilizando os nossos modelos, estudamos várias galáxias, ao longo de diferentes redshifts. Os nossos modelos permitem descrever de forma mais realista as condições de várias galáxias encontradas a redshifts 2 - 3, semelhantes a galáxias a elevado redshift.

Com base nas nossas interpretações fizémos uma previsão dos fluxos de linhas óticas caraterísticos deste tipo de fontes, a serem detetadas com o James Webb Space Telescope em galáxias a elevado redshift.

Com ferramentas que permitem analisar de forma mais precisa galáxias com baixa metalicidade, selecionámos e estudámos duas galáxias a redshift ~ 1.5 do HiZELS survey, selecionadas através da sua linha de emissão Hα, que indica alta taxa de formação estelar. Estas galáxias foram observadas com o instrumento VIMOS (Very Large Telescope) e apresentam condições semelhantes a galáxias encontradas a redshifts 2 - 3 e análogas a galáxias a elevado redshift.

Os resultados obtidos são importantes para compreender e interpretar as propriedades das galáxias a elevado redshift e ajudam a explicar a energia necessária para a reionização do Universo através destes pequenos e compactos sistemas.

Palavras-chave: galáxias: evolução; elevado redshift; meio interestelar; linhas de emissão; observações.

Contents

List of Figures

List of Tables

Chapter 1

Introduction

1.1 Lookback time

The study of galaxy formation and evolution is only possible because we live in a Universe that is in harmony with the Cosmological principle. This principle states that the Universe is homogeneous and isotropic at large scales. This has been corroborated by several observations (e.g. CMB, Cosmic Microwave Background, Penzias and Wilson (1965)), and it is also in agreement with the concordance model (ΛCDM, Cold Dark Matter Model, Ostriker and Steinhardt (1995)).

According to the ΛCDM, the Universe has a positive Λ constant, meaning that all the galaxies are receding from us (Hubble (1929)) at an accelerated rate (Riess et al. (1998)). No matter where we look up on the sky, as the light speed is finite, we are literally looking back in time. Galaxies that are at the same distance in space from us, will be at the same distance in time. This also means that there must have been a starting point in space and time (Big Bang). We can then study galaxies at different epochs of the Universe inferring its evolution across cosmic time.

In an expanding Universe the recession speed v is given by the Hubble's law $v = \mathrm{H}_0\, d$, where d is the distance to the observer and H_0 is the Hubble constant ($\mathrm{H}_0 = 67.8 \pm 0.9$ km s^{-1} Mpc^{-1}, Planck Collaboration et al. (2016)). Astronomical distances of extragalactic objects are usually described in terms of redshift (z), which is a function of the recession speed of the objects:

$$1 + z = \sqrt{\frac{1 + v/c}{1 - v/c}} \tag{1.1}$$

The redshift results from the expansion of space itself and is related with the cosmic scale factor $a(t)$ by:

$$1 + z = \frac{a(t_e)}{a(t_o)} \tag{1.2}$$

The cosmic scale factor is the relative expansion of the Universe as function of time, where $a(t_o)$ represents the size of the Universe when the light from the object is observed, and $a(t_e)$ the size of the Universe when the light was emitted. The light wave originally emitted is lengthened by the space expansion and is shifted to longer (redder) wavelengths. Therefore it can be used to calculate the redshift:

$$z = \frac{\lambda_o - \lambda_e}{\lambda_e}, \tag{1.3}$$

where λ_0 is the observed wavelength and λ_e is the emitted one.

The redshift can be used to calculate the age of an object. The evolution of the Hubble constant, which can be calculated through the Friedmann equations applied to the general relativity, evolves over time with the relation:

$$H(a) \equiv H_0 \sqrt{\Omega_r \ a^{-4} + \Omega_m \ a^{-3} + \Omega_k \ a^{-2} + \Omega_\Lambda} \ , \text{ where } a = a(t) = \frac{1}{1+z} \tag{1.4}$$

By definition $H \equiv \dot{a}(t)/a(t)$, therefore $da = a \ H(a) \ dt$. Integrating we can obtain the lookback time age:

$$t = \int_0^a \frac{da}{a \ H(a)} \tag{1.5}$$

The age of the Universe ($a = a_0 = 1$, $z = 0$) can be calculated using the last results of the cosmological parameters (Planck Collaboration et al. (2016)): $\Omega_\Lambda = 0.692 \pm 0.012$ (dark energy density), $\Omega_m = 0.308 \pm 0.012$ (matter density: baryons and dark matter), $\Omega_r \sim 10^{-4}$ (radiation density: photons and neutrinos) and $\Omega_k < 0.005$ (spatial curvature). These are estimations for the present day cosmological parameters and leave us with a Universe with 13.799 ± 0.021 Gyr.

1.2 Epoch of reionization

Because our Universe has a finite age, the size of the observable universe is also finite. The light can only reach us from distances smaller than the age of the Universe. However, during the first $\sim 400\,000$ million years after the Big Bang, radiation dominated and the Universe was opaque due to the Thompson scattering of the free electrons on the dense and hot plasma.

As the Universe expanded and cooled, matter started to dominate over radiation and almost all free electrons and protons combined to form neutral hydrogen atoms. This process is known as "recombination" (even though electrons and nuclei had never been "combined" before) and occurred at $z = 1100$. After the recombination, the universe became transparent to the CMB (i.e. the photons that were last scattered at that time).

According to the CMB measurements, the Universe was essentially homogeneous. However, tiny fluctuations in density and temperature became bigger with time as the gravitational forces were also slightly stronger than in other regions. Overdense regions of space started to collapse under gravity and stopped to expand. Dark matter may have played here a major role since baryonic matter could not collapse efficiently by itself.

The first stars and galaxies did not start to form before $z \sim 50 - 20$, during the "Dark Ages", inside mini dark matter haloes. These very first galaxies produced high-energy photons, ionizing the diffuse hydrogen in their immediate surroundings, and beginning a progressive process that culminated with the full "reionization" of the Universe.

Planck Collaboration et al. (2016) estimated an instantaneous reionization at $z \sim 8.8^{+1.2}_{-1.1}$. Several observational constrains place it $6 \lesssim z \lesssim 10$ (e.g. Robertson et al. (2015)), while other

observations indicate that the process was essentially completed by z $\sim$ 6, because the number density of neutral hydrogen clouds increases above that redshift (e.g. Fan et al. (2006), Stark et al. (2015)).

Furthermore observations have also shown that it was not an homogeneous process but rather occurred in preferred regions, being a patchy process (e.g. Matthee et al. (2015), Sobral et al. (2015)). This also supports the idea that reionization started around strong ionizing sources that created bubbles of ionized hydrogen in their vicinity. Ionized regions gradually overlapped each other and the typical distances travelled by the ionizing photons grew rapidly, which led to a largely ionized intergalactic medium (IGM) with smaller regions of moderate overdense gas.

One of the main questions in astrophysics and cosmology is the understanding of the cosmic epoch of reionization and the physical processes responsible for it. The transition of the Universe from neutral to ionized is associated with the presence of photons with energies higher than 13.6 eV ($\lambda < 912$ Å, ultraviolet light (UV)) produced by the first stars and galaxies. However, the physics behind the escape fraction of hydrogen ionizing photons (f_{esc}) is not completely understood (e.g. Hayes (2015)) and the process is complex from both theoretical (e.g. Robertson et al. (2015)) and observational (e.g. Sobral et al. (2017)) perspectives.
Furthermore, the state of ionization is determined by the balance between the rate of hydrogen recombination and photoionization, where the number of ionizing photons is crucial to maintain the ionization state of the Universe. Studies of local metal poor galaxies can help understanding the problems inherent to the escape fraction (e.g. Izotov et al. (2016)).

Cosmic reionization drivers

Star-forming galaxies (SFG) and Active Galactic Nuclei (AGN) have always been pointed as the main drivers for cosmic reionization, since they are strong ionizing sources. Their relative contributions to the total UV emission across cosmic time is still uncertain; however, SFGs have been favoured as the main contributors at early times (e.g. Robertson et al. (2015), Bouwens et al. (2015)) and the ones responsible for conserving the ionization state of the Universe (e.g. Fan et al. (2006), Haardt and Madau (1996)). AGNs by themselves are not enough to reionize the Universe and maintain the hydrogen reionization higher mainly because at z $\gtrsim$ 3 the number density of bright AGNs drops (e.g. Masters et al. (2012)). While bright AGNs are known to exist at z $>$ 7 (e.g. Mortlock et al. (2011)), their UV luminosity function declines rapidly between z $\sim$ 4 and $z \sim 6$ (e.g. Parsa et al. (2017)). At z $\sim$ 6 the AGN contribution for the total UV luminosity budget is an order of magnitude smaller than the level required to maintain the ionization state against hydrogen recombination (Parsa et al. (2017)). However, the faint-end slope of the AGN luminosity function remains uncertain and their role in the reionization process is not completely understood (e.g. Kim et al. (2015)).

It has been possible to measure the galaxy UV luminosity function out to z $\sim$ 10 (e.g. Bouwens et al. (2015)), which points towards a rapidly growing population of early star forming galaxies that could have produced the UV photons necessary for the reionization and its maintenance. Galaxies detected at high-redshift present hard ionizing spectra (e.g. Stark et al. (2015)), suggesting that they may be more common during the reionization and hence very different from the galaxies at

lower redshifts. Some exceptions are extremely metal poor galaxies recently found at redshifts 2 - 3 (e.g. Amorín et al. (2017), Vanzella et al. (2016)). Moreover, Ma et al. (2016) studied the effect of stellar binary evolution (using BPASS evolutionary synthesis; see Section 1.6.2) on the production of ionizing photons and on the escape fraction and concluded that the later time photons easily escape, increasing the escape fraction, in particular for low-metallicity galaxies. For single stellar models $f_{esc} \sim 5\%$, less than the 20 % required by models of cosmic reionization (e.g. Robertson et al. (2015)). The effective escape fraction to the IGM (i.e. the ratio between the ionizing flux and the continuum flux at 1500 Å) is boosted by factors of $\sim 4 - 10$ using BPASS models (Ma et al. (2016) indicating that f_{esc} from SFGs are in agreement with the values required to ionize the Universe. It is then necessary to understand the properties of the first galaxies, characterize their contribution with energetic UV photons at early times and estimate also the fraction of ionizing hydrogen photons that escaped to the IGM.

1.3 First Galaxies

The light emerging from a galaxy is a combination of stellar and gas emission, processed by intervening dust. However the presence of a supermassive black hole (SMBH) in the central regions of the galaxies can produce one of the most powerful energy sources in the Universe, which cannot be attributed to the normal components of galaxies: an AGN.

The first galaxies should have been very different from the galaxies at lower redshift. Images from the Hubble Deep Field (Beckwith et al. (2006)) show small and irregular galaxies that probably underwent through periods of multiple mergers to form larger galaxies like the Milky Way.

Considering the lack of sufficient confirmed high redshift galaxies beyond z $\sim$ 6 and the qualitative change in the galaxy population relative to lower redshifts, it is very difficult to constrain and distinguish the properties of high redshift AGNs and SFGs.

1.3.1 Star Forming Galaxies

The first galaxies should be a combination of different populations of stars, with different ages, which are dominated by the hot and massive stars, that spend most of their lives with effective temperatures above 10^4 K, hence emitting in the UV.

In a young universe, where heavy elements had yet to be formed, the first generation of stars (Population III, POP III) formed by the collapse of gas clouds made of hydrogen and helium (and their isotopes) with traces of lithium (e.g. Glover (2011)).

The cooling processes are extremely dependent on the metal content of the gas, occurring mainly through the de-excitation of collisional excited metal transitions because hydrogen and helium require high energies for collisional excitation from the ground state ($>$ 10.2 eV). This implies high temperatures for cooling processes to occur and high Jean mass of gas (minimum mass to collapse under gravity, which is proportional to the square of the temperature) to contract and subsequent collapse into stars. For that reason it is expected that the first stars were very massive, with hundreds of solar masses (e.g. Abel et al. (2000)), with very low metallicity ($\leq 10^{-4} Z_{\odot}$, Schneider

et al. (2002)) and short-lived that evolved rapidly into Type-II supernovae enriching the interstellar medium (ISM). The enriched ISM can cool more efficiently forming POP II stars, less massive and metal-poor stars. Ultimately it forms POP I stars, smaller, metal-rich and longer lived.

Recent studies have shown that 70 % of massive stars are expected to live in binary systems where stars interact with each other (e.g. de Mink et al. (2013)). It is therefore important to take into account binary evolution and rotation, in particular, because they are more accentuated at low metallicities (Eldridge et al. (2008), Stanway et al. (2014)). Binary effects can extend the lifetime of massive stars, producing UV photons during more time, which justifies the hard radiation fields found at high-redshift galaxies and which can help to unveil its true contribution for the reionization (Stanway et al. (2016)) .

One of the most fundamental observables of galaxy evolution is its star formation rate. To understand star formation in the first galaxies it is necessary to understand how efficiently these galaxies form stars, which depends on the cooling processes and on the density and metallicity of the gas; the stellar Initial Mass Function (IMF), which describes the fractional distribution in mass of a newly formed stars (Salpeter (1955)); and the stellar feedback.

Comparing the ionizing flux from high redshift galaxies with binary evolutionary synthesis models show variations in the Initial Mass Function (Stanway (2017)). POP III IMF is expected to be top-heavy compared to that of Milky Way stars (Johnson (2013)) due to several physical processes (Bromm and Yoshida (2011)) and it is critical for the amount of metals that they release into the ISM (Heger and Woosley (2002)).

1.3.2 Active Galactic Nuclei

AGNs are compact objects with highly variable luminosities over short timescales and with an emission highly polarised. With a superheated accretion disk and relativistic jets that can extend to hundreds of kiloparsecs, these galaxies can reach extremely high brightness radiating across all the spectrum. Many efforts have been made to understand and characterize the formation and growth of the SMBHs. While most studies focus on the peak of both galaxy and SMBH growth at z = 1 – 4, how the first SMBHs formed and grew is not exactly known. They can have been formed through the first generations of POP III stars (e.g. Volonteri and Rees (2006), Alvarez et al. (2009)), which with a mass of 10 - 100 $M_\odot$ can end their life as a black hole (which requires that POP III must grow rapidly shortly after they have formed); or directly collapsing from the primordial gas clouds producing masses of $10^4 - 10^6$ $M_\odot$ (e.g. Bromm and Loeb (2003)), where then they can grow to higher masses through periods of merging and/or high accretion rates (Di Matteo et al. (2012)) to achieve masses of 10^9 $M_\odot$ of the currently known z > 6 SMBHs (e.g. Mortlock et al. (2011)).

1.3.3 The Interstellar Medium

The Interstellar Medium (ISM) is the material for the star formation. Its chemical evolution is intrinsically related with its stellar content. However, the ISM can also reveal the stellar effects on its environment, for example, the energy released by massive stars can be measured through the energy content of the surrounding ISM. There is a vast information that can be revealed by the ISM, such as the chemical composition, temperature, velocities, ionization mechanisms, etc.

The ISM is composed essentially by gas ($\sim$ 75 % of hydrogen (H) and $\sim$ 25 % of helium (He), with traces of heavier elements) and a small percentage of microscopic particles of dust ($\lesssim$ 1 %). It contains cold gas of molecular hydrogen and other molecules (H I regions) and warm ionized gas close to hot, massive and young stars and/or intense star formation (H II regions).

The hot ISM

It is accepted that the ISM is a multiphase medium (even with some controversy, e.g. Vazquez-Semadeni (2009)), where the gas exists in a number of thermal phases (in pressure equilibrium against isobaric perturbations) which depends on the sources of heating, ionization, etc. According to Field et al. (1969) there is a warm and a cold phase. Later McKee and Ostriker (1977) added a third phase: a hot and low-density ISM, considering the role of supernovae explosions.

This very hot plasma is expected in strong extragalactic UV and X-ray sources like AGNs and SFGs, due to supernovae explosions and/or stellar winds (e.g. around Wolf-Rayet stars) and have temperatures $> 10^6$ K. To fulfill the pressure equilibrium with the other surrounding phases of the ISM, density values must be very low (0.01 - 0.001 cm^{-3}). In compact H II regions the density is around $10^3 - 10^4$ cm^{-3} whereas in extragalatic regions values can be lower ($\sim 10^2$ cm^{-3}, Hunt and Hirashita (2009)).

Strömgren sphere

A star can be approximately described by a black body radiation field which include a significant number of photons with energies $>$ 13.6 eV (UV), capable of ionize the hydrogen atom. Higher energies (from hotter stars) are required to ionize helium at 24.5 eV. These stars produce ionizing UV photons that transfer energy to the gas through photoionization creating a Strömgren sphere (ionized region around the central source) which depends on the rate of the ionizing photons, the hydrogen density and the size of the H II regions (Strömgren (1939)). The Strömgren radius grows with time until reaching an equilibrium between ionization and recombination. If the H I region is small, or the ionizing source is strong or the density is small, all the sphere can be completely ionized (matter bounded). Contrarely, it can create a partially ionized thin boundary (ionization bounded).

Strömgren assumptions rely on an isotropic medium with a constant density. In reality there is a variety of ionizing sources (such as regions of massive star formation, planetary nebulae, supernovae, AGNs) and the ionized gas can have different morphologies: from spherical or elliptical, to bipolar shapes, tori, or even completely irregular. The gas can also be filamentary or clumpy. The ionization structure in AGN clouds is different from H II regions, where thick clouds at the illuminated part of the AGN produce high ionization species, being almost completely neutral on the back. Different mechanisms coming from different regions of the AGN contribute for the emission in different regions of the spectrum. In the range of energies between the optical-UV to the X-rays, it is thought that the hard photons from the accretion disc create a photoionized plasma, responsible for AGN broad emission lines (Haardt and Maraschi (1993)) while narrow lines arise from colder gas further away from the centre (e.g. Haardt and Madau (1996)). At high redshift, galaxies are also very different, with different stellar populations, more gas-richer, with higher star formation rates, a low-density

ISM and more clumpy (Tacconi et al. (2013)). Furthermore at high redshift, the gas composition is expected to be very different from the standard solar composition and other contributions such as winds and shocks make photoionized regions difficult to understand. Photoionization codes (Section 1.6.1) can help handle several of these challenges using state-of-the-art treatments for several microphysical processes that allow to compute the energy balance producing a self-consistent model of the ionized region.

1.3.4 The Spectra

The physical processes dominating ionized regions are photoionization (removal of a bound electron from an atom by a photon, forming an ion and an electron) and recombination (free electron recombines with an ion). However, other processes contribute for the emission lines and the continuum spectra. All of these processes are proportional to a function of temperature (different for each process) and to the electron and the relevant ionic species number densities.

Continuum

The continuum spectra arises from Bremsstrahlung radiation (free-free emission, i.e. a free electron is accelerated by an ion, emitting a photon) which occurs mainly at radio frequencies; bound-free (or recombination emission) which occurs during radiative recombination and where free electrons are recaptured by ions in a certain energy level, producing discontinuities in the spectrum, such as the "Balmer discontinuity" (recombinations to n = 2); and two-photon emission, resulting from excited metastable states (particularly important for H and He, and at low densities), being the most important contribution for the UV continuum.

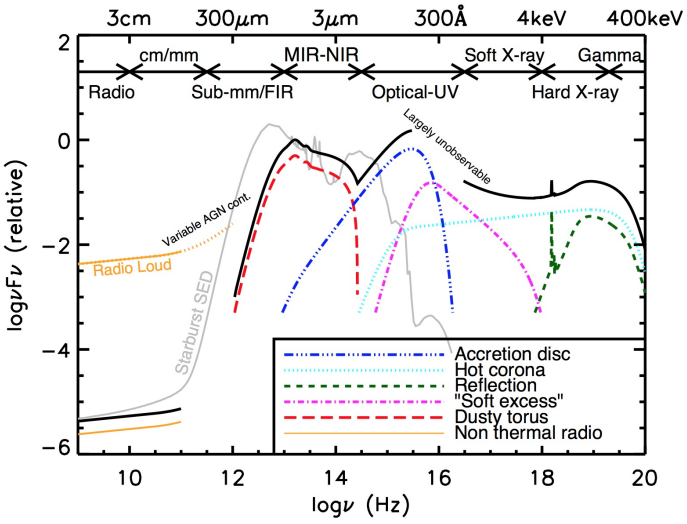

Figure 1.1: Schematic diagram of a typical AGN spectral energy distribution (SED) with the indication of the individual processes that contribute for the continuum emission, from Harrison (2016). Note that the radio-loud AGNs present radio emission several orders of magnitude higher than radio-quiet AGNs. The black solid line represents the total SED. The grey line represents a typical SFG. Low-metallicity galaxies can see their UV continuum extended to higher energies, as discussed in the next sections.

Binary systems of massive stars can emit also X-rays due to mass transfer to the companion

star. Dust contributes also for the thermal continuum emission, where the energy absorbed by the dust is emitted in the mid to far infrared (IR) part of the spectrum. AGN's plasmas can also be dominated by non-thermal radiation such as synchrotron mechanisms (radio-loud AGNs) at radio wavelengths and inverse Compton scattering on the X-rays, where low energy photons produced by the accretion disc are scatter to higher energies by relativistic electrons (Haardt and Maraschi (1993)). At gamma rays, Compton scattering arises from AGN's relativistic jets (see Figure 1.1).

Emission lines

Ionized regions are characterized by an emission spectrum with an important emission line component. Emission lines include strong recombination lines of H and He and collisional excited lines from other elements. As an example is shown a quasar spectra with several prominent emission lines (Figure 1.2).

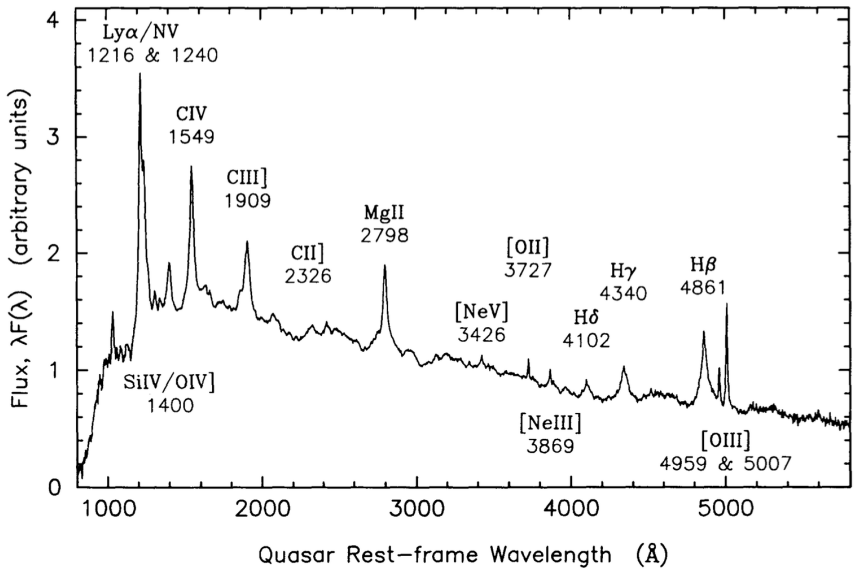

Figure 1.2: Composite spectrum of a "typical" AGN with the identification of the different UV and optical emission line features from Francis et al. (1991). The AGN spectrum is particularly characterized by intense emission lines, presenting usually Lα, the Balmer series, C IVλ1549 Å, [O III]λ5007 Å, where most of the objects present also wide wings corresponding to thousands of km/s. Narrow lines are commonly forbidden lines.

Recombination lines are produced when an electron released by the photoionization process is recaptured by an ion and then decay to lower energy levels through radiative transitions. On the de-excitation cascade, a photon is emitted with a specific wavelength contributing for the intensity of that emission line. Recombination lines of H and He can be found on ionizing regions. With energies above 13.6 eV, H is fully ionized and the H recombination lines that can be seen in the spectra are Lyα (the strongest recombination line, n = 2 to n = 1, λ = 1216 Å) followed by Hα (n = 3 to n = 2, λ = 6563 Å), Hβ (n = 4 to n = 2, λ = 4861 Å) and so on. He can be single or double ionized (He II recombination line requires ionization energies of 54.4 eV, λ = 5876 Å) and other elements such as carbon, oxygen and nitrogen, which can be multiply ionized (producing the correspondent emission lines) depending on the ionization source. The recombination line intensity

increases with decreasing electron temperature.

Collisional excited lines (CELs) form when a free electron excites, through collision, a bound electron to an upper energy level. It then decays, emitting a photon. In the process, the electron can end in a metastable level. Downward transitions from these sub-levels of energy have very low probability of occurring spontaneously. However in low density environments, the collisional de-excitation has time to happen since collisions between the ion or atom and another electron are unlikely. When it decays, it can produce a permitted, a forbidden (e.g. [OII], [OIII]) or semi-forbidden line (e.g. OIII], CIII], SiIII]) depending on the spontaneous transition probability.

1.4 Emission line diagnosis

Both recombination lines and CELs may provide informations about the state of the gas and the ionizing source.

CELs are strongly dependent to the state of the gas. They can reveal the characteristics of the gas, such as electronic temperature and density, in a direct way, and through them it is possible to estimate the ionic abundance relative to hydrogen.

Temperature can be estimated with CELs using lines with different excitation energies. At low density, the collisional excitation depend on the atomic probabilities and on the electron temperature. As temperature increases, the average electron velocity increases, increasing also the population on the $^1S_0$ level. The most common line-ratio used is the optical [OIII]$\lambda\lambda$4959,5007, which arises from the low $^1D_2$ level, and [OIII]λ4363, from the higher $^1S_0$ level (Figure 1.3).

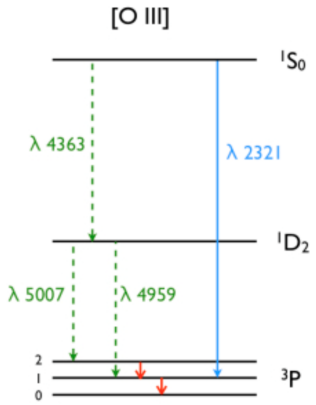

Figure 1.3: Energy-Level diagram for [OIII]

The ratio of a doublet, which includes also ratios such as [OII]λ3729 / [OII]λ3727 or CIII]λ1909 / CIII]λ1907, can give information about the electronic density of the gas. These lines arise from the same level of energy where the energy spacing the doublet is very small compared to the temperature. The critical density of each level is very different since they have different collisional de-excitation rates, which allows to estimate the density.

One of the main properties of SFGs is the star formation rate (SFR). SFR can be estimated using recombination lines, such as Hα where the luminosity of this line is proportional to the

number of photons emitted per second by the source (Q(H)), assuming that all the ionized photons are absorbed by the gas and are produced by OB stars and that the SFR has been constant over the last 10^7 years. Using an evolutionary synthesis code (see Section 1.6.2), it is possible to determine the conversion factors between the ionizing flux and the SFR, which depends on the initial mass function (IMF), stellar library and evolutionary tracks. It is also possible to determine the SFR by calibrating other lines such as [OII] doublet, however this line depends on the metallicity and ionization parameter.

In general, several UV resonance lines (transitions from the first level of energy to the ground state) allow to detect many ionization stages of a given element and so the ionization of the source. An example is carbon which can be detected as CI, CII, CIII or CIV.

In particular scenarios, for example in a radiation-bounded H II region where the density is so low that the ionization source can ionize the entire nebula, line-ratios such [OIII]/[OII] can be used to interpret the ionization of the source. The [OIII] ionization zone is not largely affected but [OII] zone is smaller and the [OIII]/[OII] ratio becomes larger for high ionization parameters (e.g. Kewley et al. (2013), Nakajima et al. (2016), Vanzella et al. (2016)).Besides that the [OIII]/[OII] flux ratio can be used for diagnosing the escape fraction of ionizing photons where a high [OIII]/[OII] may indicate a lose of a considerable fraction of the Lyman continuum emission to the IGM (Izotov et al. (2016)).

The presence of a particular line in the spectrum can also be an indicator of the hardness of the spectra, providing a clue about the nature of the source (Figure 1.4).

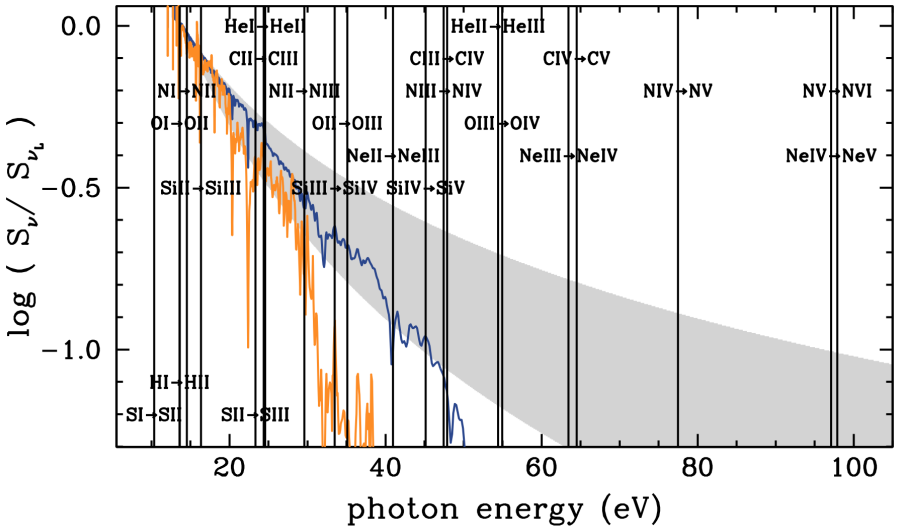

Figure 1.4: Incident SEDs of AGNs and SFGs models from Feltre et al. (2016). The grey shaded area indicates the location of AGN ionizing spectra, whereas the lines indicate low metallicity stellar populations with Z = 0.001 (blue) and Z = 0.03 (orange). The vertical lines show the ionizing energies necessary to produce the emission lines. For example, emission lines requiring ionization energies > 50 eV indicate an AGN, according to these models.

1.4.1 Line-ratios as a diagnosis tool

Due to the sensitive of individual emission lines to several properties of the ISM and to the ionizing source, several emission-line ratio diagnostics have been developed.

BPT diagram

The Baldwin - Phillips - Terlevich diagram (BPT, Baldwin et al. (1981)) is a widely known line-ratio diagram that uses two pairs of line-ratios to distinguish SFGs from AGNs (Figure 1.5). These occupy distinct regions in the BPT diagram due to differences in the SED of their ionizing radiation: in relation to the recombination lines, the optical CELs of AGNs are brighter than those of SFGs. The lines used are close in wavelength to reduce continuum subtraction reduction uncertainties and the effects of dust. BPT probes the shape of the continuum with [N II]/Hα just above 1 Rydberg and the hardness of the spectra with [OIII]/Hβ between 1-3 Rydbergs.

However, the BPT diagram is not fully understood at high-redshift. Several studies with high-redshift galaxies show an offset of these objects on the diagram, which raises questions on its applicability to higher-redshift objects (e.g. Shapley et al. (2005), Holden et al. (2016)).

For example, the BPT diagram can be used as a metallicity indicator. Several studies with SFG at z$\sim$ 2 - 3, selected in the optical rest-frame (e.g. Steidel et al. (2014), Shapley et al. (2015), Masters et al. (2014)) showed higher [NII]/Hα (for a fixed [OIII]/Hβ) than low-redshift galaxies, with near solar metallicities. This has been interpreted as a combination of harder ionizing spectra and higher N/O abundance ratio at high redshift. These may rely mainly in Wolf-Rayet starbursting (e.g. Masters et al. (2014)) where winds from nitrogen-rich Wolf-Rayet stars enrich the ISM and the future generations of stars, and the effects of binaries and rapid rotation on massive main sequence stars (e.g. Steidel et al. (2014)). Note that binary effects are enhanced at sub-solar metallicities. Therefore, the BPT diagram raises some concerns about estimating metallicities at high-redshift from strong line methods that include nitrogen lines.

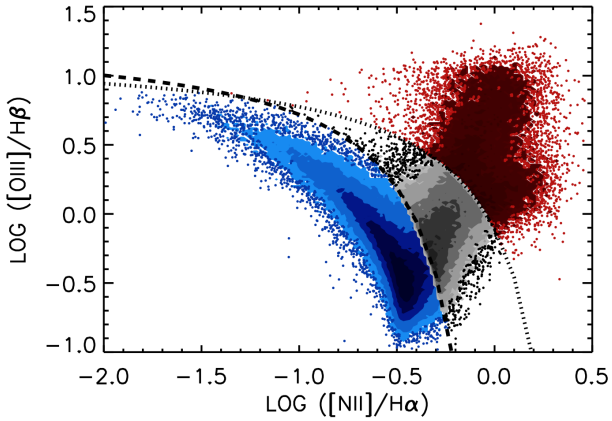

Figure 1.5: Example of a BPT diagram from Trouille et al. (2011) using SDSS data, where the SFGs are shown in blue, composite in grey and AGNs in red. The dashed curve shows Kauffmann et al. (2003) empirical division while the dotted curve shows Kewley et al. (2001) theoretical division.

UV line-ratios

The motivation for the anticipation of future missions such as the JWST, which will collect UV spectra of thousands of galaxies, has led to a recent search for UV line-ratios that allow to distinguish SFGs from AGNs (e.g. Gutkin et al. (2016), Feltre et al. (2016), Jaskot and Ravindranath (2016)).

Gutkin et al. (2016) and Feltre et al. (2016) studied various line-ratios using both UV and optical emission lines. For example, on the UV they found that AGNs and SFGs can be successfully discriminated in line-ratio diagrams that combine HeIIλ1640 with a CEL such as CIVλ1550, OIII]λ1663, CIII]$\lambda\lambda$1907,1909, NIII]λ1750 and SiIII]λ1888 (see Figure 1.6 for an example).

They also concluded that line-ratios such as CIVλ1550 / CIII]$\lambda\lambda$1907,1909; NVλ1240 / HeIIλ1640 and NVλ1240 / CIVλ1550 do not individually allow to discriminate the nature of the ionizing source.

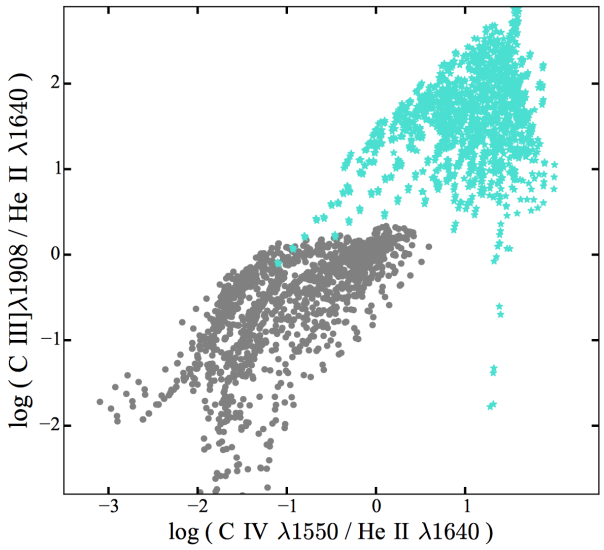

Figure 1.6: UV emission-line ratio diagnosis of HeII and two CELs of carbon from Feltre et al. (2016), using CLOUDY models. AGNs are represented by the grey dots and SFGs by the turquoise stars. The presented models span from the range of their adjustable parameters which include various values of metallicity, ionization parameter, density, dust-to-heavy element mass ratio, index of the power law (for AGN modelling) and the ionizing spectrum (see Feltre et al. (2016), Table 1.

They also found valuable diagnosis from ratios involving Neon emission lines ([NeIII]λ3343, [NeIV]λ2424, and [NeV]λ3426), which require high ionizing energies, and that allow to derive the physical conditions of the ionized gas. However, these lines are unlikely to be detected due to its faintness. In their studies, they used CLOUDY, a power law to model AGNs and the evolutionary synthesis code from Bruzual and Charlot (2003) (see Section 1.6.2), which includes the treatment of the interior and atmospheres of massive stars (including Wolf-Rayet stars and AGB stars), but which does not include binary effects and rotation. The main adjustable parameters of their ionizing source are the metallicity and the IMF with a mass cut-off that can reach 300 $M_{\odot}$. Their photoionized models do not include shocks that can also ionize the surroundings and produce AGN-like emission lines, which can enhance emission lines such as CIII] and CIV.

Jaskot and Ravindranath (2016) used different ESs (BPASS) and studied the effect of shocks on SFGs using also CLOUDY. They found that CIII]/HeII vs CIV/HeII separates star-forming regions from shock-ionized gas, and concluded that the CIII] doublet, which is frequently observed in low-metallicity SFGs and which can be detectable for a wide range of low metallicity conditions, is a promising emission line for diagnostic and characterization of galaxies at high redshift.

1.5 Searching for the first galaxies

Most of the high-redshift galaxies candidates have been found through ultra deep observations using the different filters of the WFC3 (IR) on board of the Hubble Space Telescope (e.g. Ellis et al. (2013)) and through the Lyman Break technique (LBT, Giavalisco (2002) for a review about the topic).

In the LBT, the selection of the candidates is made by their photometric colours, considering the strong discontinuity on the rest-frame UV continuum due to the absorption by neutral hydrogen of the IGM. Galaxies with high UV luminosity are easier to detect.

The LBT allows to select thousands of high-redshift candidates at once, where the confirmation can be made with follow-up optical spectroscopy (z = 5 - 7). However, it is often common to detect just one emission line in the spectra of these galaxies: Lyα. Some exceptions are strong UV emission lines, such as HeII or CIII] (e.g. Stark et al. (2015)).

The LBT technique has been extended to redshifts into the reionization epoch (e.g. Bouwens et al. (2011)), but around z $\sim$ 7, it is very difficult to obtain spectroscopic confirmation. These sources are observed on Earth at near-infrared wavelengths (which can be overcomed by using space telescopes). However, the main difficult is to recover the Lyα flux due to the amount of neutral hydrogen as we enter into the reionization epoch. Lyα is strongly scattered which suppresses a significant fraction of the total flux of the line.

The Lyα emission line then provides a probe of the condensation of primordial gas into the first galaxies. It is intrinsically the brightest UV emission line in the spectrum and it is commonly used to search for distant galaxies.

Progress have been made by searching for luminous Lyα emitters (LAE), which can be detected using surveys designed to spot these sources at specific redshifts (e.g. Matthee et al. (2015), Santos et al. (2016)) or using strong lensed galaxies (e.g. Stark et al. (2015), Stark et al. (2014)). Over the last years, the number of high-redshift galaxies at z $\sim$ 7 detected through their Lyα emission line has raised (e.g. Ouchi et al. (2009), Konno et al. (2014), Sobral et al. (2015), Matthee et al. (2017)), being brighter LAEs at the end of reionization epoch more common than previously thought (e.g. Santos et al. (2016)) and powered by strong ionizing sources (e.g. Matthee et al. (2017)).

Moreover, all high-redshift galaxies selected through other UV features show prominent Lyα line and an extremely hard radiation spectra. For example, some galaxies show CIV$\lambda\lambda$1548,1550 (e.g. Stark et al. (2015)), requiring the production of a large number of photons more energetic than 47.9 eV. The CIV emission line is associated with low luminosity narrow-line AGNs, but also has been found in dwarf galaxies at lower redshifts, probably powered by harder radiation fields associated with low metallicity stars (e.g. Vanzella et al. (2016)).

Several young galaxies, analogues of primeval galaxies, have been detected around z $\sim$ 2 - 3 (e.g. Amorín et al. (2017), Vanzella et al. (2016)). These galaxies exhibit the properties expected for high-redshift galaxies: they are compact star-forming, low-mass and low-metallicity systems, characterised by a strong UV spectra with bright emission lines, which indicates a hard radiation field produced by young and massive hot stars. Other possible analogues to high redshift systems are the "Green Peas", low-mass and compact galaxies with very active star formation, found at even lower redshifts (see e.g. Izotov et al. (2016)).

1.6 Modelling emission from high-redshift galaxies

1.6.1 Photoionization Codes

Photoionization simulation codes calculate the physical conditions of a gas irradiated by an external source of ionization and predict the resulting spectrum.

The first codes were developed in the late 60's with the aim of study low-density nebulae (e.g. Harrington (1968)). Several developments have been made since then, to include, for example improvements in the atomic processes, dealing with higher densities and higher photon energies and different optical depths. Codes can differ in their radiative treatment, geometry, equilibrium conditions, shocks treatment, atomic data, number of emission lines that can be treated, etc. Some examples of photoionization codes are CLOUDY (Ferland et al. (1998)), MAPPINGS-III (Sutherland et al. (2013)), MOCASSIN (Ercolano et al. (2003)), XSTAR (Kallman (1999)) and TITAN (Dumont et al. (2000)).

CLOUDY is an open source photoionization plasma simulation code, originally development in the late 70's to simulate gas conditions on black hole accretion discs to study the broad-line regions of AGNs (e.g. Rees et al. (1989)). CLOUDY incorporates all the physics from the first principles (with a constant update of its microphysical processes) to determines the physical conditions within a non-equilibrium gas. Despite the great variety of existent objects, from stars, to galaxies or clusters of galaxies, usually the density is so low on these environments that the plasma is collisionless and is not in thermodynamic equilibrium. For that reason, CLOUDY has been widely used by the astronomical community to simulate condition of other objects such as galactic HII regions, Planetary Nebulae and SFGs.

CLOUDY solves the 1D radiative transfer equations to simulate complex physical environments. It determines the physical conditions of the gas by solving the equations of statistical equilibrium, charge conservation, and conservation of energy, taking into consideration the relative population in different levels (the microphysics processes of astronomical plasmas are of great importance to reach better accuracies towards interpreting astronomical quantities). As a result, it determines the level of ionization, the gas chemical state and kinetic temperature, as well as the particle density and the full spectrum, with hundreds to thousands of emission lines (Osterbrock and Ferland (2006)).

Codes such as MOCASSIN can deal with more complex geometries computing for example 3D radiative transfer through Monte Carlo simulations. However, 1D codes allow faster computations (ideal for creating large grids of models) and are a good approximation to spatially unresolved objects when the exactly distribution of gas is not known (see Section 2.1.1 for a discussion about the gas geometry of high-redshift systems).

1.6.2 Evolutionary Synthesis models

Distant galaxies that hold unresolved stellar population are commonly described by their spectral energy distributions (SED), i.e. their energy as function of frequency or wavelength. Their analysis and understanding are on the basis of modern studies of galaxy formation and evolution, since the physical properties of the galaxies are encoded in their SEDs. They allow to estimate the properties of a galaxy such as its star formation history (SFH), stellar initial mass function (IMF), ionization

radiation field, total mass of stars, stellar metallicity, and the gas and dust contents.

Along with its interpretation through fitting techniques (first applied by Faber (1972)), synthetic SED models have been developed since the late 60's (e.g. Tinsley (1968)), based on stellar evolution theory and/or empiric models. These synthetic SEDs are Evolutionary Synthesis (ES) models (Maraston (1998)), also refereed as Stellar Population Synthesis (SPS), where the SFH is computed based on an IMF. Some examples are STARBURST99 (Leitherer et al. (1999)), PEGASE (Fioc and Rocca-Volmerange (1999)), FSPS (Conroy et al. (2009)) and ESs from Bruzual and Charlot (2003).

ES models can be used to derive the physical properties of a galaxy, predicting the integrated emission of stellar populations, interpreting observations, besides helping to delineate observational strategies. They are complementary to fitting techniques, where a code fits an observed spectrum with a model adding spectral components from a pre-defined base spectra, which can include evolutionary synthesis models, observed templates and individual stars (e.g. STARLIGHT, Cid Fernandes et al. (2005)). Novel approaches using genetic differential evolution optimization along with several numeric techniques (e.g. artificial intelligence strategies for spectra library selection) have been recently developed, accomplishing better SFHs fitting (FADO, Gomes and Papaderos (2017)).

Synthetic spectra concept

On the basis of a synthetic spectra of a stellar population is a simple stellar population, with a particular metallicity and abundance pattern, that evolves in time. The creation of stellar populations is based on isochrones, that specify the location of stars with the same age and metallicity on the Hertzsprung-Russel diagram; an IMF, which describes the initial mass distribution along the main sequence as function of metallicity; and stellar spectral libraries, that convert the stellar evolution results into readable SEDs. These are the building blocks of more complex systems. A review on ESs can be found in Conroy (2013).

The most updated models also include dust, which plays an important role obscuring the UV light, particularly important for SFGs with high metallicity. Another important feature is the nebular emission which comprises two components: a continuum emission from free-free, free-bound, and two-photon emission, and a recombination line emission, described in Section 1.3.4. Both components can be added to the SEDs as function of the physical state of the gas, using photoionization codes such as the ones mentioned in Section 1.6.1.

For SFGs, the UV flux is dominated by the light produced by young and hot stars and the surrounding ionized gas, which is responsible for nearly all the UV emission lines present in the spectra, therefore nebular emission is more important with high star formation rates, low metallicities and at younger ages, being very important for high-redshift galaxies (Schaerer and de Barros (2009)).

BPASS

In stellar populations that have formed stars continuously over its lifetime, both young and old stars contribute for a "stable" UV SED, while young starbursts, which contain larger portions of hot massive stars emit more ionizing photons. This is particularly important for low metallicity systems, where binary and rotation effects are more important, resulting in a modified ionizing spectra (Eldridge et al. (2008), Stanway et al. (2014)).

BPASS is the Binary Population And Spectral Synthesis code [1] (Eldridge and Stanway (2009)), that uses theoretical stellar evolution models combined with synthetic stellar atmospheres and include binary and rotation effects. Binary interactions create more hot helium and Wolf-Rayet stars due to the removal of the hydrogen envelope in primary stars. This enhances mass-losses, originating harder ionizing photons at later times than single star populations. Binaries also allow mass transfer to secondary stars increasing their mass and revitalization, and can lead to binary mergers producing single massive stars (Eldridge et al. (2008)). As a consequence it results in a top heavy mass function and more massive stars at later stages than expected, which increases the ionizing flux at later times ($\gtrsim$ 10 Myrs, Stanway et al. (2016), Figure 1.7).

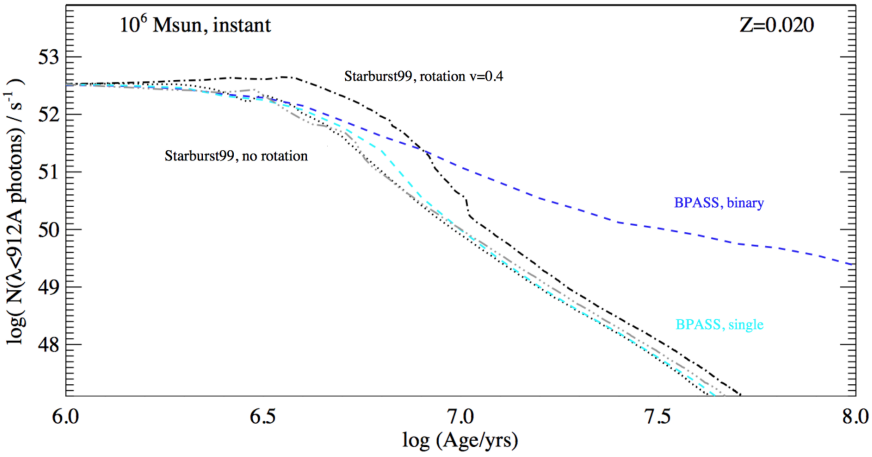

Figure 1.7: BPASS single and binary evolutionary pathways for an instantaneous star formation history, at $\sim$ 1.4 solar metallicity, and STARBURST99 with both a rotation parameter v = 0.4 and no rotation, for comparison. Note that the binary effects are even more important at sub-solar metallicities. From Stanway et al. (2016).

Rotation creates hotter stars and extends the star lifetime (Yoon and Langer (2005)). Rotation can result in stellar layer mixing, allowing high hydrogen burning (e.g. de Mink et al. (2013)). This effect is particularly important for high-mass stars ($\geq$ 20 $M_{\odot}$) and low metallicities (e.g. Eldridge et al. (2011)), where stellar winds are not strong enough to make these stars spin down and so they can remain rotating over their main sequence lifetime in a quasi-homogeneous evolution (QHE). This increases the SED flux at all ages.

When studying high-redshift galaxies, it is therefore necessary to use an ES that includes binaries and rotation effects, which can reproduce better the stellar populations of these galaxies.

1.7 Motivation and Goals

There is not a universal definition for "first galaxy" (Bromm and Yoshida (2011)). Observations and theories have been developed side by side to understand the formation and evolution of the first galaxies. For that reason, this work is based on the knowledge obtained from many observations but also from the physical concepts that are needed to build a "first galaxy".

[1] http://bpass.auckland.ac.nz

The first galaxies are expected to be powered by strong ionizing sources where the formation and evolution of massive stars have a major impact. These are also the most likely sources responsible for the reionization of the Universe.

The rest-frame UV of high-redshift galaxies show emission lines characteristic of massive stars, such as HeIIλ1640 Å and CIII]$\lambda\lambda$1907,1910 Å (e.g. Masters et al. (2014), Steidel et al. (2016), Stark et al. (2014)), indicative of a hard ionizing radiation field. These characteristics are more common in high-redshift galaxies than in the local ones. However, several analogues of high-redshift galaxies have been found at z $\sim$ 2 - 3, with high star formation rates and similar emission properties (e.g. Amorín et al. (2017)). These galaxies present low metallicity, indicating that they host predominantly POP III stars. Their study can help on the understanding of higher redshift systems and to establish whether the high-ionization emission of these sources is powered by SFG hosting hot and low-metallicity stars or AGNs, since both can potentially provide high energy photons. For "typical galaxies" at lower redshifts, such tools already exist using rest-frame optical emission line-ratios (e.g. BPT diagram). Diagnosis tools for the rest-frame UV emission lines, that take into consideration the properties of primeval galaxies, have just began to be developed using photoionization codes (e.g. Feltre et al. (2016), Gutkin et al. (2016)).

At high redshift, galaxies are unresolved and the emission we observe is the integrated light of different stellar populations (probably with different ages and metallicities). Their interpretation and comparison with the data request the use of an Evolutionary Synthesis (ES) code, which is based on known parameters, such as the initial mass function, metallicity and star formation history. Commonly, evolutionary synthesis codes differ from codes based on empirical observations of nearby stellar populations to theoretical stellar and atmosphere models. However, conventional ESs have shown not to be sufficient to explain the emission line strengths that have been detected in star forming galaxies with characteristics of primeval systems (e.g. Steidel et al. (2016)). Conventional ESs, such as STARBURST99, lack on extensive details of massive star populations and the strengths of the lines are difficult to reproduce with these models (Shapley et al. (2003)). ESs that include binary stars and rotation effects, as well as low metallicities, are then needed to explain the strengths of these lines at high-redshift (e.g. Eldridge and Stanway (2012), Steidel et al. (2016)). Moreover, ESs which include binaries and rotation are essential to understand the reionization history, since they can explain the "missing photons" necessary for the reionization (Ma et al. (2016)).

In this work we use the photoionization plasma simulation code CLOUDY 13.03, last described in Ferland et al. (2013), to simulate the gas conditions in high-redshift galaxies and to predict the emission line spectra of these low density, almost dust-free and low-metallicity systems.

We compute a grid of models to simulate star forming galaxies using both a black body shape (which does not suffers the limitations introduced by the approximations and lack of accuracy of stellar models) and the BPASS v2.0 ESs. To understand low metallicity, high-redshift SFGs, it is necessary to take into account massive stellar evolution and its interpretation. BPASS uses theoretical state-of-the-art stellar evolution models combined with synthetic stellar atmospheres that include binary and rotation effects. Binary evolution extends the lifetime of stars, increasing the influence of very blue stars in the spectra.

Including the effects of massive stars is also important to understand the nature high-redshift galaxies, such as CR7 (Sobral et al. (2015)), selected through its strong Lyα emission line, presenting

also HeII. The absence of other emission lines suggests a metal-free POP III stellar population. Stellar evolution models can help to address the nature of these galaxies (Bowler et al. (2016)).

We also create models to simulate nebular emission from AGNs using a power-law shape. The presence of supermassive black holes at high redshift create powerful AGNs that present hard ionizing spectra and are difficult to distinguish from SFGs with such characteristics.

The key goal of this work is to derive the signatures of the first galaxies using UV emission line-ratios, helping on the understanding of the nature of these sources and make observational predictions for upcoming telescopes, such as the James Webb Space Telescope. At high redshift the total flux of the Lyα emission line is attenuated by the intergalactic medium, being necessary to study the behaviour of other UV emission lines that allow to understand these high-redshift systems.

In Chapter 2 we describe our SFGs and AGNs CLOUDY models in detail and in Chapter 3 we present the main differences between our models, as well as our modelling results using UV line-ratios to explore the characteristics of both ionizing sources.

In Chapter 4 we analyse analogues of primeval galaxies around the peak of star formation of the Universe (e.g. Sobral et al. (2014)). We derive the physical properties of young SFGs from Amorín et al. (2017) and bright Lyα emitters from Sobral et al. (in prep). We also present observational interpretation of high-redshift galaxies expected to be observed with future telescopes such as the James Webb Space Telescope. We then extend our modelling results to galaxies at higher redshift, where we used our CLOUDY models to study the Lyα escape fraction in galaxies at z $\sim$ 6 - 7 (presented in Matthee et al. (2017)).

In Chapter 5 we present our study of galaxies from the HiZELS (High-z Emission line survey), which we fully analyse, and select two SFGs at z $\sim$ 1.5 to apply our modelling results.

In Chapter 6 we summarise our conclusions.

Chapter 2

CLOUDY photoionization modelling

To perform photoionization simulations, the physical properties of the **gas** and the external **source of radiation** need to be specified.

A general description of the properties of the gas cloud used in this study is presented in Section 2.1. In Section 2.2 we describe other parameters and commands common to all models. The external radiation field that strikes the cloud (i.e. the incident radiation field) is described in Section 2.3.

2.1 The gas cloud

To perform accurate radiative transfer simulations, CLOUDY needs information about the environment where the light of the ionizing source is passing through. The main parameters that must be specified to simulate the gas cloud are the **geometry** of the gas, the gas **density**, its **chemical content** and its **grain content**.

2.1.1 Geometry of the gas cloud

CLOUDY has two geometry limiting cases: an open geometry (plane-parallel) and a closed geometry (spherical). In an open geometry the diffuse emission from the illuminated face of the cloud escapes from the system without striking other clouds, whereas in a closed geometry the emission from the illuminated face of the cloud strikes the gas on the opposite side of the cloud (Figure 2.1).

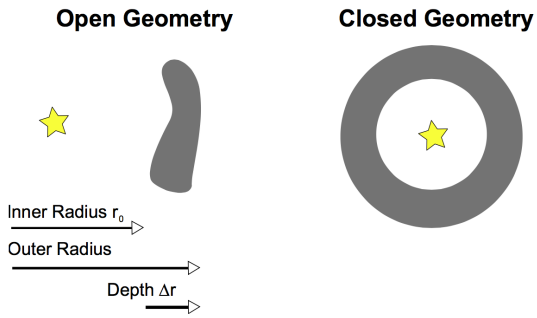

Figure 2.1: CLOUDY gas geometries (both one-dimensional) as illustrated in the documentation of CLOUDY last described in Ferland et al. (2013).

The inner radius (r_0) is the distance from the centre of the ionizing source to the illuminated face of the cloud. An outer radius can be specified defining that way a depth for the cloud. In an open geometry the inner radius is much larger than the thickness of the cloud.

In this study we used an open geometry to simulated the gas beyond the broad line region of AGNs (Section 2.3.2). We let the inner and the outer radius with the CLOUDY default values, respectively: 10^{30} cm and 10^{31} cm (i.e. with an infinite value for practical purposes). This results in a plane-parallel geometry. Ionising photons that escape from the central region can ionize the gas in low density areas (in the narrow line region) which can extend over great scales $\sim 10^2 - 10^4$ pc (e.g. Osterbrock and Ferland (2006)).

To simulate SFGs we used a closed geometry, where the central object is small relatively to the gas cloud. The closed geometry was set with the *sphere* command. By default this also sets an expanding geometry where the line photons are not absorbed by the gas on the opposite side of the cloud. In a closed geometry an inner *radius* needs to be specified.

Superstar clusters in H II regions in galaxies of the Local Group are enclosed in regions ≤ 10 pc (Hunt and Hirashita (2009)). The bulk region of star formation in the most luminous star formation region in the Milky Way is also confined to an inner radius of ~ 10 pc (Longmore et al. (2014)). For that reason we set an inner radius of 10 pc and let the outer radius with the default value. However, we explore the influence of choosing a different geometry with our black body models setting an inner radius of 1 pc. This will have influence essentially on the ionization parameter at the Strömgren radius but does not have great influence on line-ratios by themselves. Other authors used different values for the inner radius with CLOUDY. While Byler et al. (2017) fixed an inner radius of $\sim$ 3pc, Gutkin et al. (2016) followed the Charlot and Longhetti (2001) approach to simulate SFGs setting an inner radius of $r_0 \leq 0.01$ pc to ensure spherical geometry. However, Gutkin et al. (2016) parameterized their models in terms of the ionization at the Strömgren radius and it is expected that the choice of the inner radius has a negligible influence on the results (Charlot and Longhetti (2001)). More details about the radiation field can be found in Section 2.3.

Assuming that the central source produces ionizing photons at the rate of Q(H) and the hydrogen cloud is homogeneous, isothermal and is fully ionized, the size of the ionized region is proportional to Q(H) and to the density of the gas (n_H), resulting in the Strömgren sphere (Osterbrock and Ferland (2006)):

$$Q\left(\mathrm{H}^0\right) = \frac{4\pi}{3}\, r_0^3\, n_\mathrm{H}^2\, \alpha_B \;\; [\mathrm{s}^{-1}], \tag{2.1}$$

where α_B is the hydrogen recombination coefficient correspondent to the transitions for the excited levels in case B recombination. Here we assume an optical thick ionized region (case B recombination) where all the photons produced through recombination (e.g. Lyα and Balmer series) are reabsorbed within the gas cloud contributing for the emission line.
We note that our models create a thick shell for $\Delta r/r_o < 3$ and a sphere for $\Delta r/r_o \geq 3$, depending on the properties of the ionizing source and the gas density and metallicity.

The code works by dividing the cloud into a large number of thin layers (zones). CLOUDY's default limit is 1400 zones, however the calculations usually stop before reaching this value, once the code has converged. Our calculations stop when the lowest temperature is reached (Section

2.2.2) performing one more iteration over the model after that (Section 2.2.2).

More complex geometries can be used, where the code works on volume elements within the cloud to simulate three-dimensional geometries (e.g. CLOUDY 3D, Morisset (2006)).

Despite the attention towards the use of different geometries to simulate AGNs and SFGs, the geometry computed should have only secondary effects in the predicted emission line spectrum, usually at 10 % level (CLOUDY documentation, last described in Ferland et al. (2013)).

In addition, as our predictions are based on line-ratios and not line intensities by themselves, the choice of a particular geometry is not expected to have a major influence in the final results.

2.1.2 Density of the gas

The density of the gas cloud is defined in terms of the hydrogen density and it is a fundamental parameter in CLOUDY's simulations because hydrogen plays an important role in astrophysical plasmas due to its large abundance. The total hydrogen density is the combination of all protons in the atomic, ionic and molecular forms, where $n(\mathrm{H}_{other})$ represents the hydrogen contained in all other molecules:

$$n\left(\mathrm{H}\right) = n\left(\mathrm{H}^{0}\right) + n\left(\mathrm{H}^{+}\right) + 2n\left(\mathrm{H}_{2}\right) + \sum_{other} n\left(\mathrm{H}_{other}\right) \left[\mathrm{cm}^{-3}\right] \tag{2.2}$$

The density was defined with the command *hden*, which sets the initial hydrogen density. It is possible to set a density law, however we used constant density throughout the gas cloud, assuming that all the ionized, atomic and molecular gas are in pressure equilibrium. Even though the electron and molecular fractions can variate with the depth of the cloud (and so the total particle density is not exactly constant), there is a direct relation between a constant density and the ionization parameter (Davidson (1977)). Byler et al. (2017) compared CLOUDY models with a constant density law against an isobaric density law $P_{gas} = n_{tot} k T_e$ and found that the results have not changed by more than a few percent, being the effect more important in other plasma simulations codes such as MAPPINGS-III (Groves et al. (2004)), which is a pressure-based photoionization code. Density is a fundamental parameter in CLOUDY simulations whereas for MAPPINGS-III is the pressure.

We computed our models using six different gas densities spanning from 10^2 to 10^6 cm^{-3} (100, 500, 1000, 5000, 10000 and 100000 cm^{-3}). These values are in the range of observed densities in extragalactic H II regions (e.g. Hunt and Hirashita (2009)) and are within the values used by Feltre et al. (2016) and Gutkin et al. (2016).

Filling factor

The filling factor accounts for how clumpy the gas cloud is, and translates the fraction of the volume which contains the gas. Establishing a filling factor sets the gas regions with the defined density and the surrounding areas with zero density (i.e. vacuum). Changing this factor alters the effective path length of the ionizing photons. We defined a filling of 1, which means that the gas assumes the available cloud volume. Moreover, since we are using a constant density law, changing this factor while variating the density values would create the same ionizing conditions that we achieve with our models.

2.1.3 Chemical Abundances

After hydrogen and helium, which are related to the Big Bang nucleosynthesis itself, oxygen followed by carbon are the most abundant elements in the Universe. They play an important role in the chemical evolution of the Universe. As a galaxy evolves its chemical composition changes over time. Successive generations of massive stars contribute to the enrichment of the ISM with heavier elements as they explode in supernovae or via other mass-loss processes.

At high redshift chemical abundances reflect the transition from POP III to POP II stars. The chemical composition of a galaxy can therefore be a tracer of its star formation history and its state of evolution (e.g. Wheeler et al. (1989)).

The chemical composition of the gas used in this study was adapted from the default CLOUDY chemical composition (Appendix A, Table A.1), where the code considers in detail the 30 lightest elements. Throughout this work we assume a solar metallicity of $\log(O/H)+12 = 8.69$.
The CLOUDY command used to modify the CLOUDY default composition was *metals* which scale all the elements heavier that helium, relatively to hydrogen. Carbon and nitrogen abundances were set independently in relation of oxygen abundance (but taking into consideration the effect of the *metals* command) with the commands *element abundance carbon* and *element abundance nitrogen*. All the values used to scale the elements were given in log units and they are absolute values, i.e. they are directly related to hydrogen. The chemical composition is printed in the header of each calculation and can be confirmed in the CLOUDY output files. The models span from solar to extremely low metallicity.

In this study we have treated the carbon abundance in a similar way as described by Carigi and Peimbert (2011) and the nitrogen abundance with the analytical function from Groves et al. (2004).

Other authors have also used different approaches to deal with the abundance of these elements. For example, Gutkin et al. (2016) variates the C/O ratio in 9 steps and keeps N as function of O (at fixed interstellar metallicity) using Groves et al. (2004) expression, while Vale Asari et al. (2016) variates N/O and keeps C as a function of N. These approaches account for chemical observational uncertainties but create huge grids of models.

Carbon to Oxygen abundance ratio

Carbon production is thought to be primarily due to helium burning through triple-α reaction in massive stars ($M > 8M_{\odot}$) (e.g. Henry et al. (2000a)), and secondarily by low to intermediate mass stars ($1M_{\odot} < M < 8M_{\odot}$) (e.g. Henry et al. (2000b)). By contrast, oxygen is produced only by massive stars. For that reason the carbon to oxygen abundance ratio (C/O) reflects the chemical enrichment history of the galaxies.

Carbon production in metal-poor galaxies, which contain young stellar populations, should be dominated by early enrichment from massive stars, whereas as the metallicity of a galaxy increases, galaxies start to suffer contributions also from intermediate-mass stars (Garnett et al. (1995)). Massive binary stars can have an important role in the process since binary interactions can promote great wind-driven mass loss (e.g. Eldridge and Stanway (2012), Berg et al. (2016), Henry et al. (2000a)). Rotation may play an important role (e.g. Maeder and Meynet (2003)), boosting secondary stars to high rotation rates due to its binary interaction with another massive star.

At very early stages of galaxy evolution, carbon enrichment may be dominated by POP III stars (e.g. Cooke and Madau (2014)), which elevates the C/O ratio (e.g. Fabbian et al. (2009)). At later stages, secondary carbon contribution arises also from low-intermediate mass stars so there is a general agreement that the C/O ratio increases with metallicity (e.g. Berg et al. (2016)).

Observations of low metallicity galaxies at z $>$ 1 show strong emission lines of carbon (e.g. Erb et al. (2010), Stark et al. (2014)). This trend is also seen in metal-poor damped Lyα systems (DLAs) in their absorption lines. Moreover, C/O observations of DLAs show an increasing of C/O abundance with decreasing metallicity, i.e. at very low oxygen abundance (e.g. Pettini et al. (2008), Cooke et al. (2012)).

The model used in this work was inspired in the CP model (Carigi and Peimbert (2011)). The CP model predicts better the rise in the log(C/O) for log(O/H)+12 $<$ 6.8, seen for DLAs and halo stars, than other models such as Mollá et al. (2015) and Henry et al. (2000a) (see Berg et al. (2016), Figure 8).

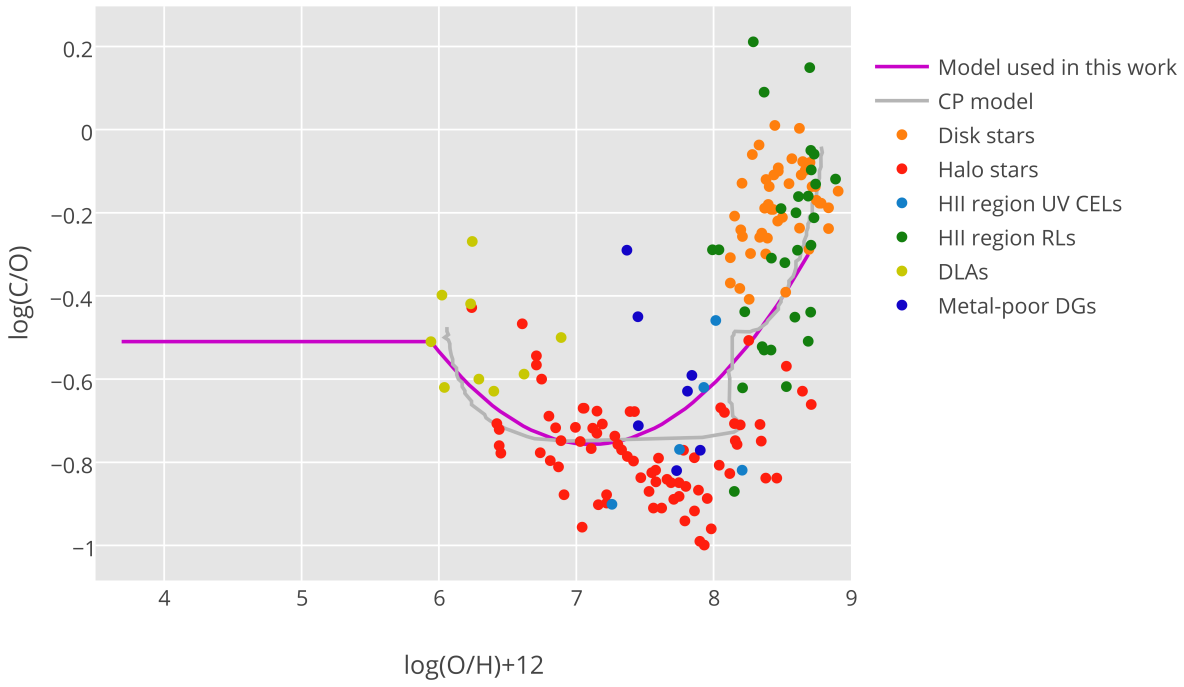

Figure 2.2: Carbon to Oxygen abundance ratio model within the range of metallicities used in this work. The model is based on several measurements for a variety of objects: Milky Way disk stars from Gustafsson et al. (1999) and halo stars from Akerman et al. (2004), Spite et al. (2005) and Fabbian et al. (2009); H II regions of SFGs calculated with UV CELs (Collisionally excited lines) from Kurt et al. (1999) and Dufour et al. (1982) and recombination lines (RLs) from Esteban et al. (2002), Esteban et al. (2009), Esteban et al. (2014), López-Sánchez et al. (2007), Pilyugin and Thuan (2005), García-Rojas and Esteban (2007). Damped Lyα systems (DLAs) are from Cooke et al. (2011) and high-ionization H II regions of dwarf galaxies (Metal-poor DGs) from Berg et al. (2016). For reference we show the CP model from Carigi and Peimbert (2011).

We fixed our solar value to $\log(C/O)_{\odot}$ = -0.3 (calculated from Appendix A, Table A.1) and the value of the lowest metallicity DLA ($\log(C/O)$ = -0.51), and we performed a polynomial fit to the data in-between these two points.

This way, between $\log(O/H)+12 = 5.94$ ($Z \sim 0.002\ Z_{\odot}$) and $\log(O/H)+12 = 8.69$ ($Z = Z_{\odot}$) our model can be simply described by a 2-degree polynomial function:

$$\log(C/O) = 0.18\ x^2 - 2.59\ x + 8.44, \tag{2.3}$$

where $x = \log(O/H)+12$. We used an oxygen abundance for the solar metallicity of $\log(O/H)_{\odot}$ = -3.31.

For reference we show the CP model which is only based on the halo and disk (dwarf) stars measurements and that keeps a flatter trend between this metallicity range. While our fit is relatively close to the CP model, the decrease of the $\log(C/O)$ value as the metallicity decreases is not so abrupt in the same range of metallicities, favouring the metal-poor DGs and H II region UV CELs.

Due to a lack of observations, for metallicities below $\log(O/H)+12 = 5.94$ we defined a threshold value of $\log(C/O)$= -0.51, which corresponds to the value of the lowest metallicity DLA of the sample. For reference $(C/O)_{\odot} = 0.5$.

Nitrogen to Oxygen abundance ratio

Comparing to carbon, nitrogen production and abundance across metallicity is relatively better understood. Nitrogen can be created primarily by nucleosynthesis through the conversion of carbon and oxygen in CNO cycles of hydrogen burning or secondarily from the CO products from previous stellar generations. While primary production occurs usually in intermediate mass stars ($4M_{\odot} < M < 8\ M_{\odot}$), secondary production can occur in stars of all masses.

Several studies at metallicity $\log(O/H)+12 \leq 8.3$ in H II regions of dwarf galaxies revealed that N/O is independent of O/H, implying a primary nitrogen origin (e.g. Thuan et al. (1995)). At even lower metallicity, for example in blue compact galaxies in H II regions with $\log(O/H)+12 \leq 7.6$, the scatter in the N/O values is very low (scatter values are commonly attributed to the different production channels) suggesting that nitrogen production is mainly made in massive stars (Thuan et al. (1995), Izotov and Thuan (1999)). With decaying metallicity, it is expected that massive stars produce less nitrogen and the low-metallicity plateau reflects the assumption of this primary production by massive stars (e.g. Vincenzo et al. (2016)). At higher metallicities the secondary production of nitrogen increases as the metallicity increases, increasing also the nitrogen abundance (e.g. Vincenzo et al. (2016)). To take into account such effects we used an the analytic function from Groves et al. (2004) which combines both production channels and can be related to that of oxygen through the expression:

$$N/H \approx O/H\,[10^{-1.6} + 10^{(2.33+log(O/H))}] \tag{2.4}$$

This function was obtained with three datasets: two from Mouhcine and Contini (2002) based on measurements on H II regions of galaxy samples and starburst nuclear galaxy surveys, and one from Kennicutt et al. (2003) based on emission-line measurements of individual H II regions within

the spiral galaxy M101. The function usually explains well the data. It decreases as the metallicity decreases, staying constant approximately below log(O/H)+12 = 7, but tends to give higher N/O values at high metallicities than the ones observed (Groves et al. (2004)).

For that reason, when applying the Groves' function we set a nitrogen abundance for the solar metallicity of $\log(N/H)_{\odot}$ = -4.196, instead of the CLOUDY default nitrogen abundance on Table A.1 ($\log(N/H)_{\odot}$ = -4.07). We have not scaled Groves' function, such as Gutkin et al. (2016) and Feltre et al. (2016), because it creates higher log(N/O) at low metallicities (log(N/O) = -1.5). This way at low metallicities our log(N/O) = -1.6, identical to Groves' value.

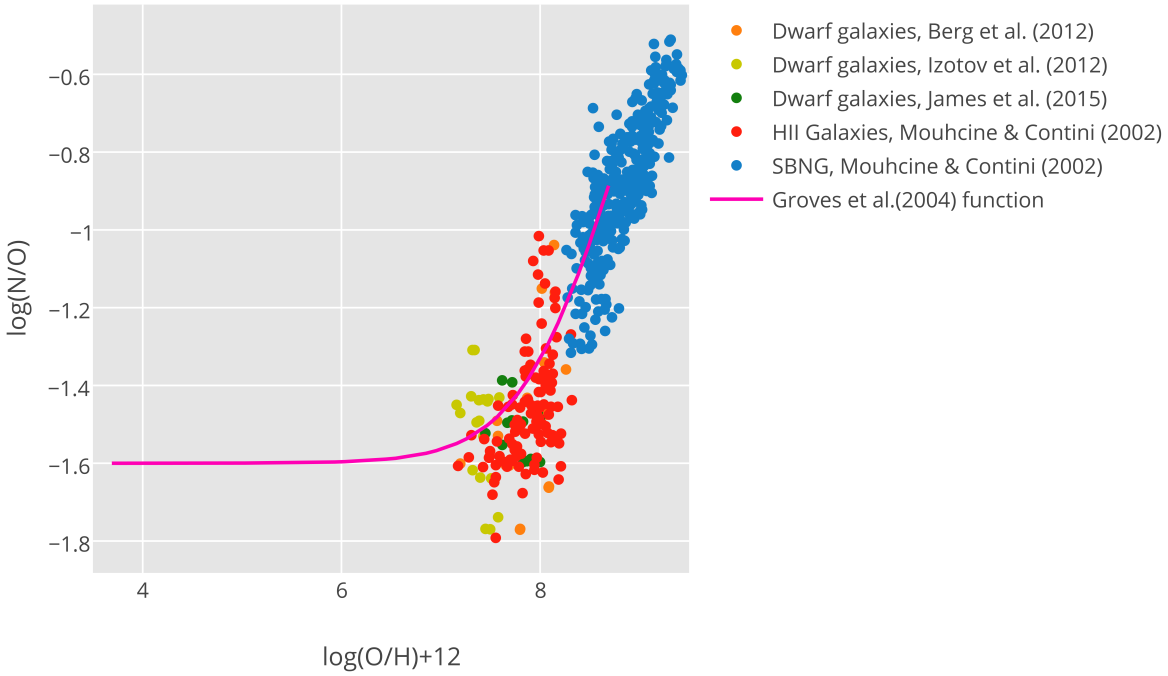

Figure 2.3: Range of log(N/O) values against oxygen abundance used in this work, using Groves et al. (2004) function. The dots correspond to measurements in samples of blue, diffuse star forming dwarf galaxies by Izotov et al. (2012), Berg et al. (2012) and James et al. (2015). H II galaxies and starburst nuclear galaxy sample (SBNG) consist both of compilations of several surveys by Mouhcine and Contini (2002).

For reference $(N/O)_{\odot}$ = 0.13 (lower than the CLOUDY default value).

2.1.4 Grains

Grains are not part of CLOUDY default gas composition and were not included in our CLOUDY models (although they might have survived in such environment) since we are only concerned with dust-free, very low metallicity galaxies, and with emission-line ratios.

Grains (e.g. graphite, silicates) are a fundamental constituent of the ISM of galaxies like the

Milky Way, where heavy elements produced by nucleosynthesis in the interior of stars can produce solid particules, that efficiently absorb UV light re-emitting in the IR. At high redshift, galaxies have young stellar populations. The dust-to-gas ratio rapidly decreases towards these redshifts (Dunlop et al. (2013)). Such evidence can also be seen on the steepening of early galaxies UV spectra.

Note that for extreme compact objects with $n_H > 10^3$ cm^{-3} the effect of dust extinction should to be more accentuated (Hunt and Hirashita (2009)). We have computed our models using a wide range of n_H values but we are mainly interested in emission lines produced in low density environments.

2.2 Other parameters

2.2.1 CMB and Cosmic ray background

CMB

Other continuum sources of radiation such as the cosmic microwave background (CMB) may affect line emissivities across the spectrum (Chatzikos et al. (2013)) even though these effects are more accentuated at longer wavelengths. However, the radiation field should be fully described between 1.001×10^{-8} Ryd $\leq h\nu \leq 7.354 \times 10^{6}$ Ryd. Adding the CMB is a way to satisfy this condition. The *CMB* command enters an isotropic source of radiation adding the shape and the intensity of the cosmic microwave background.

Cosmic Ray Background

Galactic background cosmic rays were included with the *Cosmic Ray Background* command. Cosmic rays heat and excite and/or ionize the gas and should be included if the simulation is extended into molecular gas (Shaw et al. (2005)). Molecules are present in CLOUDY simulations by default, being the effect particularly important for regions where hydrogen is predominantly molecular.

Cosmic rays were suggested as potential contributors for the reionization however their role in the process is still a debate. Recent studies, with POP II stars, point towards cosmic rays spectra being orders of magnitude below the UV radiation, contributing mainly as a heating source of the IGM (Leite et al. (2017)), with the justification that POP II stars dominate SFR at any redshift (e.g. Pallottini et al. (2014)). Other models using low-metallicity stars (mainly POP III) suggest a strong dependence on the efficiency to which cosmic rays are accelerated out of the galaxies (Rollinde et al. (2006)).

2.2.2 Iterations, Stopping criteria and Save commands

Iterations

By default, CLOUDY iterates just one time over each model. We performed two iterations, which were defined with the command *iterate*, in order to account for the radiative transfer effects affecting the emission line formation. This is mainly important for higher densities since the total optical depth is not known on the first iteration.

Stopping criteria

Our calculations stopped when the lowest effective temperature was reached. CLOUDY default value for the lowest temperature is 4000 K. We have not set any stopping criteria to end our calculations but rather used the default value. Setting this value to a lower temperature would only be of interest if we were studying, for example, IR lines with low excitation potentials. UV emission lines from ionized gas are generally formed in a gas with higher temperature. For that reason, we kept the default CLOUDY stopping criteria of 4000 K where nearly all ionization radiation has been already attenuated and the calculations already include contributions to the UV (and optical) spectra.

Save Commands

The save commands create files that can be used later.

Save commands were used to *save the continuum* which returns the photon energy in Rydbergs vs the energy flux νF_ν in erg cm^{-2} s^{-1}.

Other save commands were used, which include *save element* commands, to save the ionization structure (per zone) for the last iteration for different elements; *save lines emissivity* to save all the emission lines defined as a function of the depth in the cloud; *save optical depths* to save the optical depth for the computed geometry; *save heating* and *cooling* contributors for each zone; *save radius* for saving the distance to the central object; *save physical conditions*, which include saving the temperature, electron density, heating, radiative acceleration and the filling factor for each zone; and *save overview*, which saves the thermal and ionization structure of the cloud.

The line emissivities used in this study were read from the emissivity file where are all the lines defined in the input file were stored. The reason for this is that some of these emission lines have very low intensities, and they are not printed in the general CLOUDY output file. They were read using PyCloudy (Section 2.2.4) which computes the emissivities integrated over the volume, corresponding to the line intensity for the last radius computed. This would not represent a problem since we are focused on emission line-ratios.

2.2.3 Emission lines

The emissivity of relevant UV and optical emission lines (see Section 1.4) were saved in the emissivity file described above. The labels used by CLOUDY to identify each line can be found in Appendix A, Table A.2. We used the intrinsic line intensities and performed all the calculations from them. As grains are not present the emergent line intensities and the intrinsic line intensity will be the same. The emergent intensities do not include any reddening effects, since this is calculated from the grain albedo to compute the spectrum that emerges from the illuminated face of the cloud.

We are focused mainly on UV high-ionization emission lines but we also computed emission lines with lower ionizations and optical emission lines that can be used for future diagnostics (Table 2.1).

Table 2.1: High to moderate ionization ultraviolet and optical emission-lines

Low-to-Moderate Ionization Lines		High-Ionization Lines	
Emission-line	χ(eV)	Emission-line	χ(eV)
N III 1750 Å	29.6	N V 1240 Å	77.4
Lyα 1216 Å, Hβ 4861 Å, Hα 6563 Å	13.6	O IV] 1407 Å	54.9
C II] 1335 Å	9.29	N IV] 1485,1486 Å	47.4
O III] 1661,1666 Å, [O III] 4959,5007 Å	35.1	C IV 1548,1551 Å	47.9
N III] 1750 Å	29.6	He II 1085 Å, 1640 Å	54.4
Si III 1888 Å	16.3		
C III] 1907,1910 Å	24.4		
Mg II 2796,2803 Å	7.6		
[O II] 3727,3729 Å	13.6		
[N II] 6548,6583 Å	14.6		

2.2.4 Python tools

PyCloudy

PyCloudy[1] (Morisset (2013)) is a python library used to manage CLOUDY inputs and outputs. It allows to define CLOUDY instructions to run a model and extract the results afterwords. It is extremely useful to compute grids of models, running CLOUDY in parallel. PyCloudy can also compute pseudo 3D models and allows to interact with the 3MdB database (Mexican Million Models dataBase, Morisset et al. (2015)). PyCloudy needs several python libraries to run: Numpy and Scipy (to generic scientific computing), Matplotlib (to plot), Image (to create coloured images) and PyNeb (to change the atomic physics). To interact with the 3MdB it also needs the library PyMySQL (or MySQL). In this work we used PyCloudy version 0.8.54.

3MdB

The concept behind the 3MdB is to store the results of the models into a database and easily read only the desired output files. For huge grids of models (e.g. 10^3 to 10^6 models) reading all the output files would be too much time and memory consuming. The 3MdB was examined to evaluate its potential but was not used to store our current models. The models stored on the database were not used as well because their physical parameters (e.g. ESs or the range of metallicities) are not the ones desired for this study. Amorín et al. (2017) used the HII-CHI-MISTRY models (Pérez-Montero (2014)) stored on the 3MdB. Their results are discussed in Section 4.1.

[1] http://pythonhosted.org/pyCloudy/

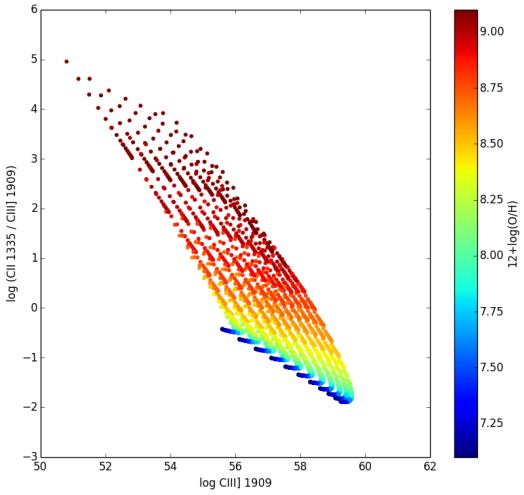

Figure 2.4: Example of HII-CHI-MISTRY models (Pérez-Montero (2014)) stored in the 3MdB. The "stripes" pattern result from different ionization parameters. From ionization parameters of -1.5 at right to -4.0 at left.

Tools like the 3MdB are very useful to store and read CLOUDY models and can be accessed easily by everyone. However, the models are usually created with one purpose, which involves defining all the input and output parameters beforehand (e.g. a specific emission line must be defined when creating the models), therefore its use is limited to satisfying several conditions.

2.3 The radiation field

The external radiation field that strikes the cloud (i.e. the incident radiation field) is defined by its **intensity** and its **shape**.

The radiation field can be created using a black body, a power law, or other SEDs, such as built-in SEDs or user-defined SEDs. We use black bodies and BPASS SEDs to investigate SFGs (Section 2.3.1) and a power law slope to model AGNs (Section 2.3.2).

The radiation field is fully described between 1.001×10^{-8} Ryd $\leq h\nu \leq 7.354 \times 10^{6}$ Ryd. In our models the incident radiation field is the major source of heating and ionization, with small contributions from background radiations (Section 2.2.1) which generate an isotropic continuum orders of magnitudes below.

There are several ways of specifying the intensity of the incident radiation field.

Here we define the ionization parameter (U), which sets the dimensionless ratio of densities of ionizing photons to hydrogen:

$$U \equiv \frac{Q\,(\mathrm{H})}{4\,\pi\,r_o^2\,n\,(\mathrm{H})\;c} \tag{2.5}$$

Where Q(H) [s^{-1}] is the number of hydrogen-ionizing photons emitted by the source, r_o [cm] is inner radius of the cloud, n(H) [cm^{-3}] is the hydrogen density (which includes ionized, neutral, and molecular hydrogen) and c is the speed of light.

The ionization parameter is set in CLOUDY using log units and it is a useful quantity in plane-parallel, low-density and constant density models, where there is a direct relation between models with different photon and gas densities but the same ionization parameter (Davidson (1977)).

In a plane-parallel geometry, where the inner radius is larger than the Strömgren sphere, the ionization parameter at the inner radius (U_0) will be similar to the ionization parameter at the Strömgren radius (U_S).

For AGN modelling we used the ionization parameter to define the intensity of the radiation field and we varied this parameter between -4 $\leq$ log U $\leq$ -1, where U = U_0 = U_S.

For closed geometries, given a U_0, CLOUDY then computes the ionization parameter at the Strömgren radius. The ionization parameter can then be used as an adjustable parameter (e.g. Groves et al. (2004)). Running models with different U_0 values but at fixed density and inner radius, produces different values for Q(H) originating different ionizations for the cloud. To create models using a black body shape we varied the ionization parameter between -4 $\leq$ log U_0 $\leq$ -1, that produces ionization parameters at the Strömgren radius of -4.5 $\lesssim$ log U_S $\lesssim$ -1, which is in the range of observed ionization parameters for local starburst galaxies (-3.5 $\leq$ log U $\leq$ -1.5, Rigby and Rieke (2004)). The values used are commonly adopted to model both SFGs and AGNs (e.g. Feltre et al. (2016), which uses -4 $\leq$ log U_S $\leq$ -1). Note that usually U_0 is larger than U_S for an inner radius smaller than the Strömgren radius (which will depend on the geometry of the cloud, in particular on the density and inner radius, but also on the metallicity).

For SFG modelling using BPASS models we used the value of Q(H) itself, which is the total number of ionizing photons emitted by the central object [s^{-1}]:

$$Q\,(\mathrm{H}) = 4\,\pi\,R_{star}^2\,\int_{\nu_1}^{\nu_2}\frac{\pi\,F_\nu}{h\,\nu}\,d\nu. \tag{2.6}$$

Changing the density at fixed Q(H) value and inner radius, computes different values for the ionization parameter. Each of the BPASS SEDs used has an intrinsic shape which influences the UV ionizing flux and the resulting ionization parameter (as well as the generated emission-lines), as explained in the next sections.

2.3.1 Star Forming Galaxies

Stars can ideally be approximated to a black body, where the peak of emission is shifted towards shorter wavelengths to hotter stars according to the Wien's law λ_{max} T = 2.89×10^{-3} m K.

Our first approach is to model SFGs using a black body incident radiation field varying the black body temperature from 20000 to 150000 K in 14 steps. This was done with the CLOUDY command *Blackbody* followed by the temperature value in Kelvin.

Our second approach is to use an ES to model SFGs. In this study we used the last version of BPASS code (BPASS v2.0, e.g. Stanway et al. (2016)) which uses a combination of stellar evolution models derived from the Cambridge STARS code (Eggleton (1971)) described in Eldridge et al. (2008), that includes evolutionary pathways from binary stellar models with rotational effects. These models can be downloaded from BPASS website [2].

[2]http://bpass.auckland.ac.nz/2.html

Each set of models contain both the continuous and instantaneous star formation histories. Here we only consider models with instantaneous star formation histories, in which all the stars are formed in a single epoch and evolve without new star formation. Continuous star formation models hold older stellar populations that will tend to boost the optical continuum reducing the strength of emission lines in the UV, which is principally sensitive to young stellar populations, since the hardening of UV photons from post-AGB stars can account for high-ionized species.

We used the BPASS v2.0 IMF fiducial models, built with a broken power law with a slope of -1.30 between 0.1 $M_\odot$ and 0.5 $M_\odot$ and -2.35 from 0.5 $M_\odot$ to 300 $M_\odot$.

Some nearby star forming regions show evidence of stellar masses above 100 $M_\odot$ that can extend to 300 $M_\odot$ (Crowther et al. (2010)). Extending the IMF to higher mass limits such as 300 $M_\odot$ predicts better the ionizing fluxes seen in galaxies at high redshift, such as in the ones from Matthee et al. (2017) and Nakajima et al. (2016)), rather than an IMF with a lower upper mass cut-off of 100 $M_\odot$ (Stanway (2017). A flatter slope below a stellar mass of 0.5 $M_\odot$ favours a more massive population rather than a Salpeter-like IMF (Stanway et al. (2016)). It is expected that the first galaxies have a stellar population with a top-heavy IMF which translates a higher proportion of massive stars compared to low-mass stars which have resulted from stellar mass transfer and binary mergers. This is translated in the BPASS ionization flux seen in Figure 1.7.

BPASS stellar atmospheres: metallicities and ages

BPASS v2.0 stellar atmospheres comprise 12 metallicity mass fractions from Z = 0.001 to Z = 0.040 ($7.6 < \log(O/H)+12 < 9.0$). Z = 0.020 ($\log(O/H)+12 = 8.8$) corresponds to the abundances of local galactic massive stars (Nieva and Przybilla (2012)) and Z = 0.014 ($\log(O/H)+12=8.69$) to the solar composition (Asplund et al. (2009)). Conventionally Z=0.020 is assumed to be the reference value for massive stars that have formed more recently than the Sun. We have assumed in our models that the solar metallicity is $\log(O/H)+12 = 8.69$ and we use Z = 0.014 for coherence as our $Z_\odot$, where the sub-solar gas abundances are scaled from this value. Table 2.2 shows how the BPASS stellar metallicities are related with the gas metallicities used in this work (in $Z_\odot$ units). We created our BPASS SFGs models taking into consideration that the metallicity of the gas should not be, in principle, higher than the metallicity of the stellar atmosphere.

Table 2.2: Solar and sub-solar BPASS stellar metallicities. In this work we used BPASS atmospheres with stellar metallicity of 0.014 ($Z_\odot$), 0.006 (0.42 $Z_\odot$), 0.002 (0.14 $Z_\odot$) and 0.001 (0.07 $Z_\odot$).

BPASS stellar metallicity (Z)	0.014	0.010	0.008	0.006	0.004	0.003	0.002	0.001
BPASS stellar metallicity ($Z_\odot$)	1	0.7	0.56	0.42	0.28	0.21	0.14	0.07

Each of the BPASS stellar metallicity files has 42 columns and 100000 rows. The first column is the wavelength of the SED, in Angstroms (starting at 1 Å, spectral resolution of 1 Å), and the next 41 columns have the information of the flux for the population at different ages, from 1 Myr up to 10 Gyr. The age in each column is given by $10^{(6+0.1(n-2))}$ years, $2 \leq n \leq 42$; and the fluxes are in Solar Luminosities per Angstroms for a cluster of 10^6 $M_\odot$.

To avoid creating an extensive grid of models we extracted SED information for 10 different ages, starting in 1 Myr, in steps of 0.4 dex in log units. Note that the ages are given in a logarithmic

scale. This corresponds to extract every 4th column in the file starting in the second column (Table 2.3).

Table 2.3: BPASS stellar ages used in this work

BPASS columns	2	6	10	14	18	22	26	30	34	38
Log (age/yrs)	6.0	6.4	6.8	7.2	7.6	8.0	8.4	8.8	9.2	9.6

Using BPASS on CLOUDY

CLOUDY has various libraries of SEDs that can be used for simulate the incident radiation field and can be included on the simulations in a very straightforward way. However, CLOUDY does not include BPASS SEDs. It was then necessary to create BPASS inputs for CLOUDY, which offers the possibility to include user-defined stellar atmosphere grids. However, the process requires reconstructing the information of the stellar models into one that CLOUDY can read. This involves compiling the BPASS SEDs and is described in detail in Appendix B.

The stellar atmospheres were then entered using the CLOUDY command *table star 'atmosphere.mod' star_age*. This command has various sub-keywords that allow to select which atmosphere CLOUDY should use, interpolating between the atmosphere grid to calculate the SED with the specific given parameters. This command only specifies the continuum shape. It is then necessary to specify a luminosity.

We defined the luminosity in units of Q(H) [s^{-1}], i.e. the total number of ionizing photons emitted by the central object. The calculation of the Q(H) values used to produce the grid is explained in the next section.

BPASS Ionizing Spectrum Intensity

All the SEDs' fluxes are normalized in CLOUDY to the Lyman limit (1 Rydberg). To correct from normalization we calculated the ionization inherent to each model, which is different for each stellar metallicity and for each stellar age.

CLOUDY converts flux density into energy density necessary for the SED. This is done by multiplying the flux density by the wavelength, obtaining $\lambda\, F_\lambda$, i.e. energy per unit area per unit time. In our case CLOUDY will be multiplying luminosity density by the photons, which leads to SEDs in $\lambda\, L_\lambda$, i.e. energy per unit time, in $L_\odot$ units.

Using the relation between flux and luminosity, $L_\lambda = 4\pi d^2 F_\lambda$ and $F_\nu\, d\nu = F_\lambda\, d\lambda$, where $F_\nu = \lambda^2/c\, F_\lambda$, the value of Q(H) (Eq. (2.6)) can be calculated in function of L_λ:

$$Q\,(\mathrm{H}) = \frac{1}{h\,c} \int_{10\text{Å}}^{912\text{Å}} \lambda\, L_\lambda\, d\lambda, \tag{2.7}$$

where the flux of the ionizing photons was calculated using the photons with wavelengths between 10 Å and 912 Å available in the BPASS SEDs. We followed Stanway et al. (2016) who calculated the flux of the ionizing photons using integration limits between 10 Å and 912 Å. The flux is negligible

below 10 Å and we found no substantial changes on the Q(H) calculations using all the ionizing fluxes (i.e. < 912 Å), where it would affect the Q(H) values less than a 0.1%.

We then set a Q(H) = 10^{52} s^{-1} for the most ionizing model ($Z_{BPASS} = 0.001$, Age = 10^6 yrs) and scaled all the Q(H) values according to this reference value (Figure 2.5)

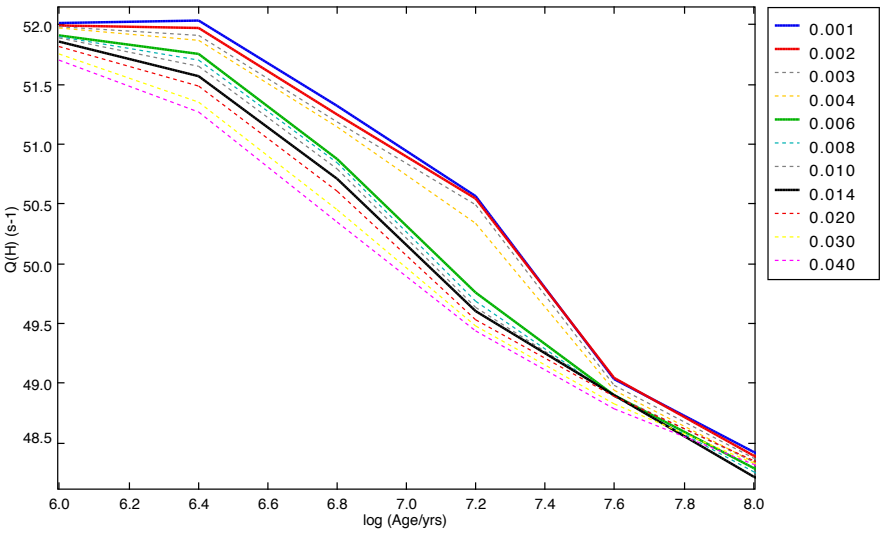

Figure 2.5: Ionizing fluxes (Q(H) values) for a binary stellar population with an ageing instantaneous starburst and with a stellar mass of 10^6 $M_\odot$. The colours indicate the stellar metallicity of each BPASS atmosphere. The solid lines highlight the stellar atmospheres used in this work.

The given BPASS SEDs comprise flux values between $1\text{Å} \leq \lambda \leq 10^6\text{Å}$, i.e. within energies of $911 \times 10^{-5}\,\text{Ryd} \leq h\nu \leq 911$ Ryd. To create a continuum for the full range of energies, CLOUDY couples a black body shape continuum to the BPASS SEDs to produce fluxes for lower energies.

In general, older BPASS models require higher values of Q(H) to produce the same ionization parameter. For that reason, and as natural, our older models will present lower ionization parameters.

Different groups have adopted different approaches to generate different values for the ionization parameter: Byler et al. (2017) chose to fix the inner radius and the density of the cloud and only varied the Q(H) value. Moy et al. (2001) fixed all the three parameters above and varied the filling factor, while Levesque et al. (2010) varied the inner radius of the gas cloud.

As the ionization parameter is sensitive to the geometry of the cloud, as well as the density of the medium and the metallicity of the ionizing source, changing the density and taking into account different metallicities produces a range for the ionization parameter between -1 $\lesssim$ log U_S $\lesssim$ -5 for ages $\lesssim$ 10^7 - 10^8 yrs and lower values of log U_S for higher ages.

2.3.2 Active Galactic Nuclei

The AGNs' SEDs extend from the radio to the gamma rays. The shape of their SED is extremely diverse at radio wavelengths and at higher energies, as described in Section 1.3.4. However, they show a consistent SED shape in the optical-UV range (Shull et al. (2012)). AGNs are characterised by a "big blue bump" (associated with thermal emission from the accretion disc (e.g. Shields (1978)), that starts in the optical and extends into the UV, with a peak in the UV and a decline to higher

energies (e.g. Sanders et al. (1989)). Their shape can be described by a power law or a broken power law (e.g. Osterbrock and Ferland (2006)).

Several efforts have been made to characterise the shape and the peak of the big blue bump, which is of particular importance for the ionizing flux of the AGNs. However, observations on this range of energies are difficult, and the exact position of the big blue bump and its shape is hard to determine (e.g. Shang et al. (2005)), in particular due to the lack of UV observations corrected from the absorption from the IGM. Composite UV AGN spectra using distinct data (e.g. AGNs with different masses, luminosities and viewing angles), show considerable variations on the value of the spectral index of the power law but a steepness towards higher energies (Francis et al. (1991)). We defined the shape of the AGN continuum with a set of power laws $f_\nu \propto \nu^\alpha$ using different spectral indexes (see Table 2.4), where f_ν is the flux in erg cm^{-2} s^{-1} Hz^{-1}.

In CLOUDY it is possible to define a power law radiation field with the *power law* command, which defines the entire radiation field between very low and very high energies. However, this commonly results in some unphysical situations, mainly when extrapolating the radiation field between the optical-ultraviolet region into the radio or gamma-ray energies, which causes several numerical problems (CLOUDY documentation last described in Ferland et al. (2013)). For that reason, we used the *table power law* command, which allows to enter another shape commands, defining that way the entire radiation field from low-energy to high-energy with spectral indexes that have physical meaning.

For lower energies, we used $f_\nu \propto \nu^{5/2}$ and for higher energies $f_\nu \propto \nu^{-2}$, according to Rybicki and Lightman (1979). We then varied the mid-range component from the infrared (0.009115 Ryd, 10 microns) to the X-rays (3676 Ryd, 0.2479 Å) using different values for the power law index (Table 2.4).

Table 2.4: AGN continuum - Power law mid-range energy spectral indexes

Mid-range energy slopes
-1.2, -1.4, -1.6, -1.8, -2.0

The values adopted are commonly used in the literature (e.g. Feltre et al. (2016), Groves et al. (2004)), who also explored values in the range of -2.0 (steepest) $\leq \alpha \leq$ -1.2 (flattest) and which have shown to be consistent with the observations (e.g. Zheng et al. (1997), Lusso et al. (2015)). The continuum was then defined this way between the low-energy limit for the continuum (1.001×10^{-8} Ryd) to its high-energy limit of 7.354×10^6 Ryd.

We also introduce an infrared break at 1 micron to minimize the free-free heating on the infrared which can be considerable for denser clouds. The full radiation field was define with the command *table power law slope x, 1 micron break.*

Chapter 3

Modelling results

3.1 Comparison of the photoionization models

The main features that differentiate our photoionization CLOUDY models are presented in Table 3.1.

Table 3.1: Adjustable parameters for AGNs, SFGs using BPASS atmospheres, and black body photoionization models.

Parameter	AGNs (power law)	SFGs (BPASS)	Black body
Ionizing spectrum	$\alpha = -1.2, -1.4, -1.6, -1.8, -2.0$	Log Age (yrs) = 6.0, 6.4, 6.8, 7.2, 7.6, 8.0, 8.4, 8.8, 9.2, 9.6	T(K) = 20000, 30000, 40000, 50000, 60000, 70000, 80000, 90000, 100000, 110000, 120000, 130000, 140000, 150000
$\log U_0$	$-1.0, -2.0, -3.0, -4.0$	-	$-1.0, -2.0, -3.0, -4.0$
$\log(n_H)(cm^{-3})$	2, 2.7, 3, 3.7, 4, 5	2, 2.7, 3, 3.7, 4, 5	2, 2.7, 3, 3.7, 4, 5
Z_{ISM} ($Z_\odot$)	1, 0.1, 0.01, 0.001, 0.0001, 0.00001	1 , 0.6, 0.4, 0.1, 0.06, 0.04, 0.01, 0.006, 0.004, 0.001, 0.0001, 0.00001	1, 0.1, 0.01, 0.001, 0.0001, 0.00001
Z stellar (Z_{BPASS})	-	0.014, 0.006, 0.002, 0.001	-

In the UV, our high-temperature black body models can produce energies comparable to our AGN models, even though the AGN SEDs keep their ionization to higher energies, producing harder ionizing photons. Overall, our power law models also represent an approximation to an AGN SED. They provide the necessary energy to produce high energy ionization lines, commonly seen in quasars' spectra but do not describe the shape and the energy of the "big blue bump" in a precise way. Our black body models with lower temperatures ($T \lesssim 70000$ K) are also comparable to our BPASS SEDs (the more "realistic" SEDs used in this work). Figure 3.1 exemplify this.

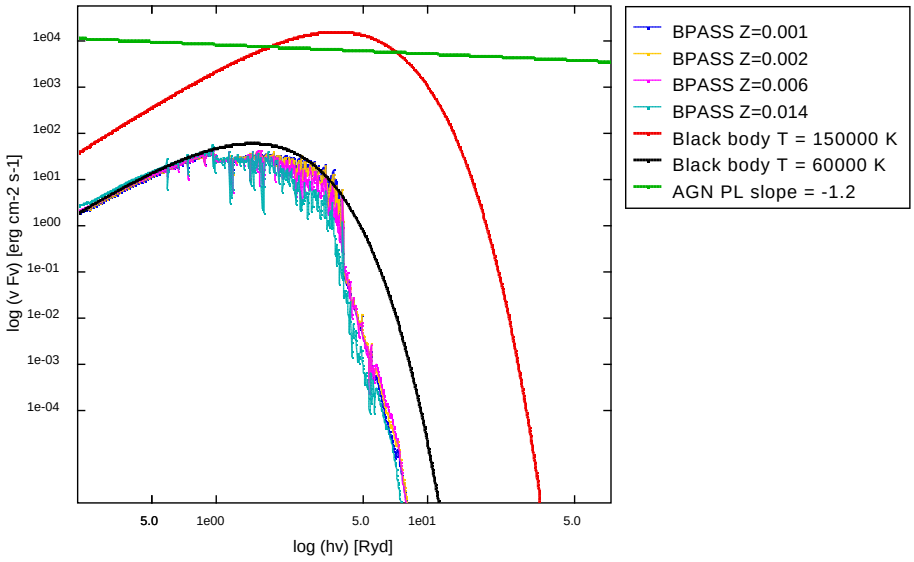

Figure 3.1: Continuum of the models in the UV range of energies (3 - 10^3 eV, 0.22 - 73.5 Ryd). We show the BPASS ESs for the different stellar metallicities used in this work, for an age of 10^6 years. For reference we plot the energy created by an AGN (power law with slope = -1.2), and a black body with 150000 K, both with high density (10^5 cm^{-3}) and high ionization parameter (log U_S = -1). At younger ages, the BPASS SEDs can be compared to a black body with temperature $\sim$ 60000 K - 70000 K with lower densities ($n_H \sim$ 100 - 500 cm^{-3}). Here plotted is a black body with T = 60000 K and n_H = 500 cm^{-3}.

The metallicity of the stellar population influence the BPASS SEDs. The effect is not so evident in Figure 3.1, however binary effects are more accentuated at lower metallicities, which can be seen in Figure 3.2 where we plot a BPASS atmosphere with the same age but different stellar metallicities: Z_{BPASS} = 0.014 ($Z_\odot$) and Z_{BPASS} = 0.001 (0.07 $Z_\odot$).

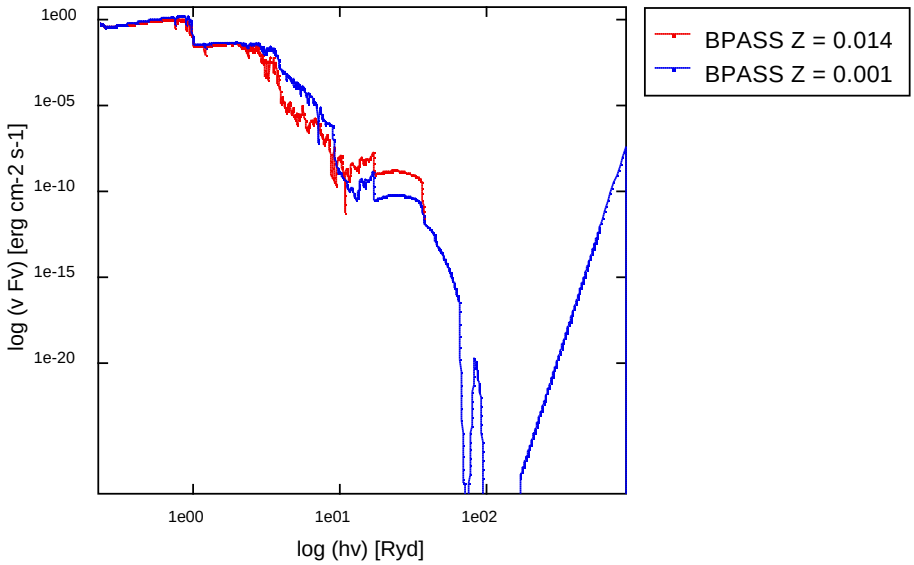

Figure 3.2: BPASS continuum for different stellar metallicities, for an age of $10^{7.2}$ years, plotted in the UV into the X-rays range of energies (3 $\sim$ 10^4 eV, 0.22 - 890 Ryd). The binary and rotational effects are more accentuated at lower metallicities, where they can extend the stellar emission to X-rays energies.

The effect of the BPASS stellar age is more evident in the UV range where, as expected, "older" models show weaker ionizing continuum (Figure 3.3). The effect will be visible on the line-ratios presented on Section 3.2. Older stellar populations originate CLOUDY models with extremely low ionization parameters and therefore very low emission line fluxes.

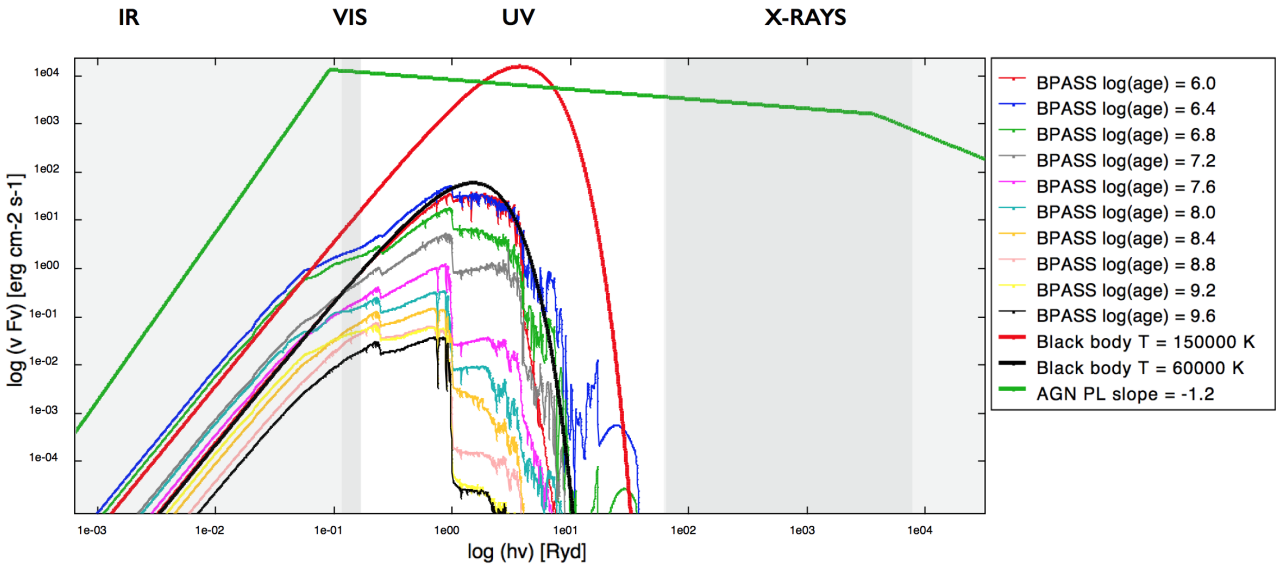

Figure 3.3: Continuum of the models where the UV range of energies (3 - 10^3 eV, 0.22 - 73.5 Ryd) is the white central area of the figure. BPASS evolutionary synthesis for different ages at a stellar metallicity Z = 0.001. For reference we plot the energy created by the same AGN power law model and black body model described in Figure 3.1.

3.2 Modelling diagnosis

As presented in Section 1.4.1, line-ratios are widely used to interpret observations and several line-ratios exist to discriminate between SFGs and AGNs. We explore the "traditional" BPT diagram, which uses optical emission lines; and UV emission-line ratios, using metal UV lines often detected in high-redshift galaxies such as OIII]$\lambda\lambda$1661,1666, CIII]$\lambda\lambda$1907, 1910 and CIV$\lambda\lambda$1548,1551, where we combine line ratios close in wavelength to minimize the influence of dust effects as Feltre et al. (2016). We also use HeIIλ1640 recombination line which is commonly seen in very hot stars (O and B stars). Its identification in a galaxy spectrum should indicate a very young stellar population. Galaxies that hold mainly POP III stars should have harder spectra and emit more HeII photons, and it is expected that HeII can help identifying early SFGs. We present the BPT diagram log([OIII]λ5007/Hβ) vs log([NII]λ6584/Hα), usually used to distinguish nearby objects (Figure 3.4).

3.2.1 BPT diagram

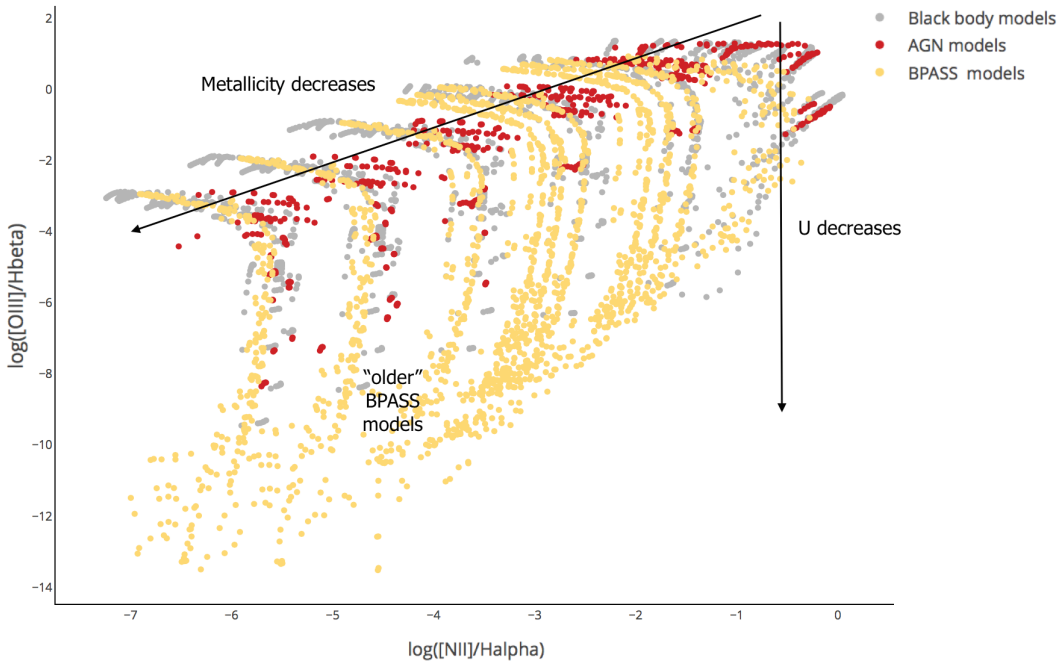

Figure 3.4: BPT diagram spanning the full range of parameters listed in Table 3.1 for all the computed models. The region occupied by BPASS models with older ages is indicated in the figure, as well as the general trend for the metallicity and the ionization parameter.

Our BPASS models extend on the diagram to lower values, mainly because of higher stellar ages. For older BPASS models (age $\gtrsim 10^{7.6} - 10^{8}$ yrs), the emission lines are weak as they are very low ionizing sources (-10 $\lesssim$ log U_S $\lesssim$ -5). Our black body models do not reach such lower values (log U_S $\gtrsim$ -4.5). The metallicity decreases for all the models as indicated in the figure, reaching low [NII]λ6584/Hα ratios not commonly seen in the BPT diagram (due to the extremely low metallicities used to create the models). It is important to note that the parameters used to create our models are not typically observed in nearby galaxies. Low metallicity values, such as $10^{-3} - 10^{-5}\,Z_{\odot}$ were

never detected, and high densities such as 10^5 cm^{-3} are also not probable in these systems, where typically gas densities in narrow-line regions of AGNs have $n_H \sim 10^3$ cm^{-3} and SFGs $n_H \sim 10^2$ cm^{-3} (Osterbrock and Ferland (2006)). As the metallicity decreases both SFGs and AGNs start occupying different regions on the BPT diagram, where AGNs with a metallicity below the solar metallicity are shifted to the "SFGs region" defined by the Kauffmann et al. (2003) and Kewley et al. (2013) divisions, which has been noted also by others (e.g. Groves et al. (2006)).

All of our AGN models above both the Kauffmann et al. (2003) and Kewley et al. (2013) divisions have solar metallicity and our BPASS SFGs models do not exceed the SFG - AGN division (see Figure 3.5). SFGs models with a metallicity above the solar (which we have not modelled) would have been "shifted" towards the "AGN solar metallicity region". We note that the BPASS models that fall into the composite area correspond to stellar populations with young ages at solar or near sub-solar metallicities and low gas densities. Here, the AGNs behaviour can be described by our black body models with solar metallicity, with either extremely high temperatures and lower densities ($\sim 10^2$ - 10^3 cm^{-3}) or very high densities ($\sim 10^5$ cm^{-3}) but lower temperatures (yet $\gtrsim$ 70000 K).

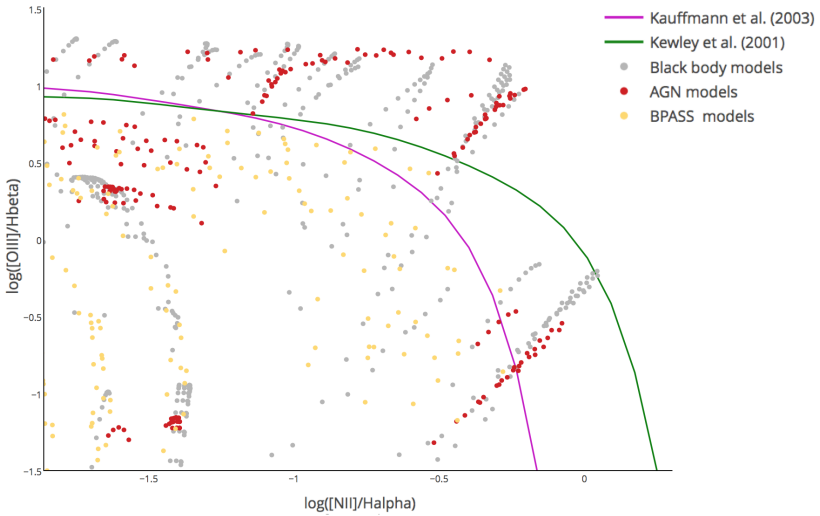

Figure 3.5: BPT diagram for near solar metallicity models. Galaxies above the Kauffmann et al. (2003) empirical division or theoretical Kewley et al. (2013) division should be considered AGNs. The area in-between is the composite region, where an object falling into this area can be either an AGN or a SFG.

The BPT diagram does not allow to distinguish a SFG with solar metallicity from an AGN with metallicity below $Z_\odot$, and its interpretation to study high-redshift objects should be used with careful (e.g. Groves et al. (2006)). At solar metallicity, our models are consistent with the BPT diagram and can successfully identify the nature of nearby objects, which suggests that our models can be used to explore UV emission lines diagnostic ratios.

We note that in Feltre et al. (2016)'s models (used to distinguish SFGs from AGNs), SFGs overlap the AGN region on the BPT diagram. The models that fall into the AGN region are models with high ionization parameter ($\log U_S \gtrsim -2$) and metallicity $\gtrsim 0.5\ Z_\odot$ We note, for example, that on our BPASS models a galaxy with solar metallicity (both stellar and ISM) and a stellar population of $10^{6.8}$ years can reach $\log U_S \sim -2$ and still being consistent with the BPT diagram.

3.2.2 UV emission-line diagnostic ratios

Besides HeIIλ1640, the doublets of carbon CIII]$\lambda\lambda$1907,1910, CIV$\lambda\lambda$1548,1551 and oxygen OIII]$\lambda\lambda$1661,1666 are the most commonly detected UV metal lines in high-redshift galaxies. In all of our models we present the total emission of the doublet: CIII]$\lambda\lambda$1907,1910 (CIII]λ1909), CIV$\lambda\lambda$1548,1551 (CIVλ1549) and OIII]$\lambda\lambda$1661,1666 (OIII]λ1665).

HeIIλ1640 can be combined with CIVλ1549 or other collisionally excited line such as OIII]λ1665 and CIII]λ1909 and was used by Feltre et al. (2016) to successfully distinguish between photoionization from SFGs and AGNs. CIVλ1549/HeIIλ1640 and CIII]λ1909/HeIIλ1640 are sensitive to the metallicity and CIII]λ1909/CIVλ1549 to the ionization parameter and the combination of both line ratios can provide a good diagnosis of the source (Groves et al. (2004)). In general ratios of carbon and oxygen lines to HeII tend to give a good indication to the metallicity as well as the density. The effect of rising the density at other fixed parameters, increases CIII]/HeII, CIV/HeII and OIII]/HeII as exemplified in Figure 3.6 (right), using the CIII] emission line as a reference. Raising the density increases the probability that de-excitation of an excited atom happen through collisions. This raises the cooling radiative efficiency through UV lines rather than other lower energy lines. As a result these line-ratios increase.

The effect of increasing the metallicity at other fixed parameters, increases also metal to helium line-ratios to a maximum, where above that plateau they start to decrease to higher metallicities. As the metallicity increases, cooling through UV collisionally excited transitions raises. However, when the electronic temperature for cooling through other lower energy lines is reached, they start to dominate. As a result these metal line-ratios drop. These effects can be seen in Figure 3.6 (left).

As expected, the temperature and the ionization parameter in our black body models, also has influence on metal to helium line-ratios. Raising the temperature, as well as raising the ionization parameter increases the flux of emission lines with higher ionization potential (see Table 2.1), which makes the ratios CIV/HeII, CIII]/HeII and OIII]/HeII to increase.

The ratio of CIV/CIII] also increases with the ionization parameter since CIV has higher ionization potential than CIII].

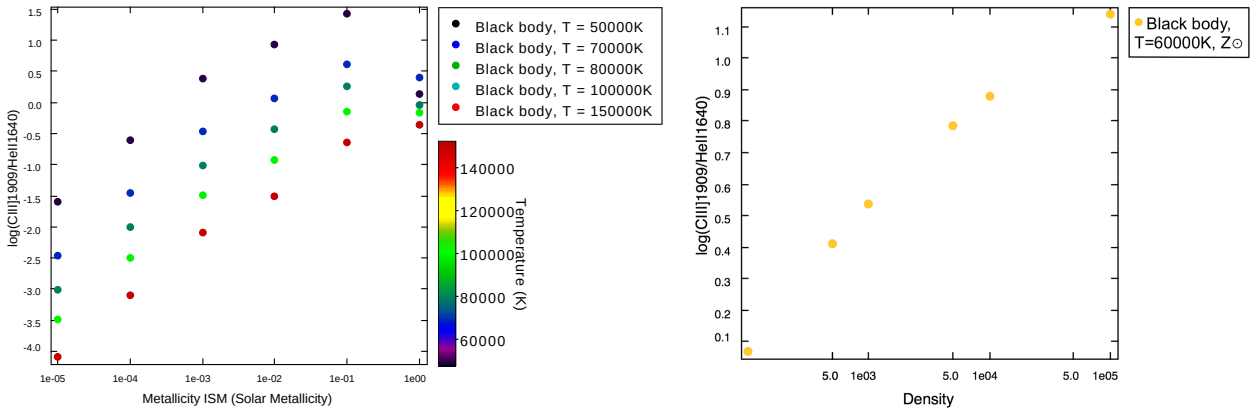

Figure 3.6: Influence of density (right), temperature and metallicity (left) on CIII]λ1909/HeIIλ1640, as an illustration. The same effects can be seen in other metal to HeII line-ratios, such as CIVλ1549 and OIII]λ1665.

We examine carbon and oxygen emission line-ratios proposed by Feltre et al. (2016) to discriminate AGNs and SFGs. These include a combination of HeII with CIII], CIV and OIII] emission lines.

As an example we present the diagram CIII]λ1909/HeIIλ1640 vs CIVλ1549/HeIIλ1640 ratio (Figure 3.7), which was proposed by Feltre et al. (2016) as a good diagnosis diagram using just three emission lines. The other emission-line diagrams used in this work, which include combinations of both carbon and oxygen emission lines, are shown on Appendix C.

We point the general trend for the ionization parameter and for the metallicity. However, note the metallicity effects explained in Figure 3.6, left. For example, at $Z_\odot$ CIII]/HeII is smaller that at 0.1 $Z_\odot$, so there is a turnover in the plots around that metallicity, where usually CIII]/HeII ratio reaches its higher value and then decreases to higher metallicities.

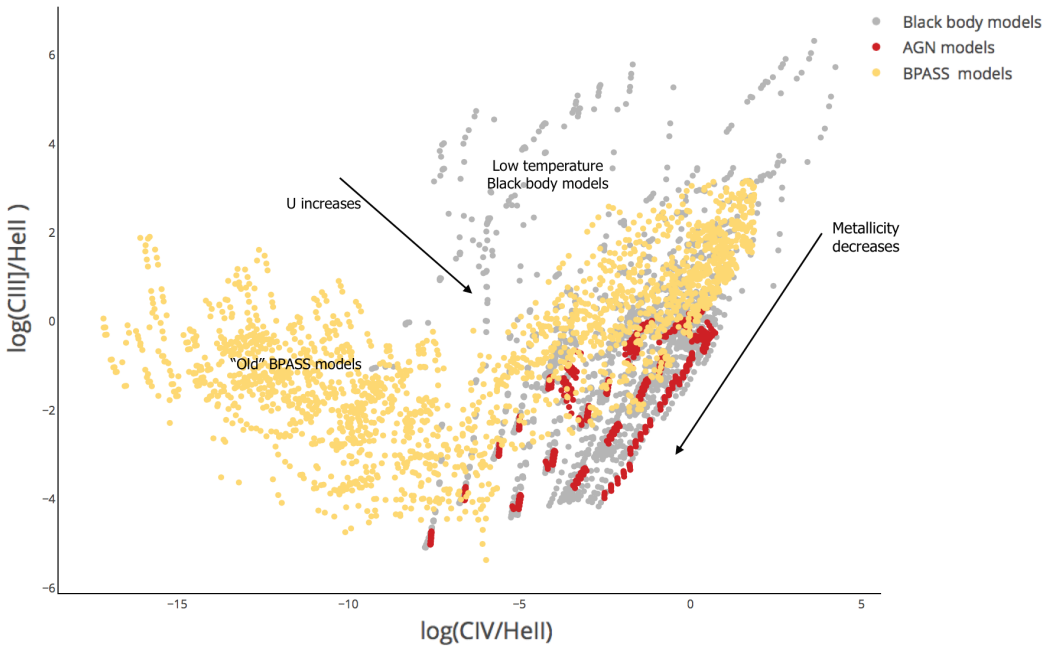

Figure 3.7: Log(CIII]λ1909/HeIIλ1640) vs log(CIVλ1549/HeIIλ1640) diagram spanning the full range of parameters listed in Table 3.1.

As in Figure 3.4 we indicate our BPASS models with older ages which correspond to very low ionizing sources. It is also possible to see that SFGs and AGNs overlap. Our black body models reach values obtained with both BPASS models and power law models. We analyse the "AGN-SFG discriminator region" (excluding older BPASS models) which corresponds roughly to make a zoom in into models with log $U_S \geq$ -4, i.e. BPASS models with ionization parameter similar to our AGN models (-4 $\leq$ log $U_S \leq$ -1). Our BPASS models that overlap the AGN models have extremely low gas metallicity $Z_{ISM} \lesssim 0.001$ $Z_\odot$, young stellar population ($\sim 10^6 - 10^7$ yrs) and different combinations of Z_{BPASS} and densities (see Figure 3.8). As the ionization increases, black body models with higher temperatures, low density or low metallicity fall into the AGN area.

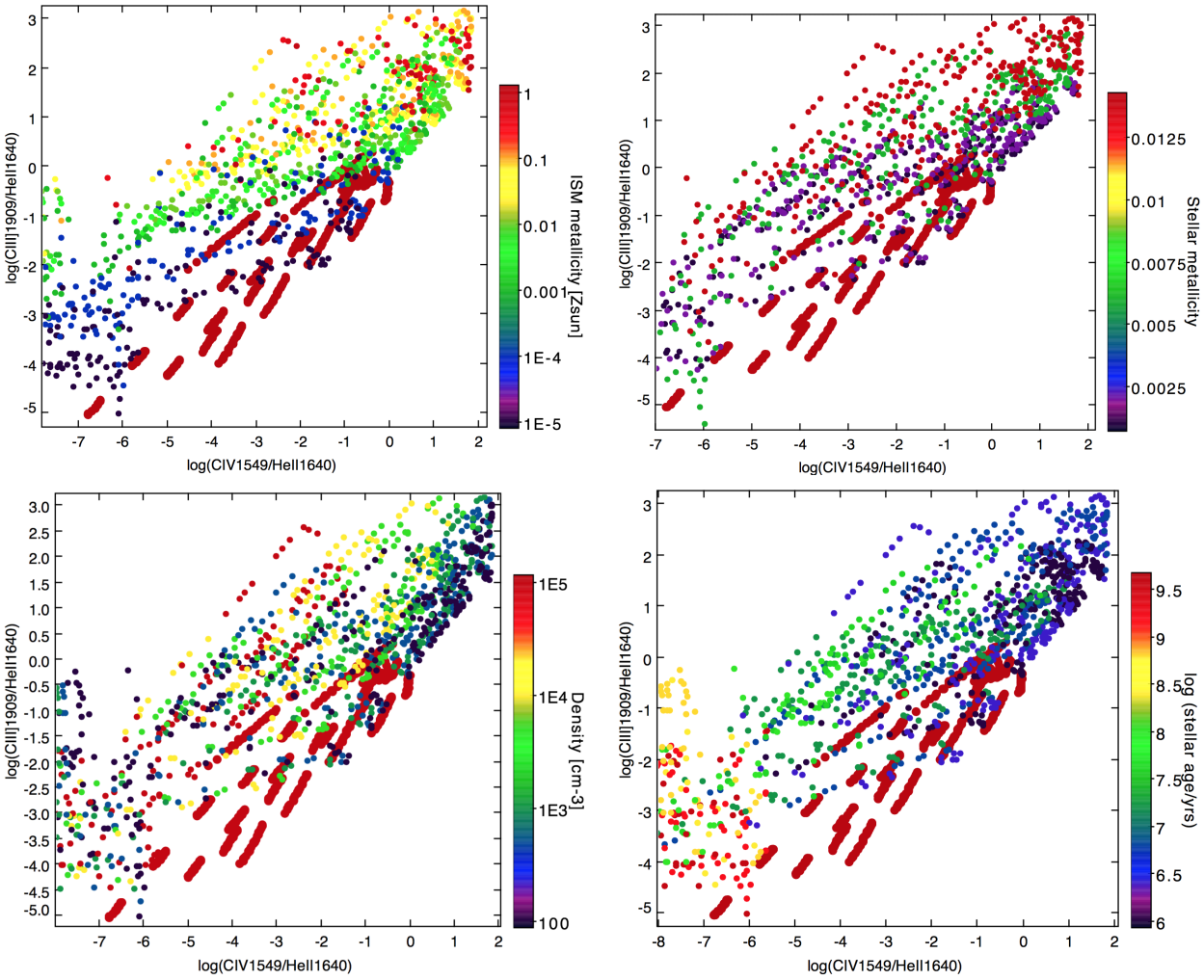

Figure 3.8: Diagram region where AGN and BPASS models overlap. The red big dots correspond to AGN models for the full range of parameters listed in Table 3.1, and the coloured dots to different characteristics of our BPASS models.

This diagram was indicated by Feltre et al. (2016) as a good AGN-SFG discriminator. According to our models, BPASS SFGs with $Z_{ISM} \gtrsim 0.01\ Z_\odot$ do not overlap the AGN area and our AGN models can be well explained by our black body models with $T \gtrsim 80000$ K (Figure 3.9). The same effect can be seen in the other computed UV line-ratios (see Appendix C).

Our black body models that fall into the BPASS region (on Figure 3.9) have a wide variety of properties, with a combination of different gas densities ($10^2 - 10^5\,cm^{-3}$). They can be qualitatively described by black bodies with extremely low gas metallicity ($\sim 10^{-5} Z_\odot$) and low temperature ($\sim$ 20000 − 30000K), very low gas metallicity ($\sim 10^{-4} - 10^{-3} Z_\odot$) and temperature ($\sim$ 30000 − 40000K), low gas metallicity ($\sim 10^{-2} Z_\odot$) and temperature ($\sim$ 30000 − 50000K). For higher metallicities they span from $\sim$ 40000 − 70000K ($\sim 10^{-1}\,Z_\odot$) and $\sim$ 40000 − 90000K ($Z_\odot$). They also reach temperatures $\sim$ 80000 − 90000K up to 150000K closer to our "AGN models zone" with a $Z_{ISM} = Z_\odot$ which means they describe better an AGN than a SFG behaviour.

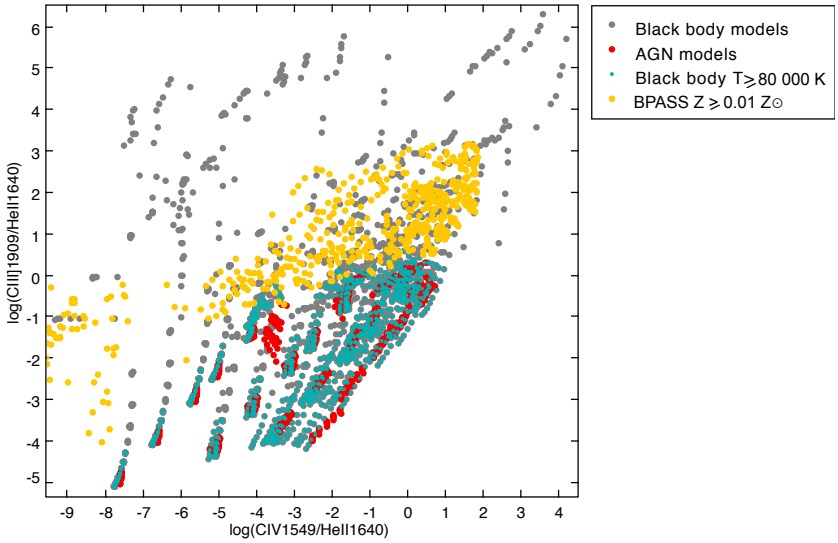

Figure 3.9: "AGN-SFG discriminator region". We plot our black body and AGN models for the full range of parameters (Table 3.1) and our BPASS galaxies with $Z_{ISM} \gtrsim 0.01\ Z_{\odot}$, which can be distinguished from AGNs. Our AGN models can be approximated to black bodies with $T \gtrsim 80000$K.

In Chapter 4 we use our UV diagnostic line ratios to study the nature of several line emitters across redshift. In Sobral et al. (in prep) we compared our line-ratio diagrams with Feltre et al. (2016) and use them to interpret the nature of 6 Lyα emitters found at $z \sim 2$ - 3. These results are presented in Section 4.2.

Chapter 4

Application across redshift

4.1 Analogues of primeval galaxies at $2.4 \leq z \leq 3.5$

Amorín et al. (2017) studied a faint population of 10 SFGs from the COSMOS field, selected on the UV by their colours, using the VLT-VIMOS Ultra Deep Survey (VUDS). VUDS is a deep spectroscopic survey with $\sim$ 10000 galaxies. They extracted a sample of 1870 galaxies with $2.4 \leq z \leq 3.5$ and selected galaxies with simultaneous detections of UV emission lines with high S/N and reliable spectroscopic redshift. They first excluded all the candidates identified as AGNs in X-ray surveys and then compared them with the UV emission line diagnostics from Feltre et al. (2016) and Gutkin et al. (2016). In all the galaxies CIII]$\lambda\lambda$1907,1910 and OIII]$\lambda\lambda$1661,1666 were detected with S/N $>$ 3, and 8 of the 10 galaxies presented also S/N $>$ 3 in CIV$\lambda\lambda$1548,1551. Their UV emission line fluxes, along with the calculated properties of these galaxies, are presented in Appendix D. The presence of high equivalent widths of other UV nebular emission rather than Lyα suggests hard radiation fields from young massive stars. The composite spectrum of the 10 SFGs is presented in Figure 4.1.

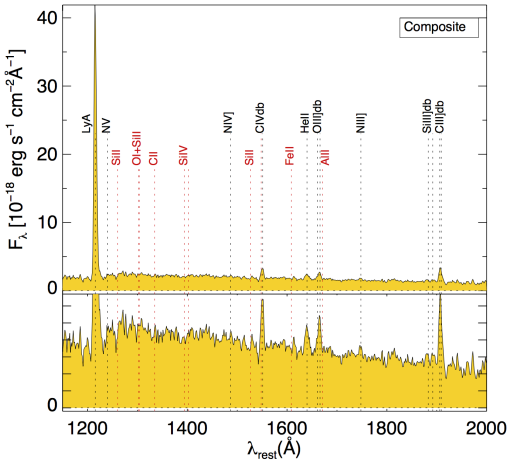

Figure 4.1: Amorín et al. (2017) composite spectrum produced through stacking of the 10 individual SFGs. The relevant emission lines are labeled in black. Note that the doublets of carbon and oxygen are unresolved due to the low spectral resolution. Absorption lines are label in red.

They estimated physical properties such as star formation rate, stellar mass and stellar ages by SED fitting with a set of Bruzual and Charlot (2003) ES models with four different metallicities (0.02 $Z_\odot$, 0.2 $Z_\odot$, 0.4 $Z_\odot$ and $Z_\odot$) adopting a Chabrier (2003) IMF. Nebular emission was included following Schaerer and de Barros (2009) with an electron density of 100 cm^{-3} and temperature of 10^4K. They concluded that these galaxies have low mass, high star formation rate and are very compact systems. They used a grid of CLOUDY photoionization models from HII-CHI-MISTRY (Pérez-Montero (2014)) on the 3MdB (Morisset et al. (2015)) which uses POPSTAR ES models (Mollá et al. (2009)), using a routine from Pérez-Montero and Amorín (2017) which obtains O/H, C/O and log U comparing the relative fluxes of the UV emission lines.

Overall, they extracted $\sim$ 4000 models under the conditions: oxygen abundances in the range [7.1, 9.1], log U in the range [-4.0, -1.5] and a constant log(C/N) = 0.6. They analysed line-ratios using CIII]λ1909; OIII]λ1665; HeIIλ1640 and CIVλ1549 and estimated that these galaxies have metallicities $\sim 0.1 - 0.05$ $Z_\odot$, strong ionization parameters log U $\sim$ -2 and log(C/O)$\sim$ -0.7.

We used our models to investigate the nature and the properties of these galaxies using the UV emission line ratios presented in Section 3.2.2. We computed different combinations of the CIII]λ1909, OIII]λ1665, HeIIλ1640 and CIVλ1549 emission lines, which can be seen in Figure 4.2.

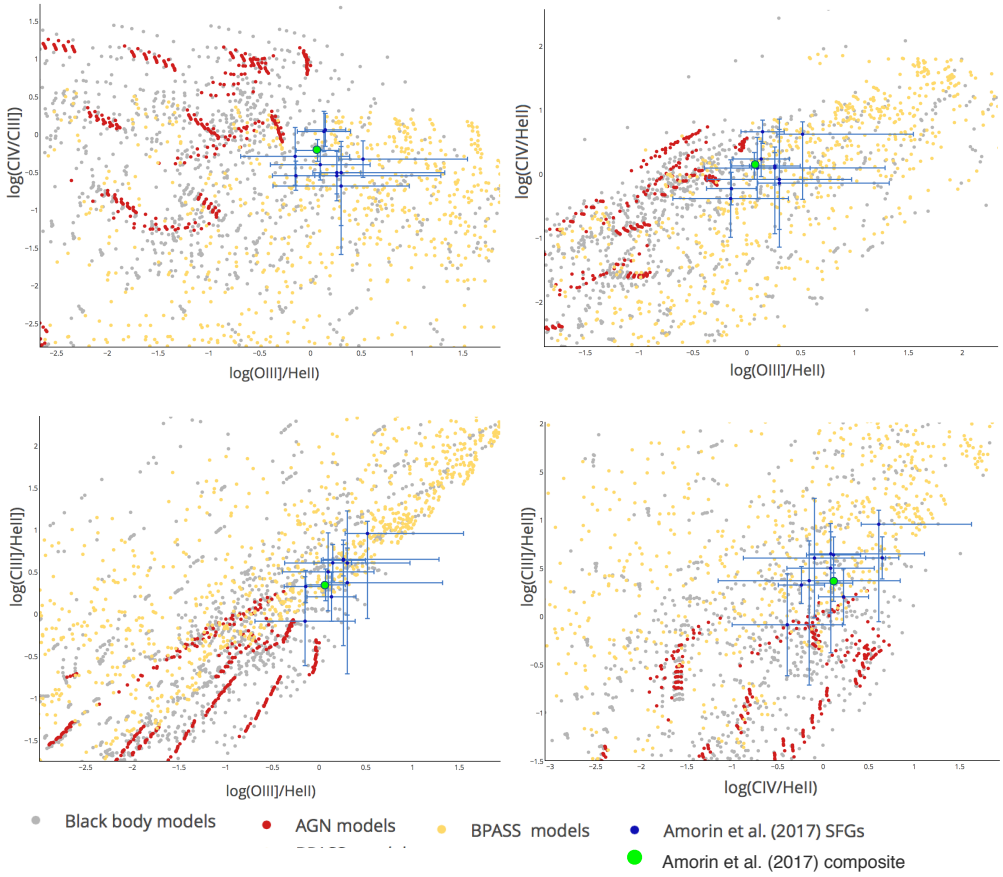

Figure 4.2: Computed UV emission line ratios diagrams for the 10 SFGs (and the composite value of the sample) from Amorín et al. (2017). Here we show the region of our diagrams (presented in Section 3.2.2 and in Appendix C) occupied by these galaxies. The great error bars were computed from non-detections in HeII in two sources and non-detections in HeII and CIV in one source (see Table D), computed from 1 σ uncertainties.

The galaxies and the composite value for the sample fall into an area essentially populated by our BPASS SFGs models. High values of CIV/CIII] indicates high ionization sources.

For each galaxy we calculated the mean value of our BPASS and black body models taking in consideration the errors in the measurements. We combined the results obtained with the four emission line diagrams (on Figure 4.2) and present the estimated physical properties using our black body and BPASS models in Tables 4.1 and 4.2, respectively. All the results are the mean values obtained with the different diagrams.

Table 4.1: Calculated properties using our black body models for the 10 SFGs and composite spectrum from Amorín et al. (2017).

VUDS ID	log U	Temperature (K)	Density (cm^{-3})	Z_{ISM} ($Z_\odot$)	log(C/O)	log(O/H)+12
510583858	-2.02 ± 0.05	86983 ± 6724	17845 ± 3806	0.35 ± 0.05	-0.66 ± 0.03	7.48 ± 0.05
510838687	-1.92 ± 0.16	64602 ± 6033	25007 ± 2631	0.30 ± 0.05	-0.66 ± 0.02	7.30 ± 0.13
511267982	-1.20 ± 0.11	73796 ± 4810	21004 ± 2207	0.36 ± 0.06	-0.63 ± 0.02	7.41 ± 0.13
5100534435	-2.00 ± 0.05	78635 ± 3831	21165 ± 1955	0.34 ± 0.05	-0.65 ± 0.02	7.40 ± 0.09
5100565880	-1.73 ± 0.33	65028 ± 9109	33961 ± 9313	0.24 ± 0.08	-0.67 ± 0.04	7.19 ± 0.30
5100750978	-2.02 ± 0.07	65991 ± 7059	21863 ± 2063	0.31 ± 0.11	-0.64 ± 0.04	7.25 ± 0.22
5100994378	-2.17 ± 0.14	67232 ± 3816	16147 ± 4280	0.35 ± 0.13	-0.61 ± 0.03	7.22 ± 0.38
5100998761	-1.95 ± 0.11	70428 ± 5668	23593 ± 1966	0.28 ± 0.07	-0.67 ± 0.02	7.30 ± 0.16
5101421970	-1.81 ± 0.06	78716 ± 9641	24757 ± 7498	0.24 ± 0.17	-0.71 ± 0.08	7.42 ± 0.30
5101444192	-1.94 ± 0.09	61458 ± 1238	22802 ± 9250	0.24 ± 0.06	-0.68 ± 0.04	7.25 ± 0.09
Composite	-1.91 ± 0.10	71108 ± 4097	24916 ± 7170	0.22 ± 0.12	-0.68 ± 0.05	7.18 ± 0.25

The values obtained with our black body models are very similar to the values obtained by Amorín et al. (2017), where we can compare values for the ionization parameter, carbon to oxygen abundance, and metallicity in log(O/H)+12 (see Figure 4.3).

For all sample our black body models predict similar values for the ionization parameter, log(C/O) and metallicity (see Appendix D), where Amorín et al. (2017)'s composite values are: log U = -1.90 ± 0.27, log(C/O) = -0.69 ± 0.08 and the metallicity log(O/H)+12 = 7.54 ± 0.25 (corresponding to variations in the sample between $\sim$ 0.05 Z$\odot$ and $\sim$ 0.1 Z$\odot$). Comparing with our results, these last two parameters present small discrepancies, mainly because of our definition of log(C/O), and the interval range of metallicities used to compute our black body models.

We used a log(C/O) function across different metallicities, while Amorín et al. (2017) variates log(C/O) according to a fixed log(N/O) using four different metallicities between $Z_\odot$ and 0.02 $Z_\odot$. Amorín et al. (2017)'s galaxies present log(C/O) values ranging from -1 to -0.38 which is supported by Berg et al. (2016) who studied a sample of galaxies spanning from $7.2 \leq$ log(O/H)+12 ≤ 8.2 that show variations of C/O values between this range of metallicities. The flat trend at these metallicities is discussed by many with some potential scenarios and a lack of observations to determine the C/O trend and its dispersion (see Section 2.1.3).

Regarding to the metallicity we obtained values slightly lower than Amorín et al. (2017) but within the same range of log(O/H)+12 ($\sim 0.03 - 0.06$ $Z_\odot$). While Amorín et al. (2017) used four values of metallicity between $Z_\odot$ and 0.02 $Z_\odot$ we used only three with our black body models that extend to lower metallicities ($Z_\odot$, 0.1 $Z_\odot$ and 0.01 $Z_\odot$). Therefore, contributions from metal poor models generates lower results. It is expected that the fine grid of our BPASS models, where we

computed seven values of metallicity within the $Z_\odot - 0.01\ Z_\odot$ range, give a more precise result due to the more realistic used SED.

Overall, the models which Amorín et al. (2017) used to calculate the properties of these galaxies can be reproduced by our black body models with higher ionization parameters. Their photoionization models are based on the POPSTAR ESs from Mollá et al. (2009) of a single instantaneous burst with an age of 1Myr which do not include binary and rotation effects. For this reason, lines associated with species having high ionization potentials can just be produced by models with high ionization parameters.

The temperature also has a high effect on the production of these UV lines. For example within this range of ionization energies a difference in 10000K can approximately triple the number of photons capable of ionizing species like OIII] or CIII] (see Steidel et al. (2014), Figure 19). Note that the temperature estimated with our models is the mean of several models and is biased to higher temperatures, due to the range of temperatures used to create the models (which can reach 150000K). A more representative value can be obtained by the median and mode values for the sample which correspond to temperatures ranging from $50000 - 70000$K. However, even with high temperatures, our black body models need higher ionization parameters to create such emission line intensities. This means that single stellar evolutionary synthesis codes do not have the necessary ionization to explain these emission lines (see e.g. Steidel et al. (2014)), and also means they are quite similar to a black body shape.

Lastly, it is important to note that the presented mean density does not have a physical meaning since models with both low and high densities ($10^2 - 10^5$ cm^{-3}) contribute for the final result. The median value of the density for each galaxy correspond to densities of $1000 - 5000$ cm^{-3}.

For metallicities described in terms of $Z_\odot$ our models are again biased to higher values. Within this zone of the diagram our black body models with $Z_\odot$ but extremely high temperatures and/or high ionization parameters can reach these values. The median and mode values for all the galaxies is 0.1 $Z_\odot$, which is in much agreement with Amorín et al. (2017) results and closer to the results obtained in terms of log(O/H)+12.

We performed the same approach using our BPASS models and present our results in Table 4.2.

Table 4.2: Calculated properties using BPASS models for the 10 SFGs and composite spectrum from Amorín et al. (2017).

VUDS ID	$Z_{STELLAR}$	log(age/yrs)	log U	Density(cm^{-3})	Z_{ISM} ($Z_\odot$)	log(C/O)	log(O/H)+12
510583858	0.0038 ± 3.61E-4	6.60 ± 0.06	-2.63 ± 0.16	24721 ± 1358	0.031 ± 0.019	-0.62 ± 0.04	6.03 ± 0.17
510838687	0.0049 ± 2.77E-4	6.45 ± 0.04	-2.25 ± 0.15	3486 ± 2640	0.087 ± 0.012	-0.73 ± 0.01	6.81 ± 0.04
511267982	0.0047 ± 2.29E-4	6.51 ± 0.03	-2.39 ± 0.12	3681 ± 2721	0.070 ± 0.019	-0.70 ± 0.01	6.60 ± 0.06
5100534435	0.0047 ± 4.60E-4	6.55 ± 0.05	-2.48 ± 0.13	3887 ± 2488	0.069 ± 0.023	-0.70 ± 0.02	6.58 ± 0.09
5100565880	0.0026 ± 8.15E-4	6.38 ± 0.16	-2.07 ± 0.31	941 ± 878	0.053 ± 0.048	-0.63 ± 0.05	6.30 ± 0.11
5100750978	0.0044 ± 3.53E-4	6.59 ± 0.02	-2.47 ± 0.06	3530 ± 1866	0.060 ± 0.022	-0.71 ± 0.01	6.59 ± 0.10
5100994378	0.0037 ± 1.50E-4	6.63 ± 0.11	-2.58 ± 0.17	2466 ± 292	0.007 ± 0.004	-0.68 ± 0.02	6.16 ± 0.11
5100998761	0.0035 ± 4.91E-4	6.60 ± 0.01	-2.41 ± 0.11	2643 ± 1724	0.035 ± 0.021	-0.69 ± 0.01	6.36 ± 0.04
5101421970	0.0024 ± 6.80E-4	6.56 ± 0.14	-2.07 ± 0.14	691 ± 227	0.023 ± 0.031	-0.68 ± 0.06	6.24 ± 0.20
5101444192	0.0035 ± 8.20E-4	6.64 ± 0.06	-2.32 ± 0.03	1979 ± 551	0.056 ± 0.045	-0.71 ± 0.02	6.53 ± 0.08
Composite	0.0030 ± 9.12E-4	6.63 ± 0.12	-2.21 ± 0.26	992 ± 465	0.061 ± 0.055	-0.67 ± 0.06	6.35 ± 0.19

The results obtained with our BPASS models reveal different characteristics: these galaxies do not need such higher ionization parameters (log U $\sim$ -2.1 $-$ -2.6) to reach the same ionization energies and they can be explained by young stellar populations ($\sim 10^{6.4} - 10^{6.6}$ yrs) surrounded by an very low metallicity environment (log(O/H)+12 $\sim$ 6.0 $-$ 6.6, 0.002 $-$ 0.008 $Z_{\odot}$).

Both the stellar metallicity, density and gas metallicity in terms of $Z_{\odot}$ (Z_{ISM}) presented on Table 4.2 are biased to higher values while the upper limit of the stellar age to lower values, as we explain next.

The density values are much more constrained than in the case of our black body models (see Figure 3.8, bottom left) with main contributions from low density models. However, the density values on the table are not accurate. Both the median and mode values of the sample used to estimate this parameter fall into values $100 - 500$ cm^{-3}, which is in much more agreement with the expected values for these systems ($\sim 10^2$ cm^{-3}, e.g. Osterbrock and Ferland (2006)).

The stellar metallicity is also biased to higher values mainly because of higher metallicity values of 0.014 ($Z_{\odot}$). The main contributions came from models with lower stellar metallicities of 0.001 (0.07 $Z_{\odot}$) and 0.002 (0.14 $Z_{\odot}$). Note that the presented variations result from the different emission line diagrams used and not from the models itself. The standard deviation for the sample is much higher, closer to the obtained values, therefore the mode and the median values described before should be a more representative value for these galaxies.

The gas metallicity presented on the table shows higher metallicities than the median and mode value for each galaxy, mainly because of contributions from $Z_{\odot}$ models. The median and mode values correspond to values of $0.004 - 0.006$ $Z_{\odot}$ which is in much more agreement with the metallicity values obtained in log(O/H)+12.

In Figure 4.3 we make a comparison of the results obtained with the different models. While with our black body models we obtained values similar to Amorín et al. (2017) for the ionization parameter and for the log(O/H)+12 value, with our BPASS models we obtained values approximately an order of magnitude below.

As expected from the BPASS SEDS, lower metallicity systems produce higher ionization photons. These sources do not need such higher ionization parameters since they have already harder ionizing SEDs.

The ionization of the binary BPASS SEDs starts to differ from the single stellar population at log(age/yrs) $\sim$ 6.5, where it steeps abruptly for an ageing instantaneous starburst (see Stanway et al. (2016), Figure 5), in particular for lower metallicities.

The obtained mean result of the stellar age is a contribution from both younger and older models, which include models with ages between 6.0 $\leq$ log(age/yrs) $\leq$ 7.6 (see Figure 3.8, bottom right). However, a higher number of models with log(age/yrs) $\sim$ 6.4 - 6.8 is decisive for the final result. At these ages the BPASS SEDs have harder spectra (see Figure 3.3). This effect is accentuated by a decrease in the stellar metallicity.

Massive stars live longer due to binary effects. At older ages they continue to dominate the spectra. In this way binary interactions increase the period where which the starburst generates ionizing flux, which can reach production rates $\sim$ 100 times higher than single stellar populations (Stanway (2017)).

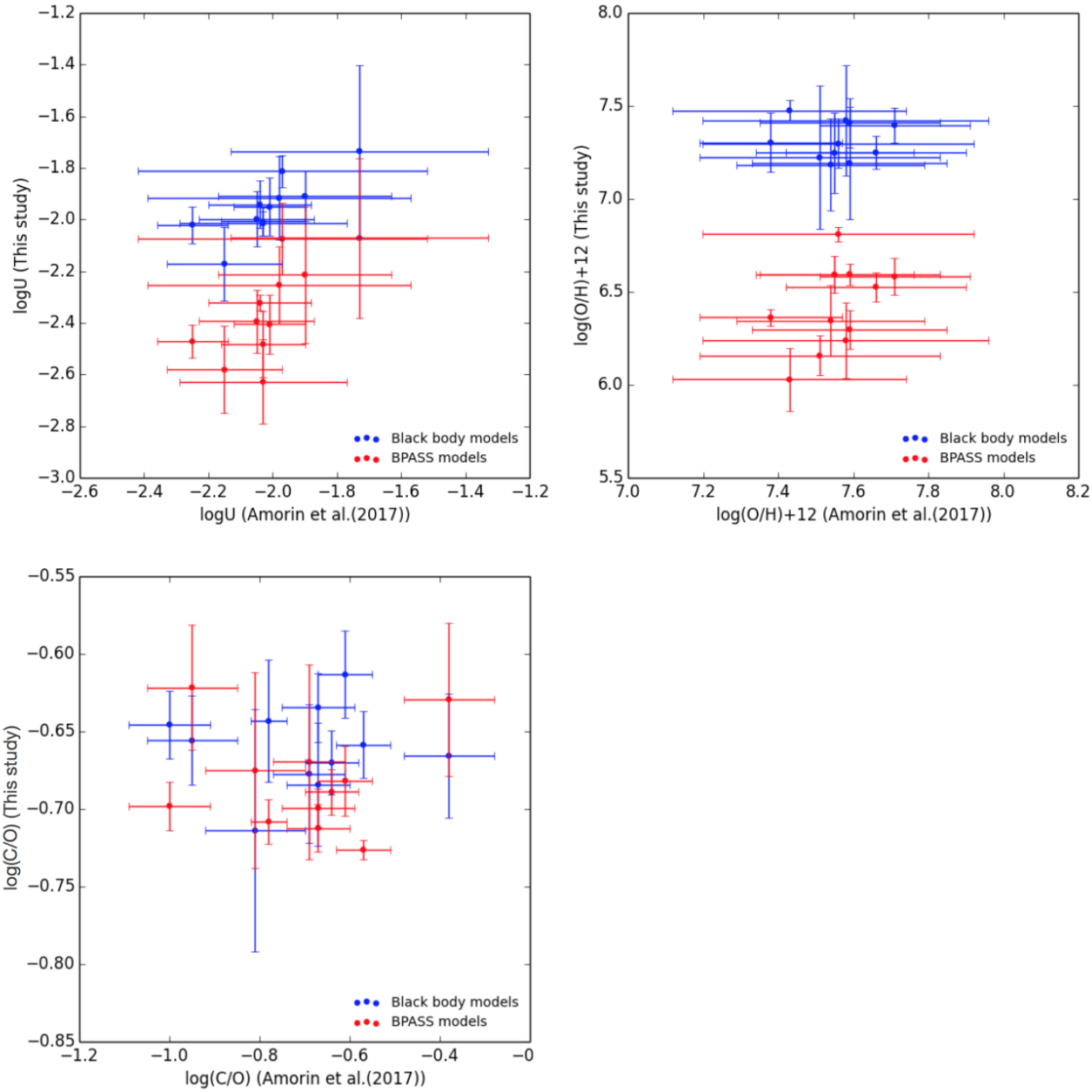

Figure 4.3: Comparison between log U, log(O/H)+12 and log(C/O) obtained with BPASS and black body models vs Amorín et al. (2017) results.

As referred before the log(C/O) obtained for some galaxies is different from Amorín et al. (2017) while it remains relatively similar for both black body and BPASS models, with some variations from higher or lower metallicity models that contributed for the final result of each galaxy. The small error bars of our BPASS values indicate a smaller scatter in the values obtained with each diagram which points towards a consistency among the diagrams. As discussed before log(C/O) may variate in different ways for different systems. For metal poor SFGs the values should be a value between -1 $\leq$ log(C/O) $\leq$ -0.3 (e.g Stark et al. (2014), Erb et al. (2010), James et al. (2015)). Our results are confined to our definition of C/O.

4.1.1 Predictions for the James Webb Space Telescope

Since the physics of the collisionally excited emission lines is essentially the same in the UV and in the optical range of energies, the physical conditions that cause these extreme UV line ratios can be used to predict their optical counterpart emission lines.

For the 10 SFGs and the composite we computed emission line-ratios of [OIII]λ5007, Hα(λ6563), [OII]λ3727 and Hβ(λ4861) to CIII]λ1909 and OIII]λ1665 respectively, and we used the Amorín et al. (2017) flux measurements of these UV lines (see Appendix D) to predict the indicated optical emission lines. Both results are presented in Table 4.3.

Table 4.3: Predictions of optical emission line fluxes for [OIII]λ5007, Hα(λ6563), [OII]λ3727 and Hβ(λ4861) based on CIII]λ1909 (a) and OIII]λ1665 (b) calibrations. Fluxes are given in 10^{-18} erg s^{-1} cm^{-2}.

VUDS ID	[OIII]^a	[OIII]^b	Hα^a	Hα^b	[OII]^a	[OII]^b	Hβ^a	Hβ^b
510583858	4.88 ± 0.03	7.72 ± 0.05	53.78 ± 0.02	85.02 ± 0.02	0.37 ± 0.74	0.58 ± 0.74	18.89 ± 0.02	29.86 ± 0.02
510838687	12.36 ± 0.02	6.95 ± 0.03	24.95 ± 0.02	14.02 ± 0.03	0.88 ± 0.25	0.49 ± 0.25	8.71 ± 0.03	4.89 ± 0.03
511267982	15.37 ± 0.03	9.42 ± 0.03	43.03 ± 0.02	26.36 ± 0.02	1.01 ± 0.32	0.61 ± 0.32	15.04 ± 0.03	9.22 ± 0.03
5100534435	4.19 ± 0.04	5.62 ± 0.03	13.47 ± 0.04	18.08 ± 0.02	0.33 ± 0.34	0.45 ± 0.38	4.71 ± 0.04	6.32 ± 0.03
5100565880	19.46 ± 0.04	9.76 ± 0.05	135.92 ± 0.02	68.18 ± 0.02	0.83 ± 2.32	0.42 ± 2.31	47.82 ± 0.03	23.99 ± 0.03
5100750978	6.79 ± 0.02	5.48 ± 0.04	23.43 ± 0.02	18.91 ± 0.03	0.51 ± 0.31	0.41 ± 0.32	8.17 ± 0.02	6.60 ± 0.04
5100994378	14.71 ± 0.02	10.01 ± 0.04	158.54 ± 0.02	107.84 ± 0.02	1.34 ± 0.43	0.91 ± 0.43	55.28 ± 0.01	37.60 ± 0.02
5100998761	15.96 ± 0.02	10.37 ± 0.03	71.20 ± 0.01	46.27 ± 0.02	1.05 ± 0.28	0.68 ± 0.28	24.85 ± 0.02	16.15 ± 0.03
5101421970	12.20 ± 0.03	14.61 ± 0.04	92.27 ± 0.02	110.56 ± 0.02	0.30 ± 1.96	0.36 ± 1.96	32.32 ± 0.03	38.73 ± 0.02
5101444192	9.79 ± 0.02	7.24 ± 0.03	32.29 ± 0.01	23.89 ± 0.02	0.68 ± 0.30	0.50 ± 0.31	11.23 ± 0.02	8.31 ± 0.03
Composite	9.48 ± 0.02	8.01 ± 0.04	62.28 ± 0.01	52.61 ± 0.01	0.48 ± 1.03	0.41 ± 1.03	21.69 ± 0.01	18.32 ± 0.02

The obtained values for the optical emission lines are in range of the expected values for an extreme ionizing population of galaxies with high star formation rates. They present both high Hα, Hβ and higher [OIII]λ5007 to [OII]λ3727. Strong optical emission line emitters discovered at z $\sim$ 1.5 $-$ 3 are also associated with low mass SFGs. Their optical emission lines are in the range of the obtained values (e.g. Masters et al. (2014)), even though the connection between the low mass population of strong UV emission line and optical emitters is not completely established. Strong optical emitters have already been found at higher redshifts (e.g. Stark et al. (2013)), particularly identified by their blue colours which indicated an extreme population of [OIII]+Hβ emitters (Smit et al. (2015)) that lie at range z $\gtrsim$ 6 (Stark et al. (2014)). This population of galaxies are of great interest to probe our optical emission line predictions, while probing the nature of these galaxies.

The discrepancy of the values obtained with CIII] and OIII] translates the variation of C/O. According to our calculations, the sample has log(C/O) $\sim$ -0.67 (C/O $\sim$ 0.2), therefore line fluxes of carbon are around 20% higher than those of oxygen lines. For this reason, the calibration with CIII] originates, in general higher emission line fluxes for the optical lines. Major disparities can be found in three sources (VUDS ID: 510583858, 5100534435, 5101421970) where Amorín et al. (2017) obtained values of log(C/O) smaller than the ones we estimated for the sources. In these cases, the emission line fluxes calculated through the carbon line are underestimated, and the calibration with OIII] is higher in all the optical lines. Nevertheless, the estimated emission line fluxes for the optical lines are only an approximation and can provide information about the range of fluxes that can be measured for these type of sources when observed in their optical rest-frame.

4.2 Bright LAEs at z ∼ 2 - 3

In Sobral et al. (in prep) we present the spectroscopic follow-up of a population of bright Lyα (LAEs) at z ∼ 2 - 3, found with narrow band surveys in the COSMOS, Boötes, UDS and GOODS-N fields. They were observed with DEIMOS (Keck), ISIS (WHT) and X-SHOOTER (VLT). The goal of our study is to improve the understanding of bright LAEs at z ∼ 2 − 3, by studying their properties and revealing their nature. We identified AGNs within the sample by searching for broad Lyα lines (FWHM > 1000 km s^{-1}), ionization energies above 50 eV and X-ray detections.

In here we analyse 6 galaxies presented in Sobral et al. (in prep), which show simultaneously the UV emission lines CIII], CIV, HeII and OIII] (for one of them: BR3), using our UV line ratio diagrams. BR3 was identified in Sobral et al. (in prep) as a narrow line AGN and B-16 as a potential narrow line AGN. BR3 is the most luminous LAE ($L_{Ly\alpha} = 43.8$ erg s^{-1}) with other strong UV emission lines but weak OIII], which indicates a high ionizing source. We used the SFGs and AGNs models from Feltre et al. (2016) and our black body models to interpret the nature of these sources. Four of these LAEs are identified as SFGs in Feltre et al. (2016) diagnosis diagrams and two as AGNs. We also used our power law models and black body models as a diagnosis and in order to investigate how clear these line ratios depend on the temperature. Three of these SFGs are consistent with effective temperatures of ∼ 70000K, while one should be more consistent with lower temperatures. According to our black body models, the AGNs of the sample have temperatures up to 100000K. We now present also the results obtained with our BPASS models (Figure 4.4).

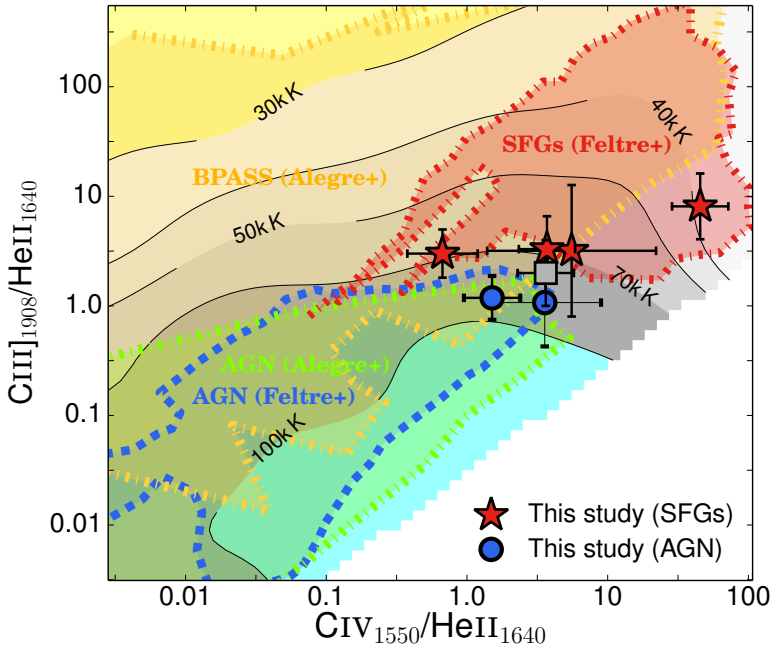

Figure 4.4: Ratios between CIII], CIV and HeII for the six LAEs. The red stars correspond to SFGs (B-21847, B-10-25068, GN-1-ISIS, GN-3378), the blue circles to AGNs (BR3 and B-16-43478) and the square to the stack of the sample. Figure adapted from Sobral et al. (in prep), where we used SFGs (red area) and AGNs (blue area) models from Feltre et al. (2016); and our BPASS SFGs (yellow area) and AGN power law models (green area) as a tool to distinguish the nature of these galaxies. The temperature of our black body models is indicated in the background.

The AGNs on Figure 4.4 are very close to the lowest effective temperature reached by our power law models. One of them (BR3) can be reached by our BPASS models with lowest metallicity which can produce higher ionizing energies. We next present an analysis of these sources using our black body and BPASS models. The emission line diagrams used for diagnosis are presented in Figure 4.5.

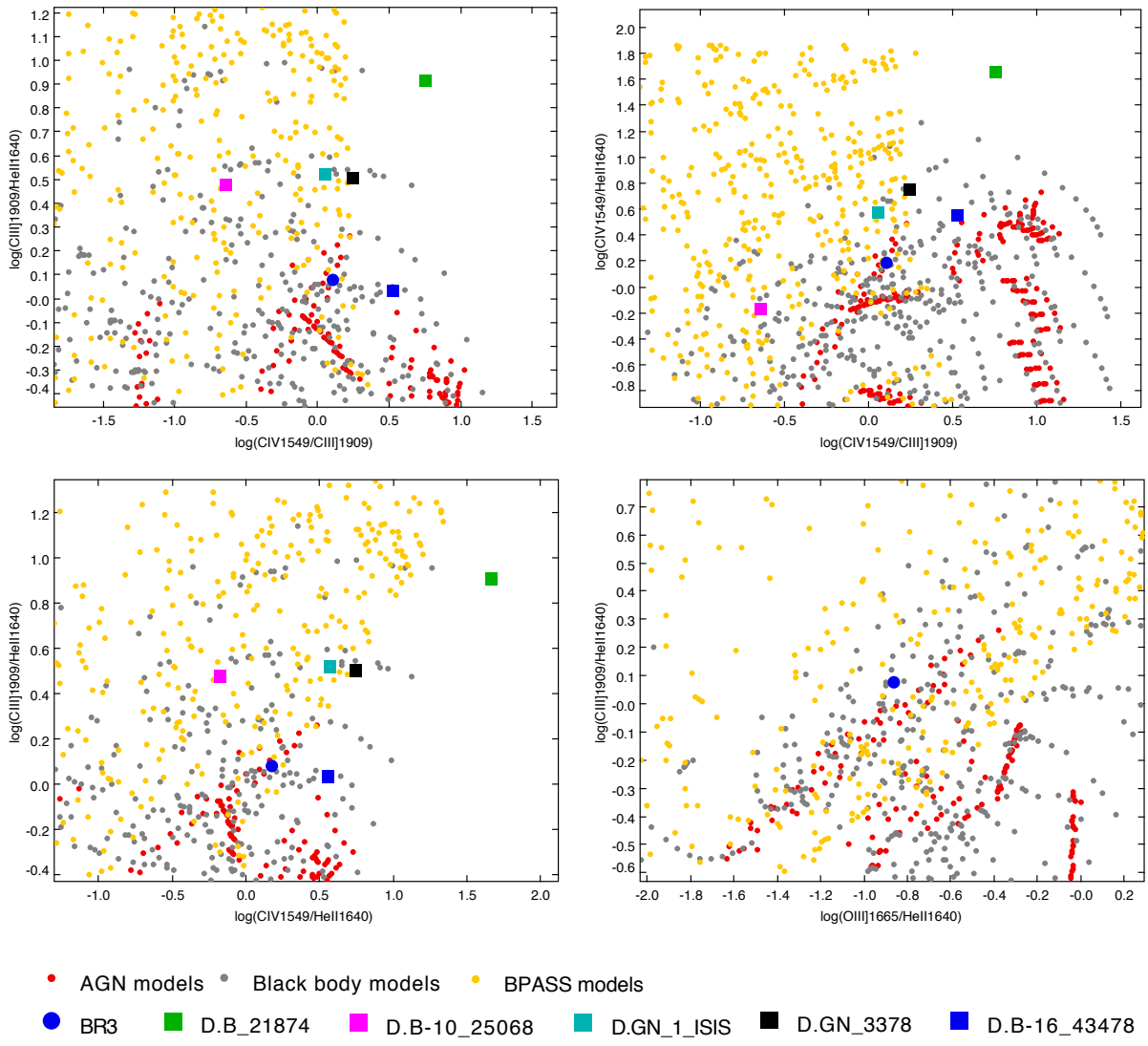

Figure 4.5: Emission line ratio diagrams involving CIII], CIV and HeII for the 6 LAEs, and OIII] for BR3.

We do not have coverage for one of the sources with our models (B-21874) mainly because this galaxy should present lower temperature. Moreover, the computed line ratios for B-21874 are based in a non detection of HeII (i.e. the value of HeII is the error of the measurement) which produces higher values on both ratios and an offset on the diagram. Besides that this galaxy displays features in its spectrum characteristic of outflows, probably powered by supernovae events, which increases its complexity (see Sobral et al. in prep).

We analyse the other five sources using our black body models and four using our BPASS models using as a fixed criteria of 0.3 difference in each line ratio. The results are presented in Tables

4.4 and 4.5 respectively. Note that once again temperatures, stellar metallicities, gas densities and nebular metallicities in $Z_\odot$ are biased to higher values, as explained in Section 4.1.

Table 4.4: Properties of the five LAEs estimated with our black body models

ID	log U	Temperature (K)	Density (cm^{-3})	Z_{ISM} ($Z_\odot$)	log(C/O)	log(O/H)+12
B-16_43478	-1.44 ± 0.02	90794 ± 1391	32173 ± 1589	0.503 ± 0.010	-0.63 ± 0.01	7.91 ± 0.04
GN_3378	-1.44 ± 0.02	66852 ± 1654	30159 ± 4233	0.318 ± 0.044	-0.69 ± 0.02	7.57 ± 0.09
GN_1_ISIS	-1.60 ± 0.05	68929 ± 4871	30106 ± 1628	0.390 ± 0.050	-0.62 ± 0.02	7.48 ± 0.17
B-10_25068	-2.04 ± 0.01	66280 ± 1533	14414 ± 8230	0.455 ± 0.017	-0.59 ± 0.01	7.52 ± 0.11
BR3	-1.94 ± 0.29	110461 ± 10273	19517 ± 5361	0.646 ± 0.177	-0.55 ± 0.08	8.01 ± 0.26

In general these sources are consistent with having high temperatures, in particular the ones that fall into the AGN region (BR3 and B-16). The temperature results are contaminated by models with higher temperatures and the obtained values should be seen as an upper limit. Their relatively higher nebular metallicity log(O/H)+12 of 7.91 and 8.01 (both close to ~ 0.2 $Z_\odot$) can better describe an AGN behaviour than a SFG.

Overall these two sources present higher nebular metallicity and higher temperature in relation to the SFGs. For BR3 the higher log(C/O) is also consistent with a sub-solar nebular metallicity, while for B-16 contributions from both higher and lower log(C/O) values at a slightly lower nebular metallicity drop this parameter. The ionization parameter of B-16 is very high, again pointing to an AGN.

However, it is interesting to note that the SFGs also present higher ionization parameters in the range of the AGNs. These can be better explained with our BPASS models. The three SFGs are consistent with lower nebular metallicity log(O/H)+12 of $7.48 - 7.57$ ($\sim$ 0.07 - 0.08 $Z_\odot$). The obtained temperatures are contaminated by higher values, as referred before, being this effect more evident for the obtained density values, which are again contaminated by higher values. More realistic densities can be achieved with our BPASS models.

We follow the same approach as before and we estimated the physical properties for just four of these galaxies with our BPASS models (since B-16 is out of range). Besides that, B-16 measurements were not based on any non detections and according to our models they point towards an AGN which is in agreement with our work presented in Sobral et al. (in prep).

Table 4.5: Properties of the 4 LAEs estimated with our BPASS models

ID	$Z_{STELLAR}$	log(age/yrs)	log U	Density(cm^{-3})	Z_{ISM} ($Z_\odot$)	log(C/O)	log(O/H)+12
GN_3378	0.0017 ± 3.21E-4	6.31 ± 0.04	-1.74 ± 0.06	394 ± 52	0.027 ± 0.022	-0.69 ± 0.02	6.41 ± 0.11
GN_1_ISIS	0.0021 ± 1.46E-4	6.48 ± 0.04	-1.84 ± 0.06	398 ± 41	0.037 ± 0.002	-0.70 ± 0.01	6.41 ± 0.09
B-10_25068	0.0032 ± 1.47E-4	6.67 ± 0.02	-2.48 ± 0.04	1985 ± 259	0.014 ± 0.004	-0.72 ± 0.01	6.38 ± 0.05
BR3	0.0039 ± 7.19E-4	6.39 ± 0.22	-2.99 ± 0.31	8064 ± 13302	0.071 ± 0.067	-0.52 ± 0.09	5.57 ± 0.39

Above all this is just an approximation for the expected physical properties of these galaxies since we did not take into account the errors in the computed line ratios, and the non emission line detections (HeII was not detected in GN-3378 and B-10-25068) and CIII] was also not detected in GN-3378.

The values obtained for BR3 reveal a nebular metallicity much lower than the ones estimated for

Amorín et al. (2017) galaxies with log(O/H)+12 = 5.57 (5.58×10^{-4} $Z_\odot$). The value of log(C/O) obtained translates this metallicity. BPASS also estimates a high density system ($\sim 10^3 - 10^4$ cm^{-3}) with a population with a stellar metallicity of $0.2 - 0.3$ $Z_\odot$ and a very low ionization parameter. This would require an extremely ionizing SED which is unlikely at this stellar metallicity and stellar age.

In general the nebular metallicity estimated with our BPASS models for the three SFGs are in the range of values obtained for Amorín et al. (2017) galaxies, where log(O/H)+12 $\sim$ 6.4 (0.005 $Z_\odot$), which translates also a similar log(C/O) value.

However, for two of the three galaxies (GN-3378 and GN-1-ISIS), log U is much higher than for Amorín et al. (2017) galaxies. This is related with a younger stellar population with ages below $10^{6.5}$ yrs and a much more metal poor stellar population (with main contributions from $Z_{STELLAR}$ < 0.1 $Z_\odot$ models) and low density systems (with main contributions from 100 cm^{-3} models). The galaxy B-10 is the one that presents more similarities with the SFGs from Amorín et al. (2017).

In conclusion BR3 and B-16 are more consistent with being AGNs and B-10 with being a SFG with low density gas ($\sim 100 - 500$ cm^{-3}) and nebular metallicity ($\sim$ 0.005 $Z_\odot$) and with a stellar population of $\sim 10^{6.67}$ yrs and a stellar metallicity of $\lesssim$ 0.2 $Z_\odot$ (with main contributions from 0.07 $Z_\odot$ and 0.14 $Z_\odot$ stellar models).

According to our models, GN-3378 and GN-1-ISIS are lower density systems (closer to $\sim$ 100 cm^{-3}) with low nebular metallicity (0.005 $Z_\odot$) that can hold very young populations of stars with stellar metallicities $<$ 0.1 $Z_\odot$ (they are better described by the lowest $Z_{STELLAR}$ BPASS SED). They also have a younger age, which requires higher ionization parameters (log U $\sim$ -1.8 $-$ -1.7).

The range of extreme physical properties obtained for these two last sources could create some doubt about their nature. However, they are not in the range of our AGN models and according to our models the AGN nature can be ruled out.

4.3 Application to z $\sim$ 6 - 7 galaxies

In Matthee et al. (2017) we used our CLOUDY black body and power-law models to compare carbon to Lyα ratios in a sample of LAEs at z $\sim 2-3$ (Sobral et al. in prep, see Section 4.2) and in a compilation of spectroscopic confirmed z $\sim 6-7$ LAEs and LBGs. The higher redshift LAEs are published in Matthee et al. (2017) (SR7 and VR7), Sobral et al. (2015) (CR7), Ouchi et al. (2009) (Himiko), Hu et al. (2016), Kashikawa et al. (2012), Bagley et al. (2017), Shibuya et al. (2017), Shimasaku et al. (2006), Ouchi et al. (2005), Westra et al. (2006); and the LBGs are from Willott et al. (2013), Richard et al. (2011), Mainali et al. (2017), Schmidt et al. (2016), Schmidt et al. (2017), Cuby et al. (2003), Huang et al. (2016), Ono et al. (2012), Iye et al. (2006), Vanzella et al. (2011), Stark et al. (2015), Stark et al. (2017), Finkelstein et al. (2013) and Oesch et al. (2015).

No rest-UV metal-lines were detected in SR6, VR7, Himiko and CR7. Our models were used to explore whether this is due to the limited depth of the observations or it could be attributed to any other physical condition (e.g. low metallicity). The sample was selected based on the availability of limits of other UV emission-lines besides Lyα. The line ratios were computed by correcting for Lyα escape fraction empirically. The physics behind the Lyα escape fraction is complex, in particular for z > 6 due to the high neutral fraction of the IGM, and its estimation is difficult. An approximation can be made using Lyα EW, which allows to estimate the intrinsic value for Lyα. This was done with the fit from Sobral et al. (2017), who used galaxies at z = 2.2:

$$f_{\rm esc,Ly\alpha} = 0.006\ {\rm EW}_{\rm Ly\alpha,0} - 0.05\ \ [5 < {\rm EW}_{\rm Ly\alpha,0} < 175], \tag{4.1}$$

where $f_{\rm esc,Ly\alpha}$ is the Lyα escape fraction. The fit should provide an underestimated value for the Lyα escape fraction since the IGM transmission decreases between z = 2.2 − 6.6 (Laursen et al. (2011)). The observed line-ratios were calculated using the relation:

$$\frac{f_{\rm CIII]}}{f_{\rm Ly\alpha}} = \frac{\alpha}{f_{\rm esc,Ly\alpha}} \quad ; \quad \frac{f_{\rm CIV}}{f_{\rm Ly\alpha}} = \frac{\alpha}{f_{\rm esc,Ly\alpha}}, \tag{4.2}$$

where α is the estimated intrinsic line-ratio with respect to Lyα. For CIV, we selected models with values of α between 0.015 and 0.1, where our models assume a $f_{\rm esc,Ly\alpha} = 1$. These values correspond to a black body with effective temperature $\approx$ 70000K and metallicity of 0.01 $Z_\odot$, and to an AGN (power law slope) with a metallicity of 0.1 $Z_\odot$, respectively. α decreases rapidly in the case of lower metallicity or lower effective temperature. For CIII], we used values from $\alpha = 0.005$ ($T_{\rm eff} \approx$ 70000K, Z= 0.01 $Z_\odot$) to $\alpha = 0.022$ for the same AGN model as described above. From comparison with the LAEs from the literature our upper detection limits are higher than for the majority of the other sources (see Matthee et al. (2017), Table 4), which already indicates that the observations were not deep enough. In the CIV/Lyα ratio for z $\approx$ 6 - 7, the detections and upper limits increase for higher luminosities, while for z $\approx$ 2 - 3 they decrease. In the CIII]/Lyα ratio, higher ratios correspond to higher UV luminosities for both z $\approx 6-7$ and z $\approx 2-3$. The CIV detections for z $\approx 6-7$ sources are closer to the expected line-ratios from our AGN models than from the SFGs (see Figure 4.6). Assuming a higher temperature result in higher CIV/Lyα ratio, however higher emission line ratios can only be explained by our AGN models (see Figure 4.7).

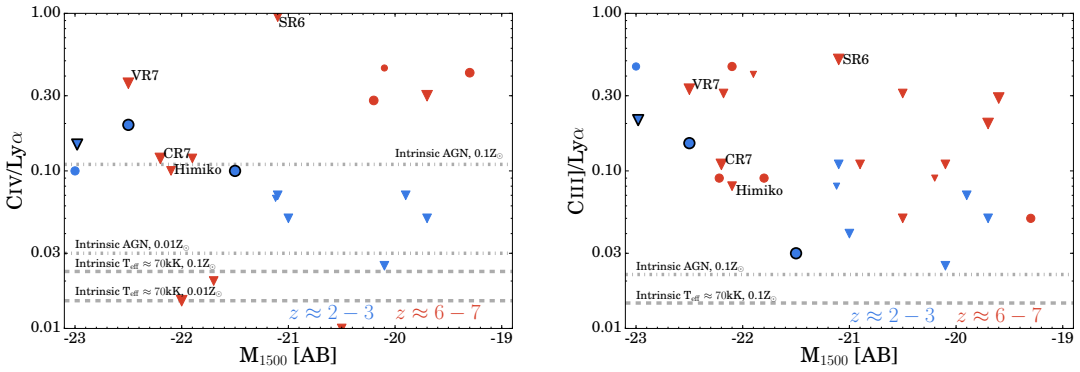

Figure 4.6: Observed CIV/Lyα and CIII]/Lyα ratios as a function of M_{1500} for luminous LAEs at $z \approx 2-3$ (Sobral et al. in prep) and the compilation of LAEs and LBGs at $z \approx 6-7$. Upper limits are shown with down-ward pointing triangles. Detections are shown with circles. The confirmed AGN sample is highlighted with black edges. The dashed horizontal lines correspond to estimated intrinsic line-ratios calculated with our black body and power law models.

According to our models the higher CIV/Lyα and CIII/Lyα ratios are below the limits for these sources, in particular for the SFGs, which indicates low Lyα escape fractions, in particular for z $\approx 6-7$. Some of the Lyα emission can also be lost since Lyα luminosities from these sources are estimated from slits, where a significant fraction of the light can be missed due to its extended emission. Detected Carbon to Lyα ratios are already close to those modelled with our black body models. With our BPASS models these ratios increase slightly at 0.1 $Z_\odot$ in relation to a black body with 70000K, being the two values much alike.

The CIV limits observed in Himiko are more consistent with a SFG or an AGN with a very low metallicity ~ 0.01 $Z_\odot$, while for the rest it may indicate a low escape fraction. With the current limits for SR6, CR7 and VR7 this analysis concludes that we would have to go a factor $5-10$ deeper to detect CIV and CIII].

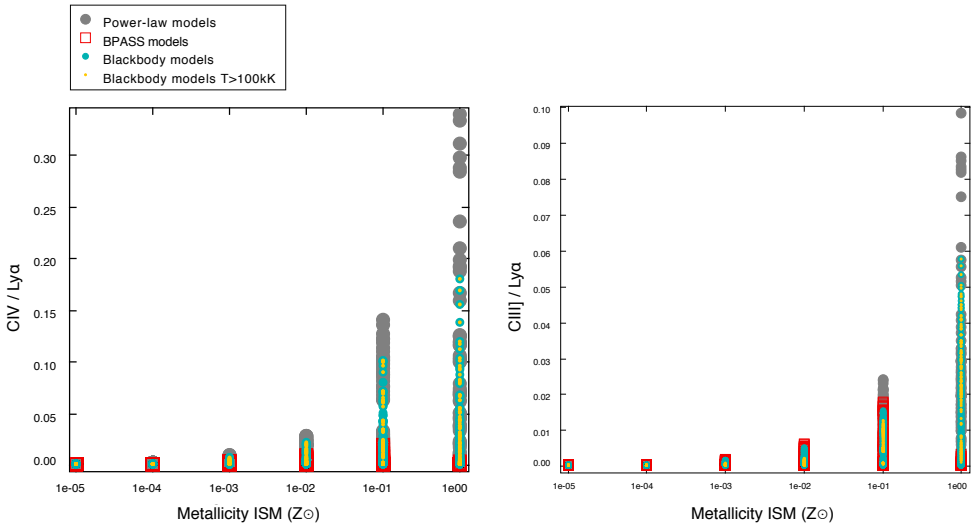

Figure 4.7: CIV/Lyα and CIII]/Lyα for all the models used in this work. Just AGNs with a $Z_\odot$ can reach higher ratios. For SFGs the higher ratios carbon to Lyα are reached at 0.1 $Z_\odot$. The maximum value reached by our BPASS models of CIV/Lyα is ~ 0.04 and for CIII]/Lyα ~ 0.02 .

Chapter 5

VIMOS - HiZELS SFGs

5.1 HiZELS Survey

In this work we also analyse data from the High-redshift(Z) Emission Line Survey (HiZELS; e.g. Geach et al. (2008), Sobral et al. (2012)), which is an extragalactic survey conducted using the wide field camera (WFCAM) on the 3.8 meter telescope on the United Kingdom Infrared Telescope (UKIRT) on Mauna Kea, Hawaii. These galaxies were selected using the narrow-band (NB) filters in the i, J, H and K bands to detect emission-line galaxies at z = 0.40, z = 0.84, z = 1.47 and z = 2.23, in particular Hα emitters (e.g. Geach et al. (2008), Sobral et al. (2014)). The emission line emitters from HiZELS are selected by the narrow-band excess imaging (Figure 5.1).

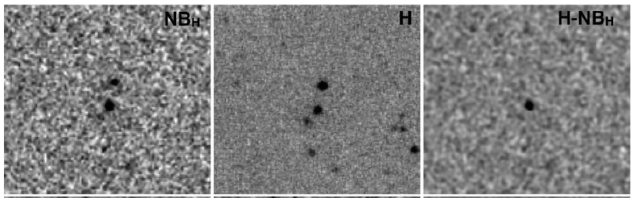

Figure 5.1: Example of a NB-H emitter (narrow-band excess selected) from Sobral et al. (2012). The non-emitters disappear by the subtraction of the broad (centre) and narrow (left) bands, leaving the isolated emitter (right).

The Hα emission line is sensitive to star formation (e.g. Kennicutt et al. (2003)) and is not strongly affected by dust extinction. HiZELS can detect SFGs at different epochs near the peak of star formation history of the Universe ($z \sim 2 - 3$, e.g. Bouwens et al. (2015), Sobral et al. (2014)).

5.2 Spectroscopic data overview

A total of 425 sources were selected from HiZELS using NB excess imaging within the Ultra Deep Survey field (UDS, 0.8 square degrees) and observed with the low resolution grism of VIMOS (VLT) instrument (See Appendix E).

The 2-D spectroscopic data was visually inspected to identify any systematic reduction problems and to extract the position of the spectrum on each slit. This allows to extract the 1-D spectra and to assign a quality flag for each source. From the total observed NB galaxies, 87 correspond to emission

line galaxies ($\sim$ 20 %). In a preliminary analysis of the data we obtained spectroscopic redshifts by identifying the emission lines given in Table 2.1 which was done visually. After that, we performed Gaussian fits to the available emission lines to calculate accurate redshifts and measurement errors, where the best redshift values corresponds to the mean of the values calculated for all the emission lines found in the spectrum. Along with that a Gaussian smoothing was performed to the 1-D spectra. The redshift distribution of the total sample (107 sources, which include 20 additional galaxies, for which spectroscopic redshift information was available) is shown in Figure 5.2. The comparison between the estimated photometric redshift and the measured spectroscopic redshift is presented in Figure 5.3.

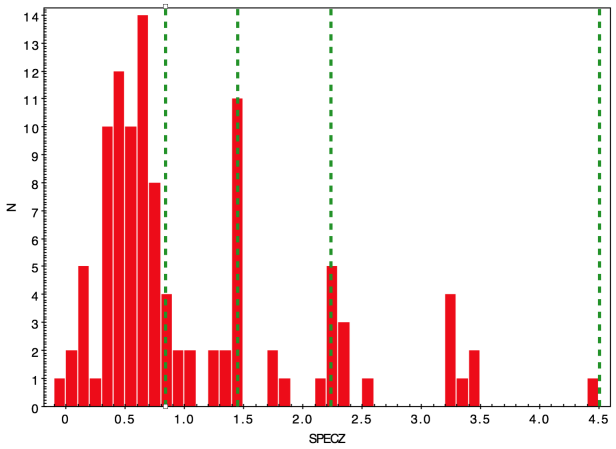

Figure 5.2: The obtained spectroscopic redshift (SPECZ) distribution shows that a higher number (N) of NB galaxies have redshift around specific values. This result is expected from the NB selection of Hα with the different filters. The detections of [OII] λ3727 at 6840 Å confirm the NB-J detections of Hα at z = 0.84, while MgII at 6916 Å allows to confirm the NB-H detections of Hα at z = 1.47 and the Lyα detections at 3930 Å confirm the NB-K detections of Hα at z = 2.23 and higher.

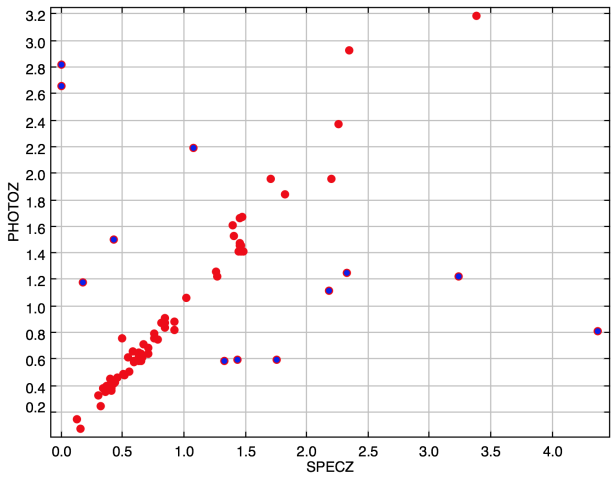

Figure 5.3: Comparison of photometric redshifts (PHOTOZ) vs calculated spectroscopic redshifts (SPECZ). In general the spectroscopic redshifts obtained are in good agreement with the photometric redshifts available (red markers). For 12 sources (blue markers) the photometric redshift values do not correspond to the redshifts obtained by spectroscopy, mainly due to contamination by emission lines of [OII]λ3727 below z $\sim$1 and Lyα from high-redshift AGNs.

5.3 Analysis of 2 HiZELS SFGs at z ∼1.46

From the total sample described before, 38 galaxies have z > 1, where 18 correspond to redshifts obtained from an external catalogue, meaning that we do not have emission line spectra available. We selected galaxies with z $\gtrsim$ 1.5, high quality spectra and with at least 2 emission lines (15 galaxies, 1.5 $\lesssim$ z $\lesssim$ 3.5.). From this sample 8 galaxies were classified as broad line AGNs and other 5 galaxies (with higher redshifts) presented just Lyα emission and Nv or Civ. We analysed 2 galaxies of the sample with both HeII, CIII] and Civ at z ∼ 1.46, which are presented next. These 2 galaxies where selected by the NB-H filter which selects Hα emitters at z ∼ 1.47 (see Table 5.1). Both the 1-D and 2-D spectra are shown in Figure 5.4.

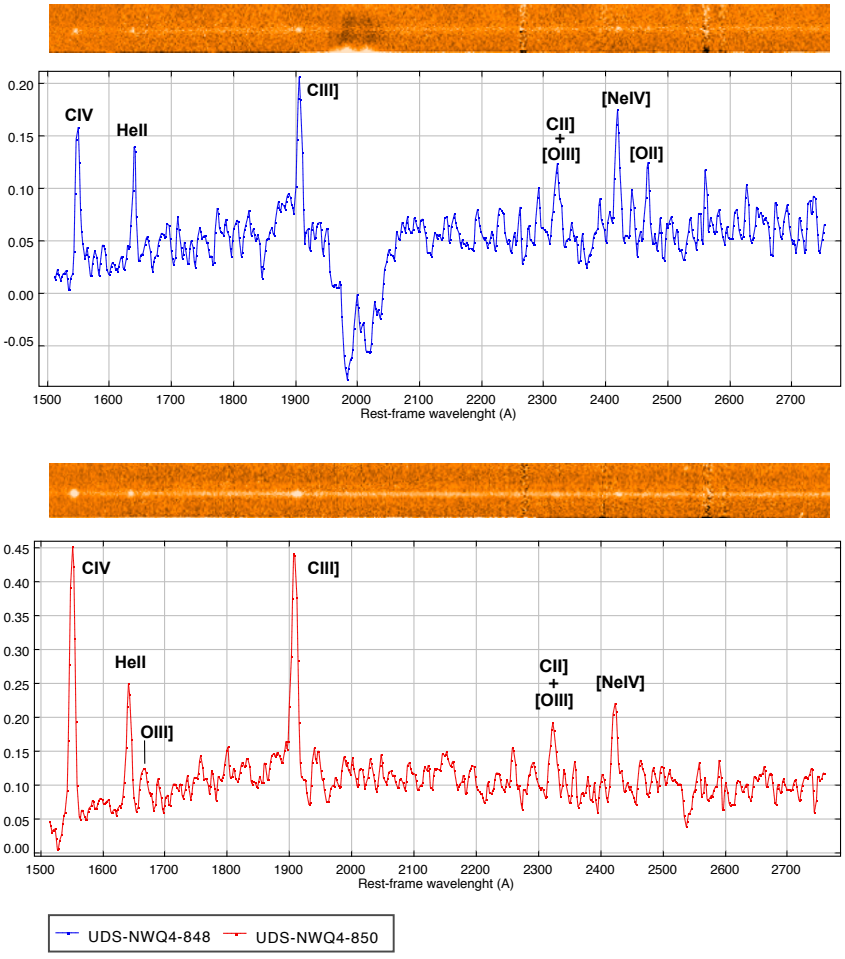

Figure 5.4: 1-D and 2-D spectra for the two HiZELS galaxies at z ∼ 1.46, NB-H selected galaxies, with indication of the respective emission lines presented in the spectra. UDS-850 is brighter than UDS-848 and all the lines have higher S/N.

Table 5.1: VIMOS ID, pointing and quadrant of observation for the two HiZELS galaxies of the sample selected by the NB-H filter which present both HeII, CIII] and CIV, and respective spectroscopic redshift calculated in this study.

Pointing	Quad	ID	RA	Dec	Mag	$z_{photometric}$	$z_{spectroscopic}$
UDS-NW	Q4	848	34.135	-4.782	19.97	1.45	1.460 ± 0.002
UDS-NW	Q4	850	34.189	-4.807	19.26	1.45	1.457 ± 0.002

We then analysed these two galaxies using three emission line ratios that include HeII, CIII] and CIV emission lines. The OIII] emission line was not used in this study because its low S/N. The CIV and CIII] cannot also be resolved and we computed the total emission of the doublet as in the previous chapter. The line-fluxes were measured by the integration of the emission line and respective subtraction of the continuum emission. The line-ratio diagnosis diagrams are presented in Figure 5.5.

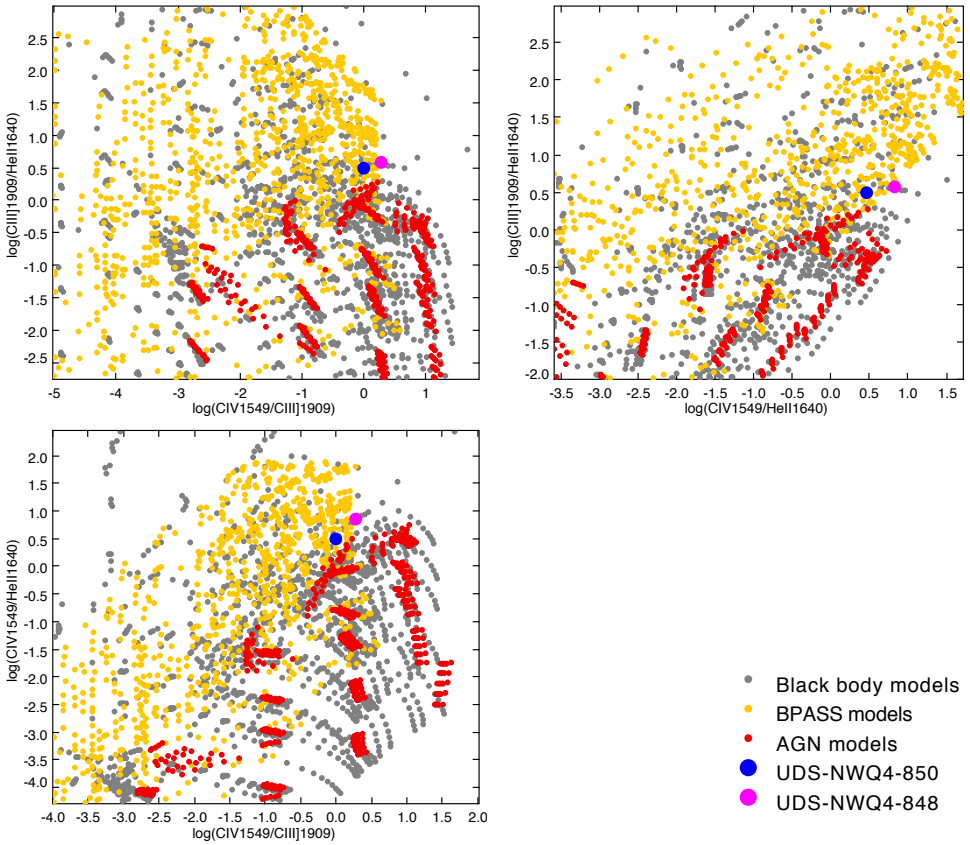

Figure 5.5: Emission line ratio diagrams involving CIII], CIV and HeII emission lines for the two HiZELS galaxies at z ∼ 1.46.

Table 5.2: Properties of the two HiZELS galaxies obtained with our black body models

ID	log U	Temperature (K)	Density (cm^{-3})	Z_{ISM} ($Z_{\odot}$)	log(C/O)	log(O/H)+12
848	-1.35 ± 0.04	65831.50 ± 1598.42	29635.71 ± 6230.77	0.288 ± 0.032	-0.73 ± 0.03	7.61 ± 0.01
850	-1.64 ± 0.05	71119.20 ± 2790.75	32858.82 ± 2854.93	0.365 ± 0.076	-0.63 ± 0.03	7.44 ± 0.10

Table 5.3: Properties of the two HiZELS galaxies obtained with our BPASS models

ID	$Z_{STELLAR}$	log(age/yrs)	log U	Density (cm^{-3})	Z_{ISM} ($Z_\odot$)	log(C/O)	log(O/H)+12
848	0.0017 ± 4.67E-4	6.29 ± 0.04	-1.74 ± 0.14	356.56 ± 43.44	0.031 ± 0.021	-0.69 ± 0.03	6.51 ± 0.12
850	0.0021 ± 7.05E-5	6.55 ± 0.03	-1.85 ± 0.06	386.29 ± 9.79	0.034 ± 0.002	-0.71 ± 0.02	6.37 ± 0.05

The physical parameter estimated for the two HiZELS-VIMOS galaxies with both our black body models and our BPASS are identical to the ones obtained for the two bright LAEs GN-3378 and GN-1-ISIS from Sobral et al. (in prep) in Section 4.2.

According to our BPASS models, UDS-848 and UDS-850 are low density systems (better described by $\sim$ 100 cm^{-3} models) with very low gas metallicities of log(O/H)+12 = 6.37 (0.005 $Z_\odot$) and 6.51 (0.007 $Z_\odot$), which can be better explained by young stellar populations with metallicities of $Z_{STELLAR}$ = 0.0017 (0.12 $Z_\odot$) and $Z_{STELLAR}$ = 0.0021 (0.15 $Z_\odot$), respectively. However, they both suffer main contributions from models with $Z_{STELLAR}$ = 0.001 (0.07 $Z_\odot$). For that reason, their $Z_{STELLAR}$ should be more consistent with a value bellow 0.1 $Z_\odot$. Due to the younger age a higher ionization parameter is required, as explained in the previous chapter.

These galaxies were selected by their bright Hα line which is a star formation tracer. For these reason it is easier to find galaxies with more extreme stellar populations than UV continuum selected galaxies such as Amorín et al. (2017) galaxies. The same happens with the two bright LAEs (Lyα selected) from Sobral et al. (in prep) which present similar properties to these two HiZELS-VIMOS galaxies.

Chapter 6

Conclusions

In this work we have demonstrated the importance of using different photoionization models to interpret the physical properties of high redshift systems. We also demonstrate the importance of using Evolutionary Synthesis models that uses binary and rotation effects.

We modelled the radiation field using a black body with different temperatures. This avoids uncertainties inherent to the Evolutionary Synthesis models used to predict the ionizing spectra of massive stars in high redshift galaxies. This also constrains the effective shape of the ionization radiation field and the ionizing photons required to produce the observed emission line ratios. We varied our physical parameters within a broad range of temperatures (20000 - 150000 K), densities (10^2 - 10^5 cm^{-3}) and metallicities ($1 - 10^{-5}$ $Z_\odot$), even though in some cases the combination of some conditions can return models with unphysical meaning.

The broad range of our models allow to obtain emission line ratios associated with both SFGs and AGNs. While SFGs can be described by black bodies with temperatures below $\sim$ 70000K, AGNs are associated with models with higher temperature.

SFGs temperatures below $\sim$ 70000K are in reasonable agreement with the ones estimated by Steidel et al. (2014), which found that a black body with temperatures $\sim$ 50000K - 60000K could describe the distribution of a sample of 251 galaxies with high star formation rates at z $\sim$ 2.3. This range of temperatures is required to reproduce harder radiation fields associated with high ionization lines. High ionization parameters are also required to produce emission lines such as CIV and OIII], which require 47.9 eV and 35.1 eV, respectively.

Our BPASS models provide a more realistic scenario for the ionization field which is produced by galaxies holding massive stars. Binary and rotation effects can extend the star lifetime, where the star can live in a quasi-estatic evolution in the main sequence for much more time than previously thought, providing ionizing photons for longer time (i.e. maintaining the ionization radiation for longer time), while rotation can expose hotter components of the stars due to fast binary interacting winds. These stellar models are capable of producing the predicted high radiation field created by our black body models below $\sim$ 70000K.

Our AGN models were modelled using the same range of conditions of our black body models (except for the temperature). For high temperatures our black body models provide similar results to our power law (AGN) models.

The results obtained for the 10 SFGs of Amorín et al. (2017) using our black body models revealed to be closer to the ones obtained by a single stellar population.

Only BPASS models can explain the presence of these high ionization lines in the spectra without invoking extreme high ionization parameters. The impact of massive stars in the observable spectra of a SFG suggests an important role played by massive stars in distant galaxies, which should be taken into account when modelling these systems, in particular in metal poor conditions.

When modelling high-redshift galaxies it is also important not to assume that the stellar metallicity is equal to the gas metallicity. Our analysis of the data revealed very different values for these two abundances. This is in agreement with Steidel et al. (2016) and reflects the initial solar abundance used in the massive stellar models. This also implies that log(C/O) of these stellar models reflect a linear scaling from the solar value, being different from the observations. The same happens with log(N/O). The creation of evolutionary models that include both binary and rotation effects taking in consideration the relative abundances of these elements for non solar metallicities would provide more accurate results.

While Amorín et al. (2017) used models where the metallicity was the same for both the gas and the stellar population and obtained metallicity values ~ 0.1 and 0.05 $Z_{\odot}$, with our models we obtained a higher stellar metallicity (~ 0.2 and 0.1 $Z_{\odot}$) but a much lower gas metallicity.

It is also important to take into account our definition of C/O in relation to the definition of Amorín et al. (2017). These discrepancies have an important impact on our predictions of optical emission line fluxes to be observed and will finally be able to be tested with James Webb Space Telescope.

While one of the bright LAEs from Sobral et al. (in prep) presents similar properties to Amorín et al. (2017) galaxies, other two suggest a younger stellar population ($< 10^{6.5}$ yrs) with lower stellar metallicity values (< 0.1 $Z_{\odot}$), similar to the properties obtained for the two HiZELS-VIMOS galaxies. These were both emission line selected galaxies through Lyα and Hα lines, respectively. Contrarily to older BPASS models, starburst at such younger ages require more extreme stellar populations with lower metallicity and higher ionization parameters.

These young and metal-poor SFGs with high ionization parameters, can help to provide a connection between a population of strong optical emitters at higher redshifts. At the same time, searching for UV emission line features such as CIII] and CIV can provide a better way of finding these extreme low metal and highly ionizing systems. At high redshift ($z \geq 6$) several galaxies were found by their UV lines (e.g. Stark et al. (2015)). Given the strong attenuation of Lyα at high redshifts, these emission lines such emission lines can better find and probe early SFGs.

The NIRSPEc instrument on the James Webb Space Telescope will make possible observations of many SFG at $3 < z < 8$, providing evidence of the properties of the interstellar medium of high-redshift galaxies as well as measuring directly high emission line galaxies within this redshift range (or even above).

In this work we have demonstrated that the ultraviolet emission lines of CIII], CIV and OIII] combined with HeII can provide different emission line ratios diagnosis that allow to successfully estimate properties of SFGs with extreme properties at $z \sim 1.5 - 3$. These should be particularly useful to interpret the ultraviolet rest-frame of high redshift systems.

All the progress made in this field will be relevant for planning and interpreting future observations of high-redshift galaxies by the James Webb Space Telescope.

References

T. Abel, G. L. Bryan, and M. L. Norman. The Formation and Fragmentation of Primordial Molecular Clouds. *The Astrophysical Journal*, 540:39–44, Sept. 2000. doi: 10.1086/309295.

C. J. Akerman, L. Carigi, P. E. Nissen, M. Pettini, and M. Asplund. The evolution of the C/O ratio in metal-poor halo stars. *Astronomy & Astrophysics*, 414:931–942, Feb. 2004. doi: 10.1051/0004-6361:20034188.

M. A. Alvarez, J. H. Wise, and T. Abel. Accretion onto the First Stellar-Mass Black Holes. *The Astrophysical Journal, Letters*, 701:L133–L137, Aug. 2009. doi: 10.1088/0004-637X/701/2/L133.

R. Amorín, A. Fontana, E. Pérez-Montero, M. Castellano, L. Guaita, A. Grazian, O. L. Fèvre, B. Ribeiro, D. Schaerer, L. A. M. Tasca, R. Thomas, S. Bardelli, L. Cassarà, P. Cassata, A. Cimatti, T. Contini, S. D. Barros, B. Garilli, M. Giavalisco, N. Hathi, A. Koekemoer, V. Le Brun, B. C. Lemaux, D. Maccagni, L. Pentericci, J. Pforr, M. Talia, L. Tresse, E. Vanzella, D. Vergani, G. Zamorani, E. Zucca, and E. Merlin. Analogues of primeval galaxies two billion years after the Big Bang. *Nature Astronomy*, 1:0052, Mar. 2017. doi: 10.1038/s41550-017-0052.

M. Asplund, N. Grevesse, A. J. Sauval, and P. Scott. The Chemical Composition of the Sun. *Annual Review of Astronomy & Astrophysics*, 47:481–522, Sept. 2009. doi: 10.1146/annurev.astro.46.060407.145222.

M. B. Bagley, C. Scarlata, A. Henry, M. Rafelski, M. Malkan, H. Teplitz, Y. S. Dai, I. Baronchelli, J. Colbert, M. Rutkowski, V. Mehta, A. Dressler, P. McCarthy, A. Bunker, H. Atek, T. Garel, C. L. Martin, N. Hathi, and B. Siana. A High Space Density of Luminous Lyman Alpha Emitters at z $\sim$ 6.5. *The Astrophysical Journal*, 837:11, Mar. 2017. doi: 10.3847/1538-4357/837/1/11.

J. A. Baldwin, M. M. Phillips, and R. Terlevich. Classification parameters for the emission-line spectra of extragalactic objects. *Publications of the Astronomical Society of the Pacific*, 93:5–19, Feb. 1981. doi: 10.1086/130766.

S. V. W. Beckwith, M. Stiavelli, A. M. Koekemoer, J. A. R. Caldwell, H. C. Ferguson, R. Hook, R. A. Lucas, L. E. Bergeron, M. Corbin, S. Jogee, N. Panagia, M. Robberto, P. Royle, R. S. Somerville, and M. Sosey. The Hubble Ultra Deep Field. *The Astronomical Journal*, 132:1729–1755, Nov. 2006. doi: 10.1086/507302.

D. Berg, E. D. Skillman, A. R. Marble, L. van Zee, and C. W. Engelbracht. Direct Oxygen Abundances for the Lowest Luminosity LVL Galaxies. In *American Astronomical Society Meeting*

Abstracts #219, volume 219 of *American Astronomical Society Meeting Abstracts*, page 244.15, Jan. 2012.

D. A. Berg, E. D. Skillman, R. B. C. Henry, D. K. Erb, and L. Carigi. Carbon and Oxygen Abundances in Low Metallicity Dwarf Galaxies. *The Astrophysical Journal*, 827:126, Aug. 2016. doi: 10.3847/0004-637X/827/2/126.

R. J. Bouwens, G. D. Illingworth, P. A. Oesch, I. Labbé, M. Trenti, P. van Dokkum, M. Franx, M. Stiavelli, C. M. Carollo, D. Magee, and V. Gonzalez. Ultraviolet Luminosity Functions from 132 z $\sim$ 7 and z $\sim$ 8 Lyman-break Galaxies in the Ultra-deep HUDF09 and Wide-area Early Release Science WFC3/IR Observations. *The Astrophysical Journal*, 737:90, Aug. 2011. doi: 10.1088/0004-637X/737/2/90.

R. J. Bouwens, G. D. Illingworth, P. A. Oesch, M. Trenti, I. Labbé, L. Bradley, M. Carollo, P. G. van Dokkum, V. Gonzalez, B. Holwerda, M. Franx, L. Spitler, R. Smit, and D. Magee. UV Luminosity Functions at Redshifts z $\sim$ 4 to z $\sim$ 10: 10,000 Galaxies from HST Legacy Fields. *The Astrophysical Journal*, 803:34, Apr. 2015. doi: 10.1088/0004-637X/803/1/34.

R. A. A. Bowler, R. J. McLure, J. S. Dunlop, D. J. McLeod, E. R. Stanway, J. J. Eldridge, and M. J. Jarvis. No evidence for Population III stars or a Direct Collapse Black Hole in the z = 6.6 Lyman-α emitter 'CR7'. *ArXiv e-prints*, Sept. 2016.

V. Bromm and A. Loeb. Formation of the First Supermassive Black Holes. *The Astrophysical Journal*, 596:34–46, Oct. 2003. doi: 10.1086/377529.

V. Bromm and N. Yoshida. The First Galaxies. *Annual Review of Astronomy & Astrophysics*, 49: 373–407, Sept. 2011. doi: 10.1146/annurev-astro-081710-102608.

G. Bruzual and S. Charlot. Stellar population synthesis at the resolution of 2003. *Monthly Notices of the Royal Astronomical Society*, 344:1000–1028, Oct. 2003. doi: 10.1046/j.1365-8711.2003.06897.x.

N. Byler, J. J. Dalcanton, C. Conroy, and B. D. Johnson. Nebular continuum and line emission in stellar population synthesis models. *The Astrophysical Journal*, 840(1):44, 2017.

L. Carigi and M. Peimbert. H II Regions and Protosolar Abundances in Galactic Chemical Evolution. *Revista Mexicana de Astronomía y Astrofísica*, 47:139–158, Apr. 2011.

G. Chabrier. Galactic Stellar and Substellar Initial Mass Function. *Publications of the Astronomical Society of the Pacific*, 115:763–795, July 2003. doi: 10.1086/376392.

S. Charlot and M. Longhetti. Nebular emission from star-forming galaxies. *Monthly Notices of the Royal Astronomical Society*, 323:887–903, May 2001. doi: 10.1046/j.1365-8711.2001.04260.x.

M. Chatzikos, G. J. Ferland, R. J. R. Williams, R. Porter, and P. A. M. van Hoof. Effects of External Radiation Fields on Line Emission - Application to Star-forming Regions. *The Astrophysical Journal*, 779:122, Dec. 2013. doi: 10.1088/0004-637X/779/2/122.

R. Cid Fernandes, A. Mateus, L. Sodré, G. Stasińska, and J. M. Gomes. Semi-empirical analysis of Sloan Digital Sky Survey galaxies - I. Spectral synthesis method. *Monthly Notices of the Royal Astronomical Society*, 358:363–378, Apr. 2005. doi: 10.1111/j.1365-2966.2005.08752.x.

C. Conroy. Modeling the Panchromatic Spectral Energy Distributions of Galaxies. *Annual Review of Astronomy & Astrophysics*, 51:393–455, Aug. 2013. doi: 10.1146/annurev-astro-082812-141017.

C. Conroy, J. E. Gunn, and M. White. The Propagation of Uncertainties in Stellar Population Synthesis Modeling. I. The Relevance of Uncertain Aspects of Stellar Evolution and the Initial Mass Function to the Derived Physical Properties of Galaxies. *The Astrophysical Journal*, 699: 486–506, July 2009. doi: 10.1088/0004-637X/699/1/486.

R. Cooke, M. Pettini, C. C. Steidel, G. C. Rudie, and P. E. Nissen. The most metal-poor damped Lyα systems: insights into chemical evolution in the very metal-poor regime. *Monthly Notices of the Royal Astronomical Society*, 417:1534–1558, Oct. 2011. doi: 10.1111/j.1365-2966.2011.19365.x.

R. Cooke, M. Pettini, and M. T. Murphy. A new candidate for probing Population III nucleosynthesis with carbon-enhanced damped Lyα systems. *Monthly Notices of the Royal Astronomical Society*, 425:347–354, Sept. 2012. doi: 10.1111/j.1365-2966.2012.21470.x.

R. J. Cooke and P. Madau. Carbon-enhanced Metal-poor Stars: Relics from the Dark Ages. *The Astrophysical Journal*, 791:116, Aug. 2014. doi: 10.1088/0004-637X/791/2/116.

P. A. Crowther, O. Schnurr, R. Hirschi, N. Yusof, R. J. Parker, S. P. Goodwin, and H. A. Kassim. The R136 star cluster hosts several stars whose individual masses greatly exceed the accepted 150M$_{solar}$ stellar mass limit. *Monthly Notices of the Royal Astronomical Society*, 408:731–751, Oct. 2010. doi: 10.1111/j.1365-2966.2010.17167.x.

J.-G. Cuby, O. Le Fèvre, H. McCracken, J.-C. Cuillandre, E. Magnier, and B. Meneux. Discovery of a z = 6.17 galaxy from CFHT and VLT observations. *Astronomy & Astrophysics*, 405:L19–L22, July 2003. doi: 10.1051/0004-6361:20030760.

K. Davidson. On photoionization analyses of emission spectra of quasars. *The Astrophysical Journal*, 218:20–32, Nov. 1977. doi: 10.1086/155653.

S. E. de Mink, N. Langer, R. G. Izzard, H. Sana, and A. de Koter. The Rotation Rates of Massive Stars: The Role of Binary Interaction through Tides, Mass Transfer, and Mergers. *The Astrophysical Journal*, 764:166, Feb. 2013. doi: 10.1088/0004-637X/764/2/166.

T. Di Matteo, N. Khandai, C. DeGraf, Y. Feng, R. A. C. Croft, J. Lopez, and V. Springel. Cold Flows and the First Quasars. *The Astrophysical Journal, Letters*, 745:L29, Feb. 2012. doi: 10.1088/2041-8205/745/2/L29.

R. J. Dufour, G. A. Shields, and R. J. Talbot, Jr. The carbon abundance in the Magellanic Clouds from IUE observations of H II regions. *The Astrophysical Journal*, 252:461–473, Jan. 1982. doi: 10.1086/159574.

A.-M. Dumont, A. Abrassart, and S. Collin. A code for optically thick and hot photoionized media. *Astronomy & Astrophysics*, 357:823–838, May 2000.

J. S. Dunlop, A. B. Rogers, R. J. McLure, R. S. Ellis, B. E. Robertson, A. Koekemoer, P. Dayal, E. Curtis-Lake, V. Wild, S. Charlot, R. A. A. Bowler, M. A. Schenker, M. Ouchi, Y. Ono, M. Cirasuolo, S. R. Furlanetto, D. P. Stark, T. A. Targett, and E. Schneider. The UV continua and inferred stellar populations of galaxies at z $\sim$ 7-9 revealed by the Hubble Ultra-Deep Field 2012 campaign. *Monthly Notices of the Royal Astronomical Society*, 432:3520–3533, July 2013. doi: 10.1093/mnras/stt702.

P. P. Eggleton. The evolution of low mass stars. *Monthly Notices of the Royal Astronomical Society*, 151:351, 1971. doi: 10.1093/mnras/151.3.351.

J. Eldridge and E. Stanway. Spectral population synthesis including massive binaries. *Monthly Notices of the Royal Astronomical Society*, 400:1019–1028, Dec. 2009. doi: 10.1111/j.1365-2966.2009.15514.x.

J. J. Eldridge and E. R. Stanway. The effect of stellar evolution uncertainties on the rest-frame ultraviolet stellar lines of C IV and He II in high-redshift Lyman-break galaxies. *Monthly Notices of the Royal Astronomical Society*, 419:479–489, Jan. 2012. doi: 10.1111/j.1365-2966.2011.19713.x.

J. J. Eldridge, R. G. Izzard, and C. A. Tout. The effect of massive binaries on stellar populations and supernova progenitors. *Monthly Notices of the Royal Astronomical Society*, 384:1109–1118, Mar. 2008. doi: 10.1111/j.1365-2966.2007.12738.x.

J. J. Eldridge, N. Langer, and C. A. Tout. Runaway stars as progenitors of supernovae and gamma-ray bursts. *Monthly Notices of the Royal Astronomical Society*, 414:3501–3520, July 2011. doi: 10.1111/j.1365-2966.2011.18650.x.

R. S. Ellis, R. J. McLure, J. S. Dunlop, B. E. Robertson, Y. Ono, M. A. Schenker, A. Koekemoer, R. A. A. Bowler, M. Ouchi, A. B. Rogers, E. Curtis-Lake, E. Schneider, S. Charlot, D. P. Stark, S. R. Furlanetto, and M. Cirasuolo. The Abundance of Star-forming Galaxies in the Redshift Range 8.5-12: New Results from the 2012 Hubble Ultra Deep Field Campaign. *The Astrophysical Journal, Letters*, 763:L7, Jan. 2013. doi: 10.1088/2041-8205/763/1/L7.

D. K. Erb, M. Pettini, A. E. Shapley, C. C. Steidel, D. R. Law, and N. A. Reddy. Physical Conditions in a Young, Unreddened, Low-metallicity Galaxy at High Redshift. *The Astrophysical Journal*, 719:1168–1190, Aug. 2010. doi: 10.1088/0004-637X/719/2/1168.

B. Ercolano, M. J. Barlow, P. J. Storey, and X.-W. Liu. MOCASSIN: a fully three-dimensional Monte Carlo photoionization code. *Monthly Notices of the Royal Astronomical Society*, 340: 1136–1152, Apr. 2003. doi: 10.1046/j.1365-8711.2003.06371.x.

C. Esteban, M. Peimbert, S. Torres-Peimbert, and M. Rodríguez. Optical Recombination Lines of Heavy Elements in Giant Extragalactic H II Regions. *The Astrophysical Journal*, 581:241–257, Dec. 2002. doi: 10.1086/344104.

C. Esteban, F. Bresolin, M. Peimbert, J. García-Rojas, A. Peimbert, and A. Mesa-Delgado. Keck HIRES Spectroscopy of Extragalactic H II Regions: C and O Abundances from Recombination Lines. *The Astrophysical Journal*, 700:654–678, July 2009. doi: 10.1088/0004-637X/700/1/654.

C. Esteban, J. García-Rojas, L. Carigi, M. Peimbert, F. Bresolin, A. R. López-Sánchez, and A. Mesa-Delgado. Carbon and oxygen abundances from recombination lines in low-metallicity star-forming galaxies. Implications for chemical evolution. *Monthly Notices of the Royal Astronomical Society*, 443:624–647, Sept. 2014. doi: 10.1093/mnras/stu1177.

D. Fabbian, P. E. Nissen, M. Asplund, M. Pettini, and C. Akerman. The C/O ratio at low metallicity: constraints on early chemical evolution from observations of Galactic halo stars. *A&A*, 500:1143–1155, June 2009. doi: 10.1051/0004-6361/200810095.

S. M. Faber. Quadratic programming applied to the problem of galaxy population synthesis. *Astronomy & Astrophysics*, 20:361–374, Sept. 1972.

X. Fan, C. L. Carilli, and B. Keating. Observational Constraints on Cosmic Reionization. *Annual Review of Astronomy & Astrophysics*, 44:415–462, Sept. 2006. doi: 10.1146/annurev.astro.44.051905.092514.

A. Feltre, S. Charlot, and J. Gutkin. Nuclear activity versus star formation: emission-line diagnostics at ultraviolet and optical wavelengths. *Monthly Notices of the Royal Astronomical Society*, 456:3354–3374, Mar. 2016. doi: 10.1093/mnras/stv2794.

G. J. Ferland, K. T. Korista, D. A. Verner, J. W. Ferguson, J. B. Kingdon, and E. M. Verner. CLOUDY 90: Numerical Simulation of Plasmas and Their Spectra. *Publications of the Astronomical Society of the Pacific*, 110:761–778, July 1998. doi: 10.1086/316190.

G. J. Ferland, R. Porter, P. van Hoof, R. Williams, N. Abel, M. Lykins, G. Shaw, W. Henney, and P. Stancil. The 2013 Release of Cloudy. *Revista Mexicana de Astronomía y Astrofísica*, 49:137–163, Apr. 2013.

G. B. Field, D. W. Goldsmith, and H. J. Habing. A Theoretical Model for the Interstellar Medium. In *Bulletin of the American Astronomical Society*, volume 1 of *Bulletin of the American Astronomical Society*, page 240, June 1969.

S. L. Finkelstein, C. Papovich, M. Dickinson, M. Song, V. Tilvi, A. M. Koekemoer, K. D. Finkelstein, B. Mobasher, H. C. Ferguson, M. Giavalisco, N. Reddy, M. L. N. Ashby, A. Dekel, G. G. Fazio, A. Fontana, N. A. Grogin, J.-S. Huang, D. Kocevski, M. Rafelski, B. J. Weiner, and S. P. Willner. A galaxy rapidly forming stars 700 million years after the Big Bang at redshift 7.51. *Nature*, 502:524–527, Oct. 2013. doi: 10.1038/nature12657.

M. Fioc and B. Rocca-Volmerange. PEGASE.2, a metallicity-consistent spectral evolution model of galaxies: the documentation and the code. *ArXiv Astrophysics e-prints*, Dec. 1999.

P. J. Francis, P. C. Hewett, C. B. Foltz, F. H. Chaffee, R. J. Weymann, and S. L. Morris. A high signal-to-noise ratio composite quasar spectrum. *The Astrophysical Journal*, 373:465–470, June 1991. doi: 10.1086/170066.

J. García-Rojas and C. Esteban. On the Abundance Discrepancy Problem in H II Regions. *The Astrophysical Journal*, 670:457–470, Nov. 2007. doi: 10.1086/521871.

D. R. Garnett, E. D. Skillman, R. J. Dufour, M. Peimbert, S. Torres-Peimbert, R. Terlevich, E. Terlevich, and G. A. Shields. The evolution of C/O in dwarf galaxies from Hubble Space Telescope FOS observations. *The Astrophysical Journal*, 443:64–76, Apr. 1995. doi: 10.1086/175503.

J. E. Geach, I. Smail, P. N. Best, J. Kurk, M. Casali, R. J. Ivison, and K. Coppin. HiZELS: a high-redshift survey of Hα emitters - I. The cosmic star formation rate and clustering at z = 2.23. *Monthly Notices of the Royal Astronomical Society*, 388:1473–1486, Aug. 2008. doi: 10.1111/j.1365-2966.2008.13481.x.

M. Giavalisco. Lyman-Break Galaxies. *Annual Review of Astronomy & Astrophysics*, 40:579–641, 2002. doi: 10.1146/annurev.astro.40.121301.111837.

S. C. O. Glover. The Chemistry of the Early Universe. In J. Cernicharo and R. Bachiller, editors, *The Molecular Universe*, volume 280 of *IAU Symposium*, pages 313–324, Dec. 2011. doi: 10.1017/S1743921311025075.

J. M. Gomes and P. Papaderos. Fitting Analysis using Differential Evolution Optimization (FADO): Spectral population synthesis through genetic optimization under self-consistency boundary conditions. *ArXiv e-prints*, Apr. 2017.

B. A. Groves, M. A. Dopita, and R. S. Sutherland. Dusty, Radiation Pressure-Dominated Photoionization. I. Model Description, Structure, and Grids. *The Astrophysical Journal, Supplement*, 153: 9–73, July 2004. doi: 10.1086/421113.

B. A. Groves, T. M. Heckman, and G. Kauffmann. Emission-line diagnostics of low-metallicity active galactic nuclei. *Monthly Notices of the Royal Astronomical Society*, 371:1559–1569, Oct. 2006. doi: 10.1111/j.1365-2966.2006.10812.x.

B. Gustafsson, T. Karlsson, E. Olsson, B. Edvardsson, and N. Ryde. The origin of carbon, investigated by spectral analysis of solar-type stars in the Galactic Disk. *Astronomy & Astrophysics*, 342:426–439, Feb. 1999.

J. Gutkin, S. Charlot, and G. Bruzual. Modelling the nebular emission from primeval to present-day star-forming galaxies. *Monthly Notices of the Royal Astronomical Society*, 462:1757–1774, Oct. 2016. doi: 10.1093/mnras/stw1716.

F. Haardt and P. Madau. Radiative Transfer in a Clumpy Universe. II. The Ultraviolet Extragalactic Background. *The Astrophysical Journal*, 461:20, Apr. 1996. doi: 10.1086/177035.

F. Haardt and L. Maraschi. X-ray spectra from two-phase accretion disks. *The Astrophysical Journal*, 413:507–517, Aug. 1993. doi: 10.1086/173020.

J. P. Harrington. Ionization Stratification and Thermal Stability in Model Planetary Nebulae. *The Astrophysical Journal*, 152:943, June 1968. doi: 10.1086/149608.

C. M. Harrison. *Observational constraints on the influence of active galactic nuclei on the evolution of galaxies*. Springer, 2016.

M. Hayes. Lyman Alpha Emitting Galaxies in the Nearby Universe. *Publications of the Astronomical Society of Australia*, 32:e027, July 2015. doi: 10.1017/pasa.2015.25.

A. Heger and S. E. Woosley. The Nucleosynthetic Signature of Population III. *The Astrophysical Journal*, 567:532–543, Mar. 2002. doi: 10.1086/338487.

R. B. C. Henry, M. G. Edmunds, and J. Köppen. On the Cosmic Origins of Carbon and Nitrogen. *The Astrophysical Journal*, 541:660–674, Oct. 2000a. doi: 10.1086/309471.

R. B. C. Henry, K. B. Kwitter, and J. A. Bates. A New Look at Carbon Abundances in Planetary Nebulae. IV. Implications for Stellar Nucleosynthesis. *The Astrophysical Journal*, 531:928–941, Mar. 2000b. doi: 10.1086/308509.

B. P. Holden, P. A. Oesch, V. G. González, G. D. Illingworth, I. Labbé, R. Bouwens, M. Franx, P. van Dokkum, and L. Spitler. Rest-frame Optical Emission Lines in z $\sim$ 3.5 Lyman-break-selected Galaxies: The Ubiquity of Unusually High [OIII]/Hβ Ratios at 2 Gyr. *The Astrophysical Journal*, 820:73, Mar. 2016. doi: 10.3847/0004-637X/820/1/73.

E. M. Hu, L. L. Cowie, A. Songaila, A. J. Barger, B. Rosenwasser, and I. G. B. Wold. An Ultraluminous Lyα Emitter with a Blue Wing at z = 6.6. *The Astrophysical Journal, Letters*, 825:L7, July 2016. doi: 10.3847/2041-8205/825/1/L7.

K.-H. Huang, M. Bradač, B. C. Lemaux, R. E. Ryan, Jr., A. Hoag, M. Castellano, R. Amorín, A. Fontana, G. B. Brammer, B. Cain, L. M. Lubin, E. Merlin, K. B. Schmidt, T. Schrabback, T. Treu, A. H. Gonzalez, A. von der Linden, and R. I. Knight. Spitzer UltRa Faint SUrvey Program (SURFS UP). II. IRAC-detected Lyman-Break Galaxies at 6 $\leq$ z $\leq$ 10 behind Strong-lensing Clusters. *The Astrophysical Journal*, 817:11, Jan. 2016. doi: 10.3847/0004-637X/817/1/11.

E. Hubble. A Relation between Distance and Radial Velocity among Extra-Galactic Nebulae. *Proceedings of the National Academy of Science*, 15:168–173, Mar. 1929. doi: 10.1073/pnas.15.3.168.

L. K. Hunt and H. Hirashita. The size-density relation of extragalactic H II regions. *Astronomy & Astrophysics*, 507:1327–1343, Dec. 2009. doi: 10.1051/0004-6361/200912020.

M. Iye, K. Ota, N. Kashikawa, H. Furusawa, T. Hashimoto, T. Hattori, Y. Matsuda, T. Morokuma, M. Ouchi, and K. Shimasaku. A galaxy at a redshift z = 6.96. *Nature*, 443:186–188, Sept. 2006. doi: 10.1038/nature05104.

Y. I. Izotov and T. X. Thuan. Heavy-Element Abundances in Blue Compact Galaxies. *The Astrophysical Journal*, 511:639–659, Feb. 1999. doi: 10.1086/306708.

Y. I. Izotov, T. X. Thuan, and N. G. Guseva. Hunting for extremely metal-poor emission-line galaxies in the Sloan Digital Sky Survey: MMT and 3.5 m APO observations. *Astronomy & Astrophysics*, 546:A122, Oct. 2012. doi: 10.1051/0004-6361/201219733.

Y. I. Izotov, I. Orlitová, D. Schaerer, T. X. Thuan, A. Verhamme, N. G. Guseva, and G. Worseck. Eight per cent leakage of Lyman continuum photons from a compact, star-forming dwarf galaxy. *Nature*, 529:178–180, Jan. 2016. doi: 10.1038/nature16456.

B. L. James, S. Koposov, D. P. Stark, V. Belokurov, M. Pettini, and E. W. Olszewski. Uncovering blue diffuse dwarf galaxies. *Monthly Notices of the Royal Astronomical Society*, 448:2687–2703, Apr. 2015. doi: 10.1093/mnras/stv175.

A. E. Jaskot and S. Ravindranath. Photoionization Models for the Semi-forbidden C III] 1909 Emission in Star-forming Galaxies. *The Astrophysical Journal*, 833:136, Dec. 2016. doi: 10.3847/1538-4357/833/2/136.

J. L. Johnson. Formation of the First Galaxies: Theory and Simulations. In T. Wiklind, B. Mobasher, and V. Bromm, editors, *The First Galaxies*, volume 396 of *Astrophysics and Space Science Library*, page 177, 2013. doi: 10.1007/978-3-642-32362-1_4.

T. Kallman. XSTAR: A program for calculating conditions and spectra of photoionized gases. Astrophysics Source Code Library, Oct. 1999.

N. Kashikawa, T. Nagao, J. Toshikawa, Y. Ishizaki, E. Egami, M. Hayashi, C. Ly, M. A. Malkan, Y. Matsuda, K. Shimasaku, M. Iye, K. Ota, T. Shibuya, L. Jiang, Y. Taniguchi, and Y. Shioya. A Lyα Emitter with an Extremely Large Rest-frame Equivalent Width of $\sim$ 900 Å at z = 6.5: A Candidate Population III-dominated Galaxy? *The Astrophysical Journal*, 761:85, Dec. 2012. doi: 10.1088/0004-637X/761/2/85.

G. Kauffmann, T. M. Heckman, C. Tremonti, J. Brinchmann, S. Charlot, S. D. M. White, S. E. Ridgway, J. Brinkmann, M. Fukugita, P. B. Hall, Ž. Ivezić, G. T. Richards, and D. P. Schneider. The host galaxies of active galactic nuclei. *Monthly Notices of the Royal Astronomical Society*, 346:1055–1077, Dec. 2003. doi: 10.1111/j.1365-2966.2003.07154.x.

R. C. Kennicutt, Jr., F. Bresolin, and D. R. Garnett. The Composition Gradient in M101 Revisited. II. Electron Temperatures and Implications for the Nebular Abundance Scale. *The Astrophysical Journal*, 591:801–820, July 2003. doi: 10.1086/375398.

L. J. Kewley, M. A. Dopita, R. S. Sutherland, C. A. Heisler, and J. Trevena. Theoretical Modeling of Starburst Galaxies. *The Astrophysical Journal*, 556:121–140, July 2001. doi: 10.1086/321545.

L. J. Kewley, M. A. Dopita, C. Leitherer, R. Davé, T. Yuan, M. Allen, B. Groves, and R. Sutherland. Theoretical Evolution of Optical Strong Lines across Cosmic Time. *The Astrophysical Journal*, 774:100, Sept. 2013. doi: 10.1088/0004-637X/774/2/100.

Y. Kim, M. Im, Y. Jeon, M. Kim, C. Choi, J. Hong, M. Hyun, H. D. Jun, M. Karouzos, D. Kim, D. Kim, J.-W. Kim, J. H. Kim, S.-K. Lee, S. Pak, W.-K. Park, Y. C. Taak, and Y. Yoon. Discovery

of a Faint Quasar at z $\sim$ 6 and Implications for Cosmic Reionization. *The Astrophysical Journal, Letters*, 813:L35, Nov. 2015. doi: 10.1088/2041-8205/813/2/L35.

A. Konno, M. Ouchi, Y. Ono, K. Shimasaku, T. Shibuya, H. Furusawa, K. Nakajima, Y. Naito, R. Momose, S. Yuma, and M. Iye. Accelerated Evolution of the Lyα Luminosity Function at z $\geq$ 7 Revealed by the Subaru Ultra-deep Survey for Lyα Emitters at z = 7.3. *The Astrophysical Journal*, 797:16, Dec. 2014. doi: 10.1088/0004-637X/797/1/16.

C. M. Kurt, R. J. Dufour, D. R. Garnett, E. D. Skillman, J. S. Mathis, M. Peimbert, S. Torres-Peimbert, and M.-T. Ruiz. Hubble Space Telescope Observations of the Dusty Small Magellanic Cloud H II Region N88A. *The Astrophysical Journal*, 518:246–261, June 1999. doi: 10.1086/307271.

P. Laursen, J. Sommer-Larsen, and A. O. Razoumov. Intergalactic Transmission and Its Impact on the Lyα Line. *The Astrophysical Journal*, 728:52, Feb. 2011. doi: 10.1088/0004-637X/728/1/52.

N. Leite, C. Evoli, M. D'Angelo, B. Ciardi, G. Sigl, and A. Ferrara. Do cosmic rays heat the early intergalactic medium? *Monthly Notices of the Royal Astronomical Society*, 469:416–424, July 2017. doi: 10.1093/mnras/stx805.

C. Leitherer, D. Schaerer, J. D. Goldader, R. M. G. Delgado, C. Robert, D. F. Kune, D. F. de Mello, D. Devost, and T. M. Heckman. Starburst99: Synthesis Models for Galaxies with Active Star Formation. *The Astrophysical Journal, Supplement*, 123:3–40, July 1999. doi: 10.1086/313233.

E. Levesque, L. Kewley, and K. Larson. Theoretical Modeling of Star-Forming Galaxies. I. Emission-Line Diagnostic Grids for Local and Low-Metallicity Galaxies. *The Astronomical Journal*, 139:712–727, Feb. 2010. doi: 10.1088/0004-6256/139/2/712.

S. N. Longmore, J. M. D. Kruijssen, N. Bastian, J. Bally, J. Rathborne, L. Testi, A. Stolte, J. Dale, E. Bressert, and J. Alves. The Formation and Early Evolution of Young Massive Clusters. *Protostars and Planets VI*, pages 291–314, 2014. doi: 10.2458/azu_uapress_9780816531240-ch013.

Á. R. López-Sánchez, C. Esteban, J. García-Rojas, M. Peimbert, and M. Rodríguez. The Localized Chemical Pollution in NGC 5253 Revisited: Results from Deep Echelle Spectrophotometry. *The Astrophysical Journal*, 656:168–185, Feb. 2007. doi: 10.1086/510112.

E. Lusso, G. Worseck, J. F. Hennawi, J. X. Prochaska, C. Vignali, J. Stern, and J. M. O'Meara. The first ultraviolet quasar-stacked spectrum at z $\simeq$ 2.4 from WFC3. *Monthly Notices of the Royal Astronomical Society*, 449:4204–4220, June 2015. doi: 10.1093/mnras/stv516.

X. Ma, P. F. Hopkins, D. Kasen, E. Quataert, C.-A. Faucher-Giguère, D. Kereš, N. Murray, and A. Strom. Binary stars can provide the 'missing photons' needed for reionization. *Monthly Notices of the Royal Astronomical Society*, 459:3614–3619, July 2016. doi: 10.1093/mnras/stw941.

A. Maeder and G. Meynet. Stellar evolution with rotation and magnetic fields. I. The relative importance of rotational and magnetic effects. *Astronomy & Astrophysics*, 411:543–552, Dec. 2003. doi: 10.1051/0004-6361:20031491.

R. Mainali, J. A. Kollmeier, D. P. Stark, R. A. Simcoe, G. Walth, A. B. Newman, and D. R. Miller. Evidence for a Hard Ionizing Spectrum from a z = 6.11 Stellar Population. *The Astrophysical Journal, Letters*, 836:L14, Feb. 2017. doi: 10.3847/2041-8213/836/1/L14.

C. Maraston. Evolutionary synthesis of stellar populations: a modular tool. *Monthly Notices of the Royal Astronomical Society*, 300:872–892, Nov. 1998. doi: 10.1046/j.1365-8711.1998.01947.x.

D. Masters, P. Capak, M. Salvato, F. Civano, B. Mobasher, B. Siana, G. Hasinger, C. D. Impey, T. Nagao, J. R. Trump, H. Ikeda, M. Elvis, and N. Scoville. Evolution of the Quasar Luminosity Function over $3 < z < 5$ in the COSMOS Survey Field. *The Astrophysical Journal*, 755:169, Aug. 2012. doi: 10.1088/0004-637X/755/2/169.

D. Masters, P. McCarthy, B. Siana, M. Malkan, B. Mobasher, H. Atek, A. Henry, C. L. Martin, M. Rafelski, N. P. Hathi, C. Scarlata, N. R. Ross, A. J. Bunker, G. Blanc, A. G. Bedregal, A. Domínguez, J. Colbert, H. Teplitz, and A. Dressler. Physical Properties of Emission-line Galaxies at $z \sim 2$ from Near-infrared Spectroscopy with Magellan FIRE. *The Astrophysical Journal*, 785:153, Apr. 2014. doi: 10.1088/0004-637X/785/2/153.

J. Matthee, D. Sobral, S. Santos, H. Röttgering, B. Darvish, and B. Mobasher. Identification of the brightest Lyα emitters at z = 6.6: implications for the evolution of the luminosity function in the reionization era. *Monthly Notices of the Royal Astronomical Society*, 451:400–417, July 2015. doi: 10.1093/mnras/stv947.

J. Matthee, D. Sobral, B. Darvish, S. Santos, B. Mobasher, A. Paulino-Afonso, H. Röttgering, and L. Alegre. Spectroscopic properties of luminous Lyman-α emitters at $z \approx 6 - 7$ and comparison to the Lyman-break population. *ArXiv e-prints*, June 2017.

C. F. McKee and J. P. Ostriker. A theory of the interstellar medium - Three components regulated by supernova explosions in an inhomogeneous substrate. *The Astrophysical Journal*, 218:148–169, Nov. 1977. doi: 10.1086/155667.

M. Mollá, M. L. García-Vargas, and A. Bressan. PopStar I: evolutionary synthesis model description. *Monthly Notices of the Royal Astronomical Society*, 398:451–470, Sept. 2009. doi: 10.1111/j.1365-2966.2009.15160.x.

M. Mollá, O. Cavichia, M. Gavilán, and B. K. Gibson. Galactic chemical evolution: stellar yields and the initial mass function. *Monthly Notices of the Royal Astronomical Society*, 451:3693–3708, Aug. 2015. doi: 10.1093/mnras/stv1102.

C. Morisset. Cloudy_3D, a new pseudo-3D photoionization code. In M. J. Barlow and R. H. Méndez, editors, *Planetary Nebulae in our Galaxy and Beyond*, volume 234 of *IAU Symposium*, pages 467–468, 2006. doi: 10.1017/S1743921306003772.

C. Morisset. pyCloudy: Tools to manage astronomical Cloudy photoionization code. Astrophysics Source Code Library, Apr. 2013.

C. Morisset, G. Delgado-Inglada, and N. Flores-Fajardo. A virtual observatory for photoionized nebulae: the Mexican Million Models database (3MdB). *Revista Mexicana de Astronomía y Astrofísica*, 51:103–120, Apr. 2015.

D. J. Mortlock, S. J. Warren, B. P. Venemans, M. Patel, P. C. Hewett, R. G. McMahon, C. Simpson, T. Theuns, E. A. Gonzáles-Solares, A. Adamson, S. Dye, N. C. Hambly, P. Hirst, M. J. Irwin, E. Kuiper, A. Lawrence, and H. J. A. Röttgering. A luminous quasar at a redshift of z = 7.085. *Nature*, 474:616–619, June 2011. doi: 10.1038/nature10159.

M. Mouhcine and T. Contini. Chemical evolution of starburst galaxies: How does star formation proceed? *Astronomy & Astrophysics*, 389:106–114, July 2002. doi: 10.1051/0004-6361:20020592.

E. Moy, B. Rocca-Volmerange, and M. Fioc. Evolution of photoionization and star formation in starbursts and H1214 II galaxies. *A&A*, 365(3):347–359, 2001. doi: 10.1051/0004-6361:20000045.

K. Nakajima, R. Ellis, I. Iwata, A. Inoue, H. Kusakabe, M. Ouchi, and B. Robertson. A Hard Ionizing Spectrum in z = 3-4 Lyα Emitters with Intense [O III] Emission: Analogs of Galaxies in the Reionization Era? *The Astrophysical Journal, Letters*, 831:L9, Nov. 2016. doi: 10.3847/2041-8205/831/1/L9.

M.-F. Nieva and N. Przybilla. Present-day cosmic abundances. A comprehensive study of nearby early B-type stars and implications for stellar and Galactic evolution and interstellar dust models. *Astronomy & Astrophysics*, 539:A143, Mar. 2012. doi: 10.1051/0004-6361/201118158.

P. A. Oesch, P. G. van Dokkum, G. D. Illingworth, R. J. Bouwens, I. Momcheva, B. Holden, G. W. Roberts-Borsani, R. Smit, M. Franx, I. Labbé, V. González, and D. Magee. A Spectroscopic Redshift Measurement for a Luminous Lyman Break Galaxy at z = 7.730 Using Keck/MOSFIRE. *The Astrophysical Journal, Letters*, 804:L30, May 2015. doi: 10.1088/2041-8205/804/2/L30.

Y. Ono, M. Ouchi, B. Mobasher, M. Dickinson, K. Penner, K. Shimasaku, B. J. Weiner, J. S. Kartaltepe, K. Nakajima, H. Nayyeri, D. Stern, N. Kashikawa, and H. Spinrad. Spectroscopic Confirmation of Three z-dropout Galaxies at z = 6.844-7.213: Demographics of Lyα Emission in z $\sim$ 7 Galaxies. *The Astrophysical Journal*, 744:83, Jan. 2012. doi: 10.1088/0004-637X/744/2/83.

D. E. Osterbrock and G. J. Ferland. *Astrophysics of gaseous nebulae and active galactic nuclei.* 2006.

J. P. Ostriker and P. J. Steinhardt. Cosmic Concordance. *ArXiv Astrophysics e-prints*, May 1995.

M. Ouchi, T. Hamana, K. Shimasaku, T. Yamada, M. Akiyama, N. Kashikawa, M. Yoshida, K. Aoki, M. Iye, T. Saito, T. Sasaki, C. Simpson, and M. Yoshida. Definitive Identification of the Transition between Small-and Large-Scale Clustering for Lyman Break Galaxies. *The Astrophysical Journal, Letters*, 635:L117–L120, Dec. 2005. doi: 10.1086/499519.

M. Ouchi, Y. Ono, E. Egami, T. Saito, M. Oguri, P. J. McCarthy, D. Farrah, N. Kashikawa, I. Momcheva, K. Shimasaku, K. Nakanishi, H. Furusawa, M. Akiyama, J. S. Dunlop, A. M. J. Mortier, S. Okamura, M. Hayashi, M. Cirasuolo, A. Dressler, M. Iye, M. J. Jarvis, T. Kodama,

C. L. Martin, R. J. McLure, K. Ohta, T. Yamada, and M. Yoshida. Discovery of a Giant Lyα Emitter Near the Reionization Epoch. *The Astrophysical Journal*, 696:1164–1175, May 2009. doi: 10.1088/0004-637X/696/2/1164.

A. Pallottini, A. Ferrara, S. Gallerani, S. Salvadori, and V. D'Odorico. Simulating cosmic metal enrichment by the first galaxies. *Monthly Notices of the Royal Astronomical Society*, 440:2498–2518, May 2014. doi: 10.1093/mnras/stu451.

S. Parsa, J. S. Dunlop, and R. J. McLure. No evidence for a significant AGN contribution to cosmic hydrogen reionization. *ArXiv e-prints*, Apr. 2017.

A. A. Penzias and R. W. Wilson. A Measurement of Excess Antenna Temperature at 4080 Mc/s. *The Astrophysical Journal*, 142:419–421, July 1965. doi: 10.1086/148307.

E. Pérez-Montero. Deriving model-based T_e-consistent chemical abundances in ionized gaseous nebulae. *Monthly Notices of the Royal Astronomical Society*, 441:2663–2675, July 2014. doi: 10.1093/mnras/stu753.

E. Pérez-Montero and R. Amorín. Using photo-ionisation models to derive carbon and oxygen gas-phase abundances in the rest UV. *Monthly Notices of the Royal Astronomical Society*, 467: 1287–1293, May 2017. doi: 10.1093/mnras/stx186.

M. Pettini, B. J. Zych, C. C. Steidel, and F. H. Chaffee. C, N, O abundances in the most metal-poor damped Lyman-α systems. *Monthly Notices of the Royal Astronomical Society*, 385:2011–2024, Apr. 2008. doi: 10.1111/j.1365-2966.2008.12951.x.

L. S. Pilyugin and T. X. Thuan. Oxygen Abundance Determination in H II Regions: The Strong Line Intensities-Abundance Calibration Revisited. *The Astrophysical Journal*, 631:231–243, Sept. 2005. doi: 10.1086/432408.

Planck Collaboration, P. A. R. Ade, N. Aghanim, M. Arnaud, M. Ashdown, J. Aumont, C. Baccigalupi, A. J. Banday, R. B. Barreiro, J. G. Bartlett, and et al. Planck 2015 results. XIII. Cosmological parameters. *A&A*, 594:A13, Sept. 2016. doi: 10.1051/0004-6361/201525830.

M. J. Rees, H. Netzer, and G. J. Ferland. Small dense broad-line regions in active nuclei. *The Astrophysical Journal*, 347:640–655, Dec. 1989. doi: 10.1086/168155.

J. Richard, J.-P. Kneib, H. Ebeling, D. P. Stark, E. Egami, and A. K. Fiedler. Discovery of a possibly old galaxy at z= 6.027, multiply imaged by the massive cluster Abell 383. *Monthly Notices of the Royal Astronomical Society*, 414:L31–L35, June 2011. doi: 10.1111/j.1745-3933.2011.01050.x.

A. G. Riess, A. V. Filippenko, P. Challis, A. Clocchiatti, A. Diercks, P. M. Garnavich, R. L. Gilliland, C. J. Hogan, S. Jha, R. P. Kirshner, B. Leibundgut, M. M. Phillips, D. Reiss, B. P. Schmidt, R. A. Schommer, R. C. Smith, J. Spyromilio, C. Stubbs, N. B. Suntzeff, and J. Tonry. Observational Evidence from Supernovae for an Accelerating Universe and a Cosmological Constant. *The Astronomical Journal*, 116:1009–1038, Sept. 1998. doi: 10.1086/300499.

J. R. Rigby and G. H. Rieke. Missing Massive Stars in Starbursts: Stellar Temperature Diagnostics and the Initial Mass Function. *The Astrophysical Journal*, 606:237–257, May 2004. doi: 10.1086/382776.

B. E. Robertson, R. S. Ellis, S. R. Furlanetto, and J. S. Dunlop. Cosmic Reionization and Early Star-forming Galaxies: A Joint Analysis of New Constraints from Planck and the Hubble Space Telescope. *The Astrophysical Journal, Letters*, 802:L19, Apr. 2015. doi: 10.1088/2041-8205/802/2/L19.

E. Rollinde, E. Vangioni, and K. A. Olive. Population III Generated Cosmic Rays and the Production of ^{6}Li. *The Astrophysical Journal*, 651:658–666, Nov. 2006. doi: 10.1086/507580.

G. B. Rybicki and A. P. Lightman. *Radiative processes in astrophysics*. 1979.

E. E. Salpeter. The Luminosity Function and Stellar Evolution. *The Astrophysical Journal*, 121:161, Jan. 1955. doi: 10.1086/145971.

D. B. Sanders, E. S. Phinney, G. Neugebauer, B. T. Soifer, and K. Matthews. Continuum energy distribution of quasars - Shapes and origins. *The Astrophysical Journal*, 347:29–51, Dec. 1989. doi: 10.1086/168094.

S. Santos, D. Sobral, and J. Matthee. The Lyα luminosity function at z = 5.7 - 6.6 and the steep drop of the faint end: implications for reionization. *Monthly Notices of the Royal Astronomical Society*, 463:1678–1691, Dec. 2016. doi: 10.1093/mnras/stw2076.

D. Schaerer and S. de Barros. The impact of nebular emission on the ages of z≈6 galaxies. *Astronomy & Astrophysics*, 502:423–426, Aug. 2009. doi: 10.1051/0004-6361/200911781.

K. B. Schmidt, T. Treu, M. Bradač, B. Vulcani, K.-H. Huang, A. Hoag, M. Maseda, L. Guaita, L. Pentericci, G. B. Brammer, M. Dijkstra, A. Dressler, A. Fontana, A. L. Henry, T. A. Jones, C. Mason, M. Trenti, and X. Wang. The Grism Lens-Amplified Survey from Space (GLASS). III. A Census of Lyα Emission at z $\geq$ 7 from HST Spectroscopy. *The Astrophysical Journal*, 818:38, Feb. 2016. doi: 10.3847/0004-637X/818/1/38.

K. B. Schmidt, K.-H. Huang, T. Treu, A. Hoag, M. Bradač, A. L. Henry, T. A. Jones, C. Mason, M. Malkan, T. Morishita, L. Pentericci, M. Trenti, B. Vulcani, and X. Wang. The Grism Lens-Amplified Survey from Space (GLASS). XI. Detection of C IV in Multiple Images of the z = 6.11 Lyα Emitter behind RXC J2248.7-4431. *The Astrophysical Journal*, 839:17, Apr. 2017. doi: 10.3847/1538-4357/aa68a3.

R. Schneider, A. Ferrara, P. Natarajan, and K. Omukai. First Stars, Very Massive Black Holes, and Metals. *The Astrophysical Journal*, 571:30–39, May 2002. doi: 10.1086/339917.

Z. Shang, M. S. Brotherton, R. F. Green, G. A. Kriss, J. Scott, J. K. Quijano, O. Blaes, I. Hubeny, J. Hutchings, M. E. Kaiser, A. Koratkar, W. Oegerle, and W. Zheng. Quasars and the Big Blue Bump. *The Astrophysical Journal*, 619:41–59, Jan. 2005. doi: 10.1086/426134.

A. E. Shapley, C. C. Steidel, M. Pettini, and K. L. Adelberger. Rest-Frame Ultraviolet Spectra of z∼3 Lyman Break Galaxies. *The Astrophysical Journal*, 588:65–89, May 2003. doi: 10.1086/373922.

A. E. Shapley, A. L. Coil, C.-P. Ma, and K. Bundy. Chemical Abundances of DEEP2 Star-forming Galaxies at z∼1.0-1.5. *The Astrophysical Journal*, 635:1006–1021, Dec. 2005. doi: 10.1086/497630.

A. E. Shapley, N. A. Reddy, M. Kriek, W. R. Freeman, R. L. Sanders, B. Siana, A. L. Coil, B. Mobasher, I. Shivaei, S. H. Price, and L. de Groot. The MOSDEF Survey: Excitation Properties of z $\sim$ 2.3 Star-forming Galaxies. *The Astrophysical Journal*, 801:88, Mar. 2015. doi: 10.1088/0004-637X/801/2/88.

G. Shaw, G. J. Ferland, N. P. Abel, P. C. Stancil, and P. A. M. van Hoof. Molecular Hydrogen in Star-forming Regions: Implementation of its Microphysics in CLOUDY. *The Astrophysical Journal*, 624:794–807, May 2005. doi: 10.1086/429215.

T. Shibuya, M. Ouchi, Y. Harikane, M. Rauch, Y. Ono, S. Mukae, R. Higuchi, T. Kojima, S. Yuma, C.-H. Lee, H. Furusawa, A. Konno, C. L. Martin, K. Shimasaku, Y. Taniguchi, M. A. R. Kobayashi, M. Kajisawa, T. Nagao, T. Goto, N. Kashikawa, Y. Komiyama, H. Kusakabe, R. Momose, K. Nakajima, M. Tanaka, and S.-Y. Wang. SILVERRUSH. III. Deep Optical and Near-Infrared Spectroscopy for Lyα and UV-Nebular Lines of Bright Lya Emitters at z=6-7. *ArXiv e-prints*, May 2017.

G. A. Shields. Thermal continuum from acretion disks in quasars. *Nature*, 272:706–708, Apr. 1978. doi: 10.1038/272706a0.

K. Shimasaku, N. Kashikawa, M. Doi, C. Ly, M. A. Malkan, Y. Matsuda, M. Ouchi, T. Hayashino, M. Iye, K. Motohara, T. Murayama, T. Nagao, K. Ohta, S. Okamura, T. Sasaki, Y. Shioya, and Y. Taniguchi. Lyα Emitters at z = 5.7 in the Subaru Deep Field. *Publications of the Astronomical Society of Japan*, 58:313–334, Apr. 2006. doi: 10.1093/pasj/58.2.313.

J. M. Shull, M. Stevans, and C. W. Danforth. HST-COS Observations of AGNs. I. Ultraviolet Composite Spectra of the Ionizing Continuum and Emission Lines. *The Astrophysical Journal*, 752:162, June 2012. doi: 10.1088/0004-637X/752/2/162.

R. Smit, R. J. Bouwens, M. Franx, P. A. Oesch, M. L. N. Ashby, S. P. Willner, I. Labbé, B. Holwerda, G. G. Fazio, and J.-S. Huang. High-precision Photometric Redshifts from Spitzer/IRAC: Extreme [3.6] - [4.5] Colors Identify Galaxies in the Redshift Range z $\sim$ 6.6 - 6.9. *The Astrophysical Journal*, 801:122, Mar. 2015. doi: 10.1088/0004-637X/801/2/122.

D. Sobral, P. N. Best, Y. Matsuda, I. Smail, J. E. Geach, and M. Cirasuolo. Star formation at z=1.47 from HiZELS: an Hα+[O II] double-blind study. *Monthly Notices of the Royal Astronomical Society*, 420:1926–1945, Mar. 2012. doi: 10.1111/j.1365-2966.2011.19977.x.

D. Sobral, P. N. Best, I. Smail, B. Mobasher, J. Stott, and D. Nisbet. The stellar mass function of star-forming galaxies and the mass-dependent SFR function since z = 2.23 from HiZELS.

Monthly Notices of the Royal Astronomical Society, 437:3516–3528, Feb. 2014. doi: 10.1093/mnras/stt2159.

D. Sobral, J. Matthee, B. Darvish, D. Schaerer, B. Mobasher, H. J. A. Röttgering, S. Santos, and S. Hemmati. Evidence for PopIII-like Stellar Populations in the Most Luminous Lyman-α Emitters at the Epoch of Reionization: Spectroscopic Confirmation. *The Astrophysical Journal*, 808:139, Aug. 2015. doi: 10.1088/0004-637X/808/2/139.

D. Sobral, J. Matthee, P. Best, A. Stroe, H. Röttgering, I. Oteo, I. Smail, L. Morabito, and A. Paulino-Afonso. The CALYMHA survey: Lyα luminosity function and global escape fraction of Lyα photons at z = 2.23. *Monthly Notices of the Royal Astronomical Society*, 466:1242–1258, Apr. 2017. doi: 10.1093/mnras/stw3090.

M. Spite, R. Cayrel, B. Plez, V. Hill, F. Spite, E. Depagne, P. François, P. Bonifacio, B. Barbuy, T. Beers, J. Andersen, P. Molaro, B. Nordström, and F. Primas. First stars VI - Abundances of C, N, O, Li, and mixing in extremely metal-poor giants. Galactic evolution of the light elements. *Astronomy & Astrophysics*, 430:655–668, Feb. 2005. doi: 10.1051/0004-6361:20041274.

E. R. Stanway. What can distant galaxies teach us about massive stars? *ArXiv e-prints*, Feb. 2017.

E. R. Stanway, J. J. Eldridge, S. M. L. Greis, L. J. M. Davies, S. M. Wilkins, and M. N. Bremer. Interpreting high [O III]/H β ratios with maturing starbursts. *Monthly Notices of the Royal Astronomical Society*, 444:3466–3472, Nov. 2014. doi: 10.1093/mnras/stu1682.

E. R. Stanway, J. J. Eldridge, and G. D. Becker. Stellar population effects on the inferred photon density at reionization. *Monthly Notices of the Royal Astronomical Society*, 456(1):485, 2016. doi: 10.1093/mnras/stv2661.

D. P. Stark, M. A. Schenker, R. Ellis, B. Robertson, R. McLure, and J. Dunlop. Keck Spectroscopy of $3 \leq z \leq 7$ Faint Lyman Break Galaxies: The Importance of Nebular Emission in Understanding the Specific Star Formation Rate and Stellar Mass Density. *The Astrophysical Journal*, 763:129, Feb. 2013. doi: 10.1088/0004-637X/763/2/129.

D. P. Stark, J. Richard, B. Siana, S. Charlot, W. R. Freeman, J. Gutkin, A. Wofford, B. Robertson, R. Amanullah, D. Watson, and B. Milvang-Jensen. Ultraviolet emission lines in young low-mass galaxies at $z \sim 2$: physical properties and implications for studies at $z \geq 7$. *Monthly Notices of the Royal Astronomical Society*, 445:3200–3220, Dec. 2014. doi: 10.1093/mnras/stu1618.

D. P. Stark, G. Walth, S. Charlot, B. Clément, A. Feltre, J. Gutkin, J. Richard, R. Mainali, B. Robertson, B. Siana, et al. Spectroscopic detection of C IV λ1548 in a galaxy at z= 7.045: Implications for the ionizing spectra of reionization-era galaxies. *Monthly Notices of the Royal Astronomical Society*, 454(2):1393–1403, 2015.

D. P. Stark, R. S. Ellis, S. Charlot, J. Chevallard, M. Tang, S. Belli, A. Zitrin, R. Mainali, J. Gutkin, A. Vidal-García, R. Bouwens, and P. Oesch. Lyα and C III] emission in z = 7-9 Galaxies: accelerated reionization around luminous star-forming systems? *Monthly Notices of the Royal Astronomical*, 464:469–479, Jan. 2017. doi: 10.1093/mnras/stw2233.

C. C. Steidel, G. C. Rudie, A. L. Strom, M. Pettini, N. A. Reddy, A. E. Shapley, R. F. Trainor, D. K. Erb, M. L. Turner, N. P. Konidaris, K. R. Kulas, G. Mace, K. Matthews, and I. S. McLean. Strong Nebular Line Ratios in the Spectra of z $\sim$ 2-3 Star Forming Galaxies: First Results from KBSS-MOSFIRE. *The Astrophysical Journal*, 795:165, Nov. 2014. doi: 10.1088/0004-637X/795/2/165.

C. C. Steidel, A. L. Strom, M. Pettini, G. C. Rudie, N. A. Reddy, and R. F. Trainor. Reconciling the Stellar and Nebular Spectra of High-redshift Galaxies. *The Astrophysical Journal*, 826:159, Aug. 2016. doi: 10.3847/0004-637X/826/2/159.

B. Strömgren. The Physical State of Interstellar Hydrogen. *The Astrophysical Journal*, 89:526, May 1939. doi: 10.1086/144074.

R. Sutherland, M. Dopita, L. Binette, and B. Groves. MAPPINGS III: Modelling And Prediction in PhotoIonized Nebulae and Gasdynamical Shocks. Astrophysics Source Code Library, June 2013.

L. J. Tacconi, R. Neri, R. Genzel, F. Combes, A. Bolatto, M. C. Cooper, S. Wuyts, F. Bournaud, A. Burkert, J. Comerford, P. Cox, M. Davis, N. M. Förster Schreiber, S. García-Burillo, J. Gracia-Carpio, D. Lutz, T. Naab, S. Newman, A. Omont, A. Saintonge, K. Shapiro Griffin, A. Shapley, A. Sternberg, and B. Weiner. Phibss: Molecular Gas Content and Scaling Relations in z $\sim$ 1-3 Massive, Main-sequence Star-forming Galaxies. *The Astrophysical Journal*, 768:74, May 2013. doi: 10.1088/0004-637X/768/1/74.

T. X. Thuan, Y. I. Izotov, and V. A. Lipovetsky. Heavy element abundances in a new sample of low-metallicity blue compact galaxies. *The Astrophysical Journal*, 445:108–123, May 1995. doi: 10.1086/175676.

B. M. Tinsley. Evolution of the Stars and Gas in Galaxies. *The Astrophysical Journal*, 151:547, Feb. 1968. doi: 10.1086/149455.

L. Trouille, A. J. Barger, and C. Tremonti. The OPTX Project V: Identifying Distant AGNs. *ArXiv e-prints*, Sept. 2011.

N. Vale Asari, G. Stasińska, C. Morisset, and R. Cid Fernandes. BOND: Bayesian Oxygen and Nitrogen abundance Determinations in giant H II regions using strong and semistrong lines. *Monthly Notices of the Royal Astronomical Society*, 460:1739–1757, Aug. 2016. doi: 10.1093/mnras/stw971.

E. Vanzella, L. Pentericci, A. Fontana, A. Grazian, M. Castellano, K. Boutsia, S. Cristiani, M. Dickinson, S. Gallozzi, E. Giallongo, M. Giavalisco, R. Maiolino, A. Moorwood, D. Paris, and P. Santini. Spectroscopic Confirmation of Two Lyman Break Galaxies at Redshift Beyond 7. *The Astrophysical Journal, Letters*, 730:L35, Apr. 2011. doi: 10.1088/2041-8205/730/2/L35.

E. Vanzella, S. De Barros, G. Cupani, W. Karman, M. Gronke, I. Balestra, D. Coe, M. Mignoli, M. Brusa, F. Calura, G.-B. Caminha, K. Caputi, M. Castellano, L. Christensen, A. Comastri, S. Cristiani, M. Dijkstra, A. Fontana, E. Giallongo, M. Giavalisco, R. Gilli, A. Grazian, C. Grillo, A. Koekemoer, M. Meneghetti, M. Nonino, L. Pentericci, P. Rosati, D. Schaerer, A. Verhamme,

C. Vignali, and G. Zamorani. High-resolution Spectroscopy of a Young, Low-metallicity Optically Thin L = 0.02L* Star-forming Galaxy at z = 3.12. *The Astrophysical Journal, Letters*, 821:L27, Apr. 2016. doi: 10.3847/2041-8205/821/2/L27.

E. Vazquez-Semadeni. Are There Phases in the ISM? *ArXiv e-prints*, Feb. 2009.

F. Vincenzo, F. Belfiore, R. Maiolino, F. Matteucci, and P. Ventura. Nitrogen and oxygen abundances in the Local Universe. *Monthly Notices of the Royal Astronomical Society*, 458:3466–3477, June 2016. doi: 10.1093/mnras/stw532.

M. Volonteri and M. J. Rees. Quasars at z=6: The Survival of the Fittest. *The Astrophysical Journal*, 650:669–678, Oct. 2006. doi: 10.1086/507444.

E. Westra, D. H. Jones, C. E. Lidman, K. Meisenheimer, R. M. Athreya, C. Wolf, T. Szeifert, E. Pompei, and L. Vanzi. The wide field imager Lyman-alpha search (WFILAS) for galaxies at redshift $\sim$ 5.7. II. Survey design and sample analysis. *Astronomy & Astrophysics*, 455:61–72, Aug. 2006. doi: 10.1051/0004-6361:20064882.

J. C. Wheeler, C. Sneden, and J. W. Truran, Jr. Abundance ratios as a function of metallicity. *Annual Review of Astronomy & Astrophysics*, 27:279–349, 1989. doi: 10.1146/annurev.aa.27.090189.001431.

C. J. Willott, R. J. McLure, P. Hibon, R. Bielby, H. J. McCracken, J.-P. Kneib, O. Ilbert, D. G. Bonfield, V. A. Bruce, and M. J. Jarvis. An Exponential Decline at the Bright End of the z = 6 Galaxy Luminosity Function. *The Astronomical Journal*, 145:4, Jan. 2013. doi: 10.1088/0004-6256/145/1/4.

S.-C. Yoon and N. Langer. Evolution of rapidly rotating metal-poor massive stars towards gamma-ray bursts. *Astronomy & Astrophysics*, 443:643–648, Nov. 2005. doi: 10.1051/0004-6361:20054030.

W. Zheng, G. A. Kriss, R. C. Telfer, J. P. Grimes, and A. F. Davidsen. A Composite HST Spectrum of Quasars. *The Astrophysical Journal*, 475:469–478, Feb. 1997. doi: 10.1086/303560.

Appendices

Appendix A

Table A.1: CLOUDY C13 default Solar Composition

A			12+log	log	n/n(H)	ref
1	H	Hydrogen	12.00	0.00	1.00E+00	GS98
2	He	Helium	11.00	−1.00	1.00E-01	text
3	Li	Lithium	3.31	−8.69	2.04E-09	GS98
4	Be	Beryllium	1.42	−10.58	2.63E-11	GS98
5	B	Boron	2.79	−9.21	6.17E−10	GS98
6	C	Carbon	8.39	−3.61	2.45E-04	AP02
7	N	Nitrogen	7.93	−4.07	8.51E-05	H01
8	O	Oxygen	8.69	−3.31	4.90E-04	AP01
9	F	Fluorine	4.48	−7.52	3.02E-08	GS09
10	Ne	Neon	8.00	−4.00	1.00E-04	H01
11	Na	Sodium	6.33	−5.67	2.14E-06	GS98
12	Mg	Magnesium	7.54	−4.46	3.47E-05	H01
13	Al	Aluminium	6.47	−5.53	2.95E-06	GS98
14	Si	Silicon	7.54	−4.46	3.47E-05	H01
15	P	Phosphorus	5.51	−6.50	3.20E-07	GS98*
16	S	Sulphur	7.27	−4.74	1.84E-05	GS98*
17	Cl	Chlorine	5.28	−6.72	1.91E-07	GS98
18	Ar	Argon	6.40	−5.60	2.51E-06	GS98
19	K	Potassium	5.12	−6.88	1.32E-07	GS98
20	Ca	Calcicum	6.36	−5.64	2.29E-06	GS98
21	Sc	Scandium	3.17	−8.83	1.48E-09	GS98
22	Ti	Titanium	5.02	−6.98	1.05E-07	GS98
23	V	Vanadium	4.00	−8.00	1.00E-08	GS98
24	Cr	Chromium	5.67	−6.33	4.68E-07	GS98
25	Mn	Manganese	5.46	−6.54	2.88E-07	GS98*
26	Fe	Iron	7.45	−4.55	2.82E-05	H01
27	Co	Cobalt	4.92	−7.08	8.32E-08	GS98
28	Ni	Nickel	6.25	−5.75	1.78E-06	GS98
29	Cu	Copper	4.21	−7.79	1.62E-08	GS98
30	Zn	Zinc	4.60	−7.40	3.98E-08	GS98

References: GS98:Grevesse and Sauval (1998), GS98*: mean of photospheric and meteoritic, H01: Holweger (2001), AP01, AP02: Allende Prieto et al. (2001,2002).

Table A.2: PyCloudy and CLOUDY emission line commands. Adapted from 3MdB database commands (Morisset et al. (2015)).

pyCloudy	CLOUDY	Comments	pyCloudy	CLOUDY	Comments	pyCloudy	CLOUDY	Comments
BAC__3646A	Bac 3646	BalmHead	COUT__3646A	cout 3646	OutwardBalmPeak	CREF__3646A	cref 3646	ReflectedBalmPeak
H__1__4861A	H 1 4861	H I 4861	TOTL__4861A	TOTL 4861	H I 4861	H__1__6563A	H 1 6563	H I 6563
H__1__4340A	H 1 4340	H I 4340	H__1__4102A	H 1 4102	H I 4102	H__1__3970A	H 1 3970	H I 3970
H__1__3835A	H 1 3835	H I 3835	H__1__1216A	H 1 1216	H I 1216	H__1_4051M	H 1 4.051	H I 4.051m
H__1_2625M	H 1 2.625	H I 2.625m	H__1_7458M	H 1 7.458	H I 7.458m	HE_1__5876A	He 1 5876	He I 5876
CA_B__5876A	Ca B 5876	He I 5876 Bcase	HE_1__7281A	He 1 7281	He I 7281	HE_1__7065A	He 1 7065	He I 7065
HE_1__4471A	He 1 4471	He I 4471	CA_B__4471A	Ca B 4471	He I 4471 Bcase	HE_1__6678A	He 1 6678	He I 6678
CA_B__6678A	Ca B 6678	He I 6678 Bcase	TOTL_1083M	TOTL 1.083	He I 1.083	HE_2__1640A	He 2 1640	He I 1640
HE_2__4686A	He 2 4686	He II 4686	C__1__8727A	C 1 8727	[C I] 8727	TOTL__9850A	TOTL 9850	[C I] 9850
C_IC__9850A	C Ic 9850	[C I] 9850 coll	TOTL__2326A	TOTL 2326	C II] 2326+	C__2__1335A	C 2 1335	C II 1335
C__2__1761A	C 2 1761	C II 1761	TOTL__6580A	TOTL 6580	[C II] 6580	C__2__4267A	C 2 4267	C II 4267
C__2_1576M	C 2 157.6	[C II] 157.6m	C__3_9770A	C 3 977.0	[C III] 977	C__3__1907A	C 3 1907	[C III] 1907
C__3__1910A	C 3 1910	[C III] 1910	C__3__4649A	C 3 4649	C III 4649	C__3__2297A	C 3 2297	C III 2297
TOTL__1549A	TOTL 1549	C IV 1549 totl	C__4__1549A	C 4 1549	C IV 1549 rec	C__4__4659A	C 4 4659	C IV 4649
N__1__5198A	N 1 5198	[N I] 5198	N__1__5200A	N 1 5200	[N I] 5200	N__2__5755A	N 2 5755	[N II] 5755
N_2R__5755A	N 2r 5755	N II 5755 rec	N__2__6548A	N 2 6548	[N II] 6548	N__2__6584A	N 2 6584	[N II] 6584
N__2__2141A	N 2 2141	N II 2141	N__2__4239A	N 2 4239	N II 4239	N__2__4041A	N 2 4041	N II 4041
TOTL__5679A	TOTL 5679	N II 5679 totl	N__2_1217M	N 2 121.7	[N II] 121.7m	N__2_2054M	N 2 205.4	[N II] 205.4m
N__3_5721M	N 3 57.21	[N III] 57.21m	N__3__4641A	N 3 4641	N III 4641	TOTL__1750A	TOTL 1750	N III] 1750+
N__3__4379A	N 3 4379	N III 4379	N__4__1485A	N 4 1485	N IV] 1485	N__4__1719A	N 4 1719	N IV 1719
TOTL__1240A	TOTL 1240	[N V] 1240 totl	N__5__1239A	N 5 1239	[N V] 1239	O__1__7773A	O 1 7773	O I 7773
O__1__6300A	O 1 6300	[O I] 6300	O__1__5577A	O 1 5577	[O I] 5577	O__1_6317M	O 1 63.17	[O I] 63.17m
O__1_1455M	O 1 145.5	[O I] 145.5m	O_II__3726A	O II 3726	[O II] 3726	O_II__3729A	O II 3729	[O II] 3729
O_II__7323A	O II 7323	[O II] 7323	O_II__7332A	O II 7332	[O II] 7332	O_2R__3726A	O 2r 3726	O II 3726 rec
O_2R__3729A	O 2r 3729	O II 3729 rec	O_2R__7323A	O 2r 7323	O II 7323 rec	O_2R__7332A	O 2r 7332	O II 7332 rec
TOTL__3727A	TOTL 3727	[O II] 3727+	TOTL__7325A	TOTL 7325	[O II] 7325+	O_II__2471A	O II 2471	[O II] 2471+
O__2__4152A	O 2 4152	O II 4152	TOTL__4341A	TOTL 4341	O II 4341	O__2__4651A	O 2 4651	O II 4651
O_2R__4651A	O 2r 4651	O II 4651+	TOTL__4363A	TOTL 4363	[O III] 4363	REC__4363A	Rec 4363	O III 4363 rec
O__3__4959A	O 3 4959	[O III] 4959	O__3__5007A	O 3 5007	[O III] 5007	O__3_5180M	O 3 51.80	[O III] 51.8m
O__3_8833M	O 3 88.33	[O III] 88.33m	TOTL__1665A	TOTL 1665	[O III] 1665+	TOTL__1402A	TOTL 1402	O IV] 1402+
O__4__1342A	O 4 1342	O IV 1342	O__4_2588M	O 4 25.88	[O IV] 25.88m	TOTL__1218A	TOTL 1218	O V] 1218+
O__5__1216A	O 5 1216	[O V] 1216	NE_2_1281M	Ne 2 12.81	[Ne II] 12.81m	NE_3__3869A	Ne 3 3869	[Ne III] 3869
NE_3__3968A	Ne 3 3968	[Ne III] 3968	NE_3_1555M	Ne 3 15.55	[Ne III] 15.55m	NE_3_3601M	Ne 3 36.01	[Ne III] 36.01m
NE_3__1815A	Ne 3 1815	[Ne III] 1815	NE_4__1602A	Ne 4 1602	[Ne IV] 1602	NE_4__2424A	Ne 4 2424	[Ne IV] 2424
NE_4__4720A	Ne 4 4720	[Ne IV] 4720+	NE_5__3426A	Ne 5 3426	[Ne V] 3426	NE_5__3346A	Ne 5 3346	[Ne V] 3346
NE_5__2976A	Ne 5 2976	[Ne V] 2976	NE_5_2431M	Ne 5 24.31	[Ne V] 24.31m	NE_5_1432M	Ne 5 14.32	[Ne V] 14.32m
TOTL__2798A	TOTL 2798	[Mg II] 2798+	SI_2_3481M	Si 2 34.81	[Si II] 34.81m	SI_2__2334A	Si 2 2334	[Si II] 2334
SI_3__1892A	Si 3 1892	[Si III] 1892	SI_4__1394A	Si 4 1394	[Si IV] 1394	S_II__4070A	S II 4070	[S II] 4070
S_II__4078A	S II 4078	[S II] 4078	S_II__6731A	S II 6731	[S II] 6731	S_II__6716A	S II 6716	[S II] 6716
S_II_1029M	S II 1.029	[S II 1.029m	S_II_1034M	S II 1.034	[S II] 1.034m	S_II_1032M	S II 1.032	[S II] 1.032m
S_II_1037M	S II 1.037	[S II] 1.037m	S__3__6312A	S 3 6312	[S III] 6312	S__3__9532A	S 3 9532	[S III] 9532
S__3__9069A	S 3 9069	[S III] 9069	S__3_1867M	S 3 18.67	[S III] 18.67m	S__3_3347M	S 3 33.47	[S III] 33.47m
S__4_1051M	S 4 10.51	[S IV] 10.51m	S__4__1398A	S 4 1398	[S IV] 1398	CL_2__8579A	Cl 2 8579	[Cl II] 8579
CL_2__9124A	Cl 2 9124	[Cl II] 9124	CL_2__6162A	Cl 2 6162	[Cl II] 6162	CL_2_1440M	Cl 2 14.40	[Cl II] 14.40m
CL_3__8552A	Cl 3 8552	[Cl III] 8552	TOTL__8494A	TOTL 8494	[Cl III] 8494+	CL_3__5538A	Cl 3 5538	[Cl III] 5538
CL_3__5518A	Cl 3 5518	[Cl III] 5518	CL_4__7532A	Cl 4 7532	[Cl IV] 7532	CL_4_2040M	Cl 4 20.40	[Cl IV] 20.40m
CL_4_1170M	Cl 4 11.70	[Cl IV] 22.70m	AR_2_6980M	Ar 2 6.980	[Ar II] 6.98m	AR_3__7135A	Ar 3 7135	[Ar III] 7135
AR_3__7751A	Ar 3 7751	[Ar III] 7751	AR_3__5192A	Ar 3 5192	[Ar III] 5192	AR_3_9000M	Ar 3 9.000	[Ar III] 9.00m
AR_3_2183M	Ar 3 21.83	[Ar III] 21.83m	AR_4__7171A	Ar 4 7171	[Ar IV] 7171	AR_4__4711A	Ar 4 4711	[Ar IV] 4711
AR_4__4740A	Ar 4 4740	[Ar IV] 4740	AR_5__7005A	Ar 5 7005	[Ar V] 7005	AR_5_1310M	Ar 5 13.10	[Ar V] 13.1m
AR_5_8000M	Ar 5 8.000	[Ar V] 8.00m	FE_2__8617A	Fe 2 8617	[Fe II] 8617	FE_3__4608A	Fe 3 4608	[Fe III] 4608
FE_3__4668A	Fe 3 4668	[Fe III] 4668	FE_3__4659A	Fe 3 4659	[Fe III] 4659	FE_3__4702A	Fe 3 4702	[Fe III] 4702
FE_3__4734A	Fe 3 4734	[Fe III] 4734	FE_3__4881A	Fe 3 4881	[Fe III] 4881	FE_3__5271A	Fe 3 5271	[Fe III] 5271
FE_3__4755A	Fe 3 4755	[Fe III] 4755	FE_4__2836A	Fe 4 2836	[Fe IV] 2836	FE_6__5177A	Fe 6 5177	[Fe VI] 5177
FE_7__4894A	Fe 7 4894	[Fe VII] 4894	FE_7__5721A	Fe 7 5721	[Fe VII] 5721	FE_7__4989A	Fe 7 4989	[Fe VII] 4989
FE_7__6087A	Fe 7 6087	[Fe VII] 6087	FE_7__5277A	Fe 7 5277	[Fe VII] 5277	F12__1200M	F12 12.00	IRAS 12m
F25__2500M	F25 25.00	IRAS 25m	F60__6000M	F60 60.00	IRAS 60m	F100_1000M	F100 100.00	IRAS 100m
MIPS_2400M	MIPS 24.00	MIPS 24m	MIPS_7000M	MIPS 70.00	MIPS 70m	MIPS_1600M	MIPS 160.0	MIPS 160m
IRAC_3600M	IRAC 3.600	IRAC 3.6m	IRAC_4500M	IRAC 4.500	IRAC 4.5m	IRAC_5800M	IRAC 5.800	IRAC 5.8m
IRAC_8000M	IRAC 8.000	IRAC 8.0m						

Appendix B

BPASS SEDs Compilation

The BPASS inputs for CLOUDY were done in two steps and involved the creation of ascii files (for the different stellar metallicity of the models) and its compilation into binary atmosphere files (with .mod extension). The binary compilation is necessary to avoid delays when reading the grids (which are large files). The binary files created are hardware dependent and they must be compiled inside the data folder on CLOUDY directory. The ascii and other downloaded files can be deleted after the compilation since the binary files are the ones that CLOUDY actually uses.

The atmosphere files were created following the guidelines CLOUDY C13 documentation last described in Ferland et al. (2013), and contain the next information, which must be specified in the following order:

- Magic number, which is a number that identifies the syntax version. For CLOUDY C13 the syntax is identified by version'20060612'.
- Number of dimensions (*ndim*) that are varied in the grid. This is usually a number between 1 and 4. In our case the parameter changing in the grid is just '1', corresponding to the age.
- Number of parameters (*npar*) that are supplied for each atmosphere model. This number is also '1' corresponding to the ages.
- Label for the parameters: 'Age'. Note that this is the label for the first parameter. If there were more parameters in the grid they must have been specified using as much labels as the parameters.
- Number of atmosphere models (*nmod*). In this case '10' ages were used (instead of the 41).
- Number of points of the independent variable (*nwave*) corresponding to '100000' wavelength values.

The next four parameters explains to CLOUDY how to convert the previous variables to CLOUDY internal units (note that the conversion factors are multiplied with the numbers in the ascii file).

- Type of the independent variable. Defining 'lambda' sets that the grid is given in wavelength.
- Conversion factor for the wavelength. Since the default units of wavelength are Angstroms, the conversion factor is '1'.

- Type of the dependent variable. In our case, the dependent variable is flux per wavelength which corresponds to 'F_lambda'.

- Conversion factor for the dependent variable which converts the flux density in $\mathrm{erg\,cm^{-2}\ s^{-1}\ \mathring{A}^{-1}}$. It is important to note that in our case, the BPASS fluxes are given in $\mathrm{L_\odot \mathring{A}^{-1}}$, so they correspond to luminosity densities $\mathrm{L_\lambda}$, usually expressed, in astronomy, in $\mathrm{erg\ s^{-1} \mathring{A}^{-1}}$. Luminosity density does not depend on the distance between the source and the cloud while flux density $\mathrm{F_\lambda}$ is not independent. To let this parameter independent, i.e. not dependent of the radius of the cloud, we set this factor to '1'.

CLOUDY converts flux density into energy density necessary for the SED. This is done by multiplying the flux density by the wavelength, obtaining $\lambda\ \mathrm{F_\lambda}$, i.e. energy per unit area per unit time. In our case CLOUDY will be multiplying luminosity density by the photons, which leads to SEDs in $\lambda\ \mathrm{L_\lambda}$, i.e. energy per unit time, in $\mathrm{L_\odot}$ units.

Each ascii file created corresponds to a BPASS metallicity, where the age is the parameter that variates in the grid. To create the binary files with the generic name atmosphere.mod, it is necessary to execute CLOUDY in the CLOUDY data directory (containing the ascii files) with the command '*compile stars "spectra-name.ascii"*'. This was done creating a compile.in file and running it using 'cloud directory + *cloudy.exe -r compile*' which directs its output to compile.out giving the information if the compilation was successful. All the ascii files were compiled individually.

Appendix C

Carbon and Oxygen line-ratios

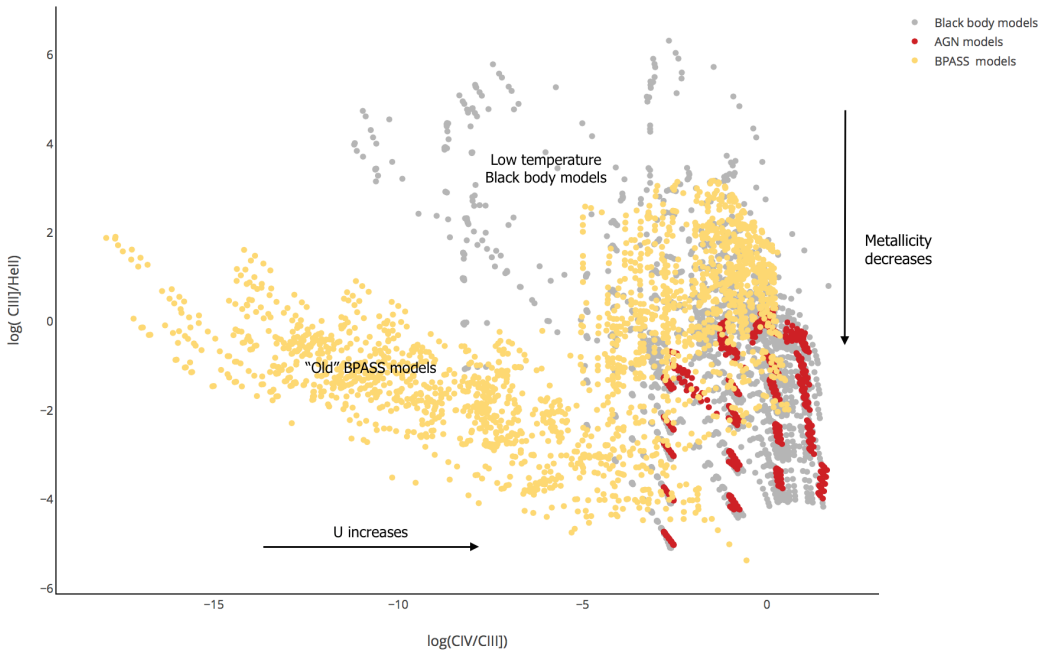

Figure C.1: Log(CIII]λ1909/HeIIλ1640) vs log(CIVλ1549/CIII]λ1909) diagram spanning the full range of parameters listed in Table 3.1.

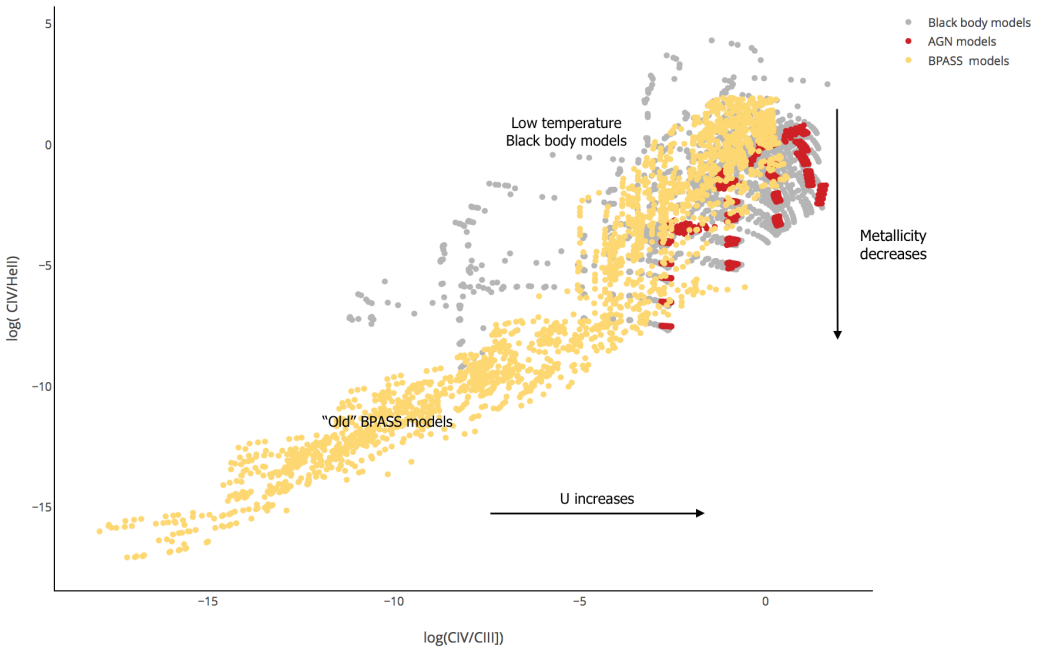

Figure C.2: Log(CIVλ1549/HeIIλ1640) vs log(CIVλ1549/CIII]λ1909) diagram spanning the full range of parameters listed in Table 3.1.

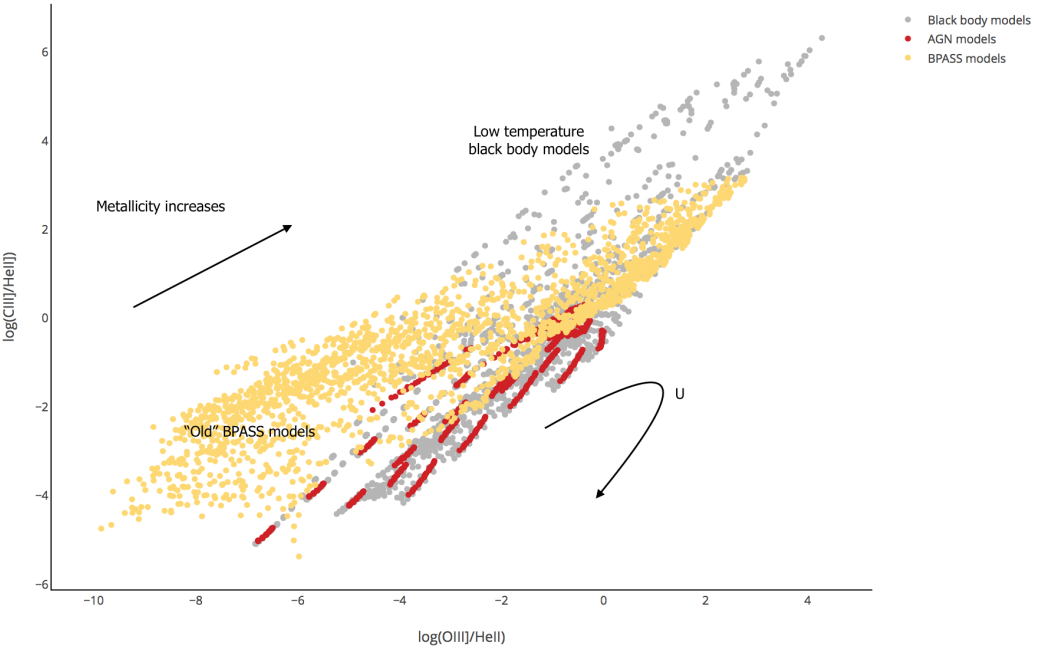

Figure C.3: Log(CIII]λ1909/HeIIλ1640) vs log(OIII]λ1665/HeIIλ1640) diagram spanning the full range of parameters listed in Table 3.1.

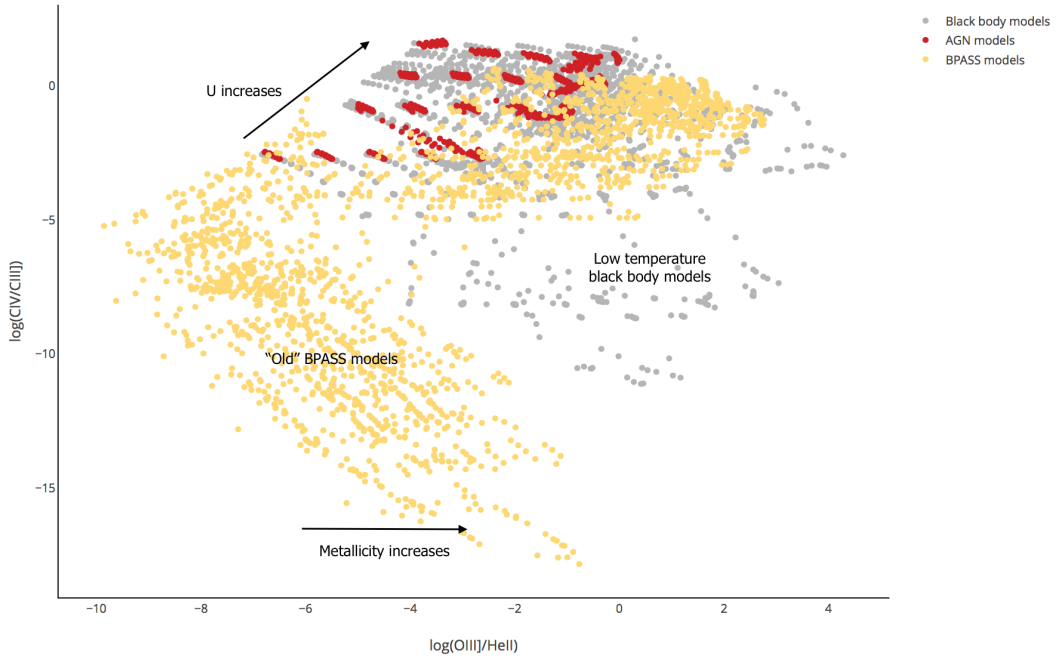

Figure C.4: Log(CIVλ1549/CIII]λ1909) vs log(OIII]λ1665/HeIIλ1640) diagram spanning the full range of parameters listed in Table 3.1.

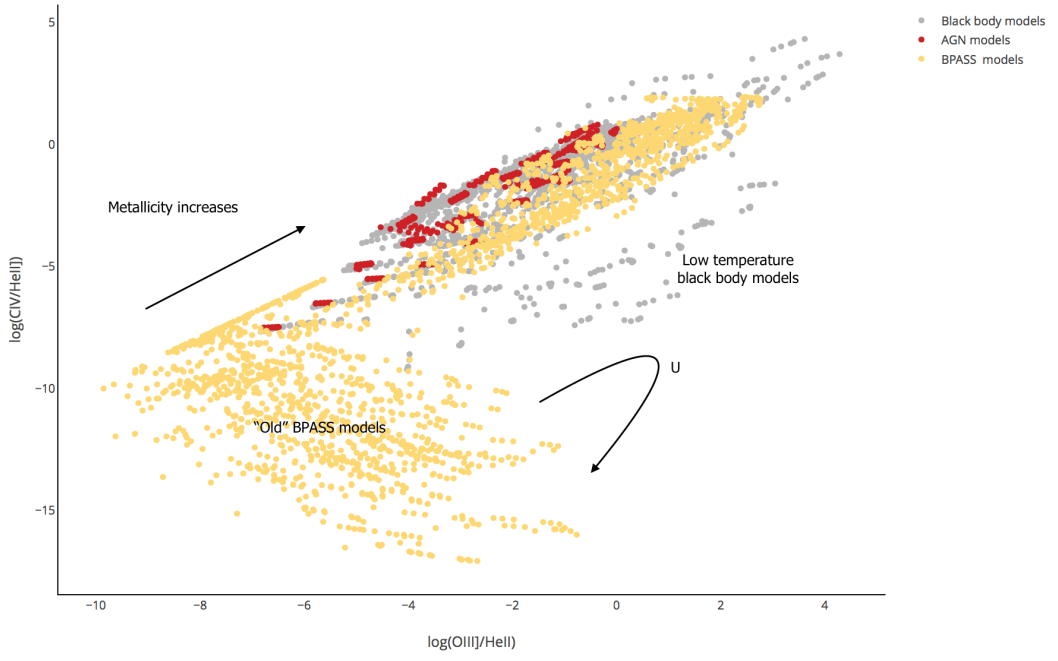

Figure C.5: Log(CIVλ1549/HeIIλ1640) vs log(OIII]λ1665/HeIIλ1640) diagram spanning the full range of parameters listed in Table 3.1.

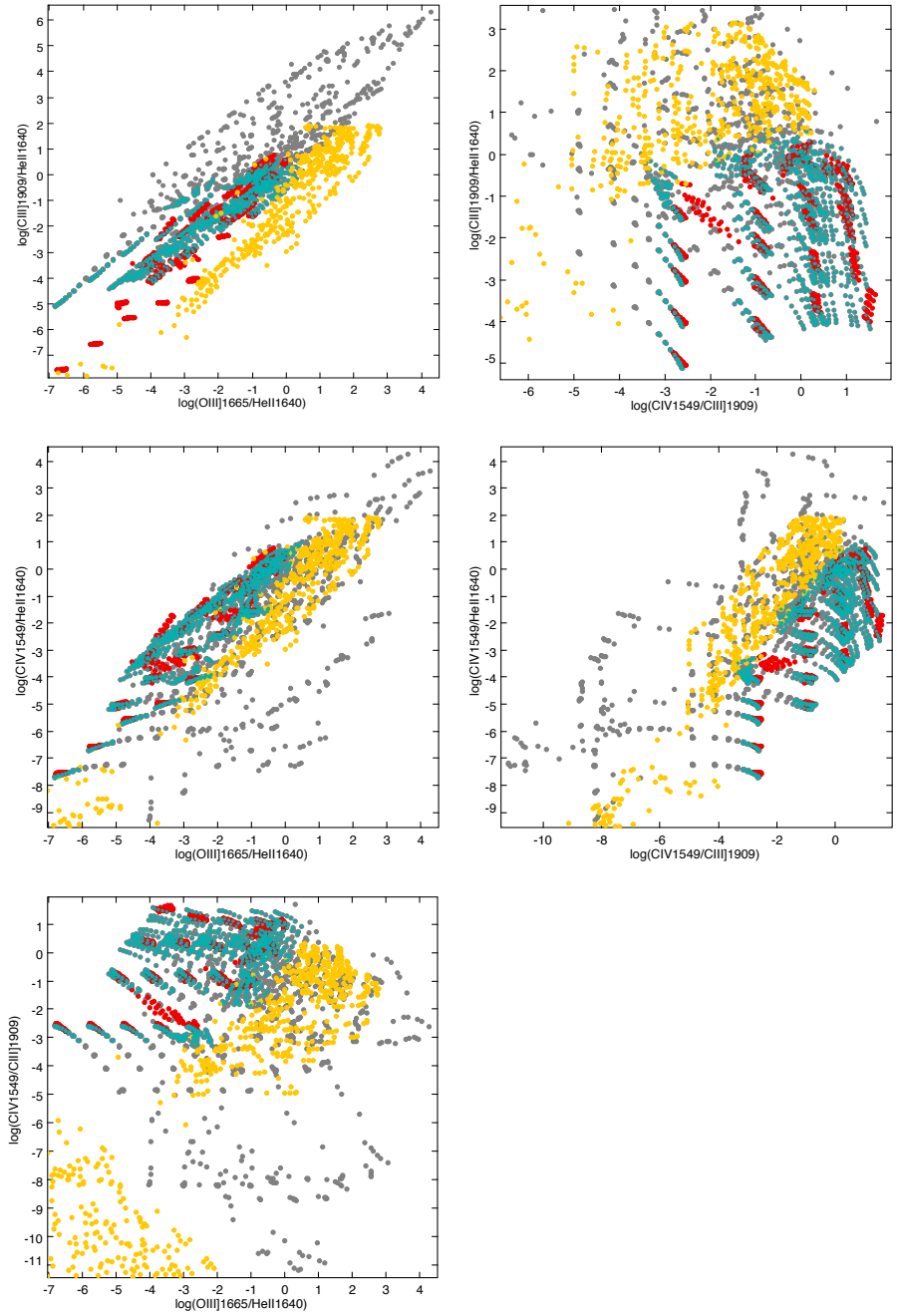

Figure C.6: Various combinations of emission line ratios using CIV, CIII], OIII] and HeII. Our black body models are indicated by the grey dots. AGN (power law models) for the full range of parameters, listed in Table 3.1 are indicated by the red dots. Our BPASS galaxies with $Z_{\odot} \geq 0.01$ are indicated by the yellow dots and Black body models with T $\geq$ 80000K by the green dots.

Appendix D

Amorín et al. (2017) SFGs properties

Table D.1: Emission line measurements, calculated abundances and ionization properties of the 10 SFGs (where (1) corresponds to the VUDS identification) and composite spectrum from Amorín et al. (2017).

VUDS ID (1)	z	EW_0(Lyα)	F(Lyα)	F(CIV)	F(He II)	F(O III])	F(C III])	$12+\log(O/H)$	$\log(C/O)$	$\log(U)$
510583858	2.4141	111±16	126.3±6.8	4.1±1.4	10.2±5.1	7.2±1.4	8.2±1.4	7.43±0.31	-0.95±0.10	-2.03±0.26
510838687	2.5539	35±12	19.5±3.2	5.7±1.1	<1.4	4.6±1.1	12.4±1.8	7.56±0.36	-0.57±0.06	-1.98±0.41
511267982	2.8256	56±12	67.7±4.2	4.6±1.1	<3.8	6.9±1.5	16.6±3.8	7.59±0.24	-0.67±0.08	-2.05±0.18
5100534435	2.9635	47±11	44.0±4.0	<1.4	<2.0	4.0±0.8	4.6±1.9	7.71±0.20	-1.00±0.09	-2.03±0.13
5100565880	3.0505	168±10	567.1±8.1	41.3±5.3	9.3±1.2	13.0±2.0	36.9±6.5	7.59±0.26	-0.38±0.10	-1.73±0.40
5100750978	2.9630	82±12	120.9±5.9	1.6±0.8	2.0±1.2	4.0±1.2	7.9±1.2	7.55±0.21	-0.78±0.04	-2.25±0.11
5100994378	2.7970	89±10	377.0±11.7	6.1±1.1	10.6±1.9	7.6±1.1	22.0±1.5	7.51±0.32	-0.61±0.06	-2.15±0.18
5100998761	2.4460	185±35	361.5±21.4	8.3±1.4	6.9±3.1	8.6±1.7	21.4±2.4	7.38±0.19	-0.64±0.06	-2.01±0.11
5101421970	2.4650	261±30	738.4±31.5	27.7±4.9	16.6±3.5	22.5±3.5	26.0±5.2	7.58±0.38	-0.81±0.11	-1.97±0.45
5101444192	3.4240	267±35	182.3±3.5	3.5±0.9	2.7±0.4	4.9±0.9	11.5±1.3	7.66±0.24	-0.67±0.07	-2.04±0.16
Composite		131±11	260.0±2.0	9.1±1.1	7.0±1.2	8.2±1.0	15.2±1.2	7.54±0.25	-0.69±0.08	-1.90±0.27

Appendix E

VIMOS Instrument - VLT

Located in Cerro Paranal, Chile, the Very Large Telescope (VLT) of the European Southern Observatory (ESO), with four Unit Telescopes of 8.2 meters of diameter each, is the most advanced optical observatory in the world. VIMOS is the Visible Multi-Object Spectrograph, one of the instruments of the Unit Telescope 3 of the VLT, which has a Multi-Object Spectroscopy (MOS) observing mode that allow to obtain multiple spectra, using short slits that are cut by a laser drill into a mask at the positions of the targets. VIMOS has a large field-of-view. For that reason its optical path is split into four channels, which result in four separated quadrants (Figure E.1) that are operated in parallel using the same grism.

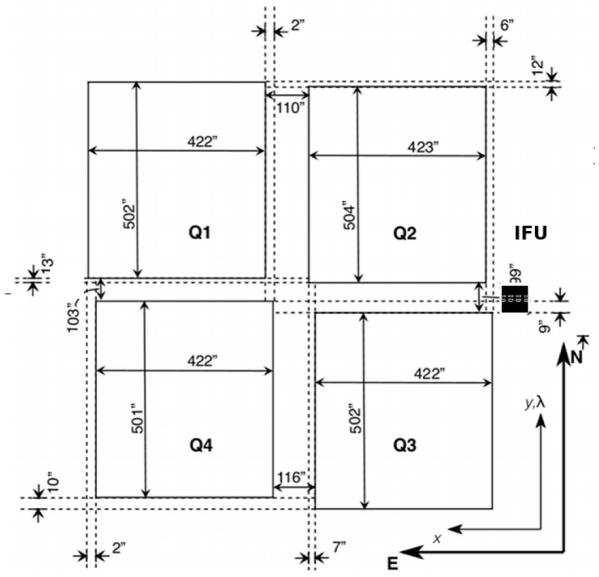

Figure E.1: VIMOS field-of-view. Orientation for a zero degree rotator angle where the x axis of the CCDs is oriented to East and the y axis is oriented to North. Increasing the rotator angle moves the compass counter-clockwise. The four quadrants have approximately the same size and are separated by a gap as indicated in the figure. The pointing coordinates correspond to the center of the gap.

The field-of-view for the four quadrants is 4 x 7' x 8' and it provides an image scale of 0.205"/pixel. The data of this project were taken during the period 84A on six pointings of the UDS field (Table

E.2) using MOS with the low resolution *LR blue* grism, which gives a spectral resolution of 180 with a 1" slit width for a spectral range between 3700 Å − 6700 Å.

POINTINGS	α(J2000)	δ (J2000)
UDS-NE	$2^h\ 19^m\ 00^s$	-4° 48' 00"
UDS-NW	$2^h\ 16^m\ 36^s$	-4° 48' 00"
UDS-CEN	$2^h\ 17^m\ 48^s$	-5° 06' 00"
UDS-W	$2^h\ 16^m\ 36^s$	-5° 06' 00"
UDS-SE	$2^h\ 19^m\ 00^s$	-5° 24' 00"
UDS-SW	$2^h\ 16^m\ 36^s$	-5° 24' 00"

Figure E.2: Coordinates of the six observed pointings.

The use of a low resolution grism allows to place multiple layers of slits along the dispersion direction (Figure E.3). Slits of reference are placed in objects, such as stars, to guarantee the slit mask position. The use of this telescope is fundamental to detect faint emission lines and allows to cover an area of the sky in a single VIMOS pointing for $\sim$ 200 sources. The data obtained from VIMOS corresponds to a spectra imaging with the total slits per quadrant. ESO has available different pipelines to do bias subtraction with overscan removal, flat-fielding and removal of cosmic rays from the raw data. One of the pipeline products obtained is a two-dimensional reduced spectra of the objects found in each slit. The images of the spectra have a dispersion of 5.3 Å per pixel and a starting wavelength of 3700 Å.

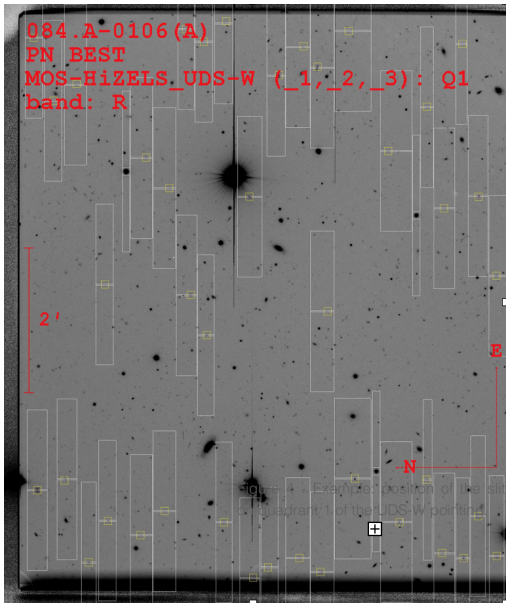

Figure E.3: Example of positioning of the slits on the first quadrant of the UDS-W pointing.